The Interaction of Water with Metal Surfaces

UNIVERSITY OF
LIVERPOOL

Thesis submitted in accordance with the requirements of the University of
Liverpool for the degree of Doctor in Philosophy

by

Ahmed Hussein Omer

Surface Science Research Centre, Department of Chemistry

August 2008

Abstract

The Interaction of Water with Metal Surfaces
Ahmed Hussein Omer

This thesis describes experimental studies of water adsorption on the Ru (0001) and Ni (111) single crystal surfaces. On the model Ru(0001) surface, H_2O and D_2O form intact wetting layers that are very sensitive to the preparation conditions, electron beam irradiation and surface contamination. Whereas LEED shows a well-defined $(\sqrt{3} \times \sqrt{3})R30°$ pattern for 0.67 ML H_2O /D_2O , concurrent helium atom scattering (HAS) measurements show no evidence of sharp diffraction peaks, just very broad maxima close to the second order diffraction position. These maxima are interpreted as diffuse elastic scattering from a highly corrugated but disordered surface, and indicate that water does not form an ordered $\sqrt{3}$ bilayer on this surface. We propose a model in which disordered chains of flat and H-down water are imbedded in a honeycomb network of hydrogen bonded water. This hydrogen bonding network imposes long-range order on the adlayer but allows for substantial local disorder, with disorder arising from the orientation of the water, the orientation of the protons along the chains, the direction of the chains and their length. A structure factor analysis shows that a water layer that is disordered in the vertical location of the O atoms (orientation of the water), while maintaining a well-defined lateral periodicity will give rise to a well-defined LEED pattern. Diffuse scattering of He originates from the sensitivity of the surface corrugation to the position of the (disordered) H atoms and the location of H-down water within the network. For water adsorption on Ni (111), the thermal desorption spectrum shows a simple two-peak profile, with the multilayer only forming upon the saturation of the monolayer. In contrast to the commensurate $\sqrt{3}$ LEED pattern reported previously, we observe a LEED pattern that is consistent with diffraction from two domains of a $(2\sqrt{7} \times 2\sqrt{7})R19°$ unit cell. Adsorption of a second water layer on top of the wetting layer destroys the $2\sqrt{7}$ LEED pattern, indicating that the structure of the wetting layer is disrupted by the formation of hydrogen bonds to the second layer, producing a bulk ice film. Chloroform desorption measurements indicate a layer-by-layer growth of ordered crystalline ice. The relatively short lattice parameter of the Ni (111) surface means that formation of a commensurate $\sqrt{3}$ structure would require a compression of 4.5 % (as compared to bulk ice), which is just too great. Consequently, water prefers to optimise its density and hydrogen-bonding network at the expense of the favoured atop adsorption site.

Acknowledgements

I am extremely grateful to my supervisor Andrew Hodgson for his advice, guidance and good counsel during the last four years. It has been an absolute honour and a privilege to work with him. In the completion of this thesis, I am very much indebted to Mark Gallagher, whom I have worked with on the majority of the experiments. In addition, I am grateful to George Darling who provided the theoretical calculations described in this thesis. I would also like to express my appreciation and high regard for Sam Haq from whom I have learned a great deal about ultra high vacuum techniques and instrumentation, and who has been exceptionally supportive during my PhD. I am also obliged to the past and present members of the Dynamics Group, most specially Chris Clay, Linda Cummings and Georgina Zimbitas. It has also been an honour to work with the Condensed Matter Physics Group, in particular my secondary supervisor Chris Lucas, as well as Ben Fowler. Moreover, it has been my good fortune to work with the esteemed Electrochemist Nenad Markovic, formerly of the University of California Berkeley and currently at the University of Chicago. I would like to say a personal 'thank you' to Rasmita Raval for giving me the opportunity to join the Surface Science Research Centre and to EPSRC for the funding my research. In addition, I very much appreciate the help and kindness of all the people in the SSRC. Finally, I am extremely indebted to all my family and friends who have been a special source of support for me.

Ahmed Hussein Omer 2008

Contents

iii

List of Figures

v

List of Acronyms

AES	-	Auger Electron Spectroscopy
ASW	-	Amorphous Solid Water
DFT	-	Density Functional Theory
EELS	-	Electron Energy Loss Spectroscopy
ESDIAD	-	Electron Stimulated Desorption Ion Angular Distributions
FTIR	-	Fourier Transform Infrared Spectroscopy
HAS	-	Helium Atom Scattering
HREELS	-	High Resolution Electron Energy Loss Spectroscopy
Ih	-	Hexagonal Ice
IR	-	Infrared
IRAS	-	Infra-Red Absorbtion Spectroscopy
LEED	-	Low Energy Electron Diffraction
LEED I-V	-	Low Energy Electron Diffraction Intensity-Voltage
ML	-	Monolayer
RAIRS	-	Reflection Absorption Infra Red Spectroscopy
RHEED	-	Reflection High Energy Electron Diffraction
SFG	-	Sum Frequency Generation
STM	-	Scanning Tunnelling Microscopy
TDS	-	Thermal Desorption Spectroscopy
TPD	-	Temperature Programmed Desorption
TPRS	-	Temperature Programmed Reaction Spectroscopy
TSP	-	Titanium Sublimation Pump
UHV	-	Ultra High Vacuum
UPS	-	Ultraviolet Photoemission Spectroscopy
WF	-	Workfunction
XPS	-	X-ray Photoelectron Spectroscopy
XAFS	-	X-ray Absorption Fine Sturcutre
XAS	-	X-ray Absorption Spectroscopy

Chapter 1

Introduction

The processes occurring at the water-metal interface are implicated in a diverse range of fields including fuel cells, catalysis, electrochemistry, corrosion science and nano-technology. However, despite the long history of research in this area, a comprehensive understanding of the water-metal surface interaction is still lacking. In this thesis we apply a range of surface science techniques including low energy electron diffraction (LEED), temperature programmed desorption (TPD), work function measurements and helium atom scattering (HAS) to investigate the wetting, structure and dynamics of water films on the Ru (0001) and Ni (111) close packed surfaces.

1.1   The Peculiarity of Water

The H_2O molecule (figure 1.1), consisting of two hydrogen atoms bonded to an O atom within a C_{2v} symmetry, is seemingly simple. However, this apparent simplicity is deceptive because, along with the covalent bonding, the hydrogen atoms of a water molecule are able to form subtle bond-like interactions with the oxygen atoms of neighbouring water molecules. In 1920, Latimer and Rodebush first described these interactions as being analogous to bonding [6], an insight, which

ultimately led to the indispensable concept of the hydrogen bond. In general, a hydrogen bonding interaction occurs when an acidic group (AH) and a basic counterpart (B) form an AH...B bond-like interaction. In the case of water, the acidic component is provided by the OH group, with the lone-pair on the O atom acting as the basic counterpart. This ability of a water molecule to act readily as both a donor of electron density (Lewis base) via its oxygen lone pairs and an acceptor (Lewis acid) through its OH group makes it ideally suited for hydrogen bonding. A hydrogen bonding interaction generally consists of electrostatic forces, charge transfer, covalent forces, dispersion forces and exchange repulsion [1]. These hydrogen-bonding interactions govern the chemistry of water and lie behind many of its anomalous physical and chemical properties.
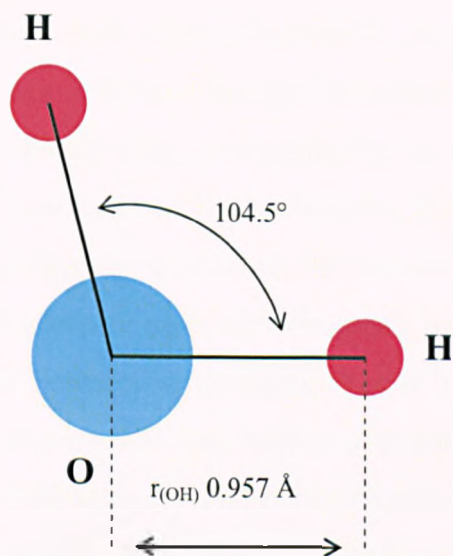
Figure 1.1: Schematic depiction of a water molecule, showing the O-H inter-atomic separation and the HOH angle.

In addition, there is a strong directional element to hydrogen bonds, with the chemical bond of the hydrogen atom donated to the hydrogen bonding pointing directly at the nucleus of the acceptor O atom. In a hydrogen-bonded net-

work such as that found in hexagonal ice, each water molecule contributes two hydrogen atoms to the hydrogen-bonding network, while also accepting two H atom bonds. Consequently, a fully coordinated water molecule has four hydrogen bonds. Counter intuitively, increasing the number of hydrogen bonds between water molecules does not lead to a reduction in the average bond strength. Instead, the formation of the initial hydrogen bond lengthens the covalent O-H bond on the donor molecule. This results in a net redistribution of electric charge towards the O atom, giving it a larger dipole moment and making it a better H bond acceptor. Likewise, the formation of the initial hydrogen bond, leads to a net redistribution of electron density from the protons of the acceptor molecule, towards its O atom and the newly formed H bond, making it a slightly better proton donor. Moreover, the partially charged bridging H atom reduces the repulsive interaction between the O atoms of the donor and acceptor molecules, leading to a decrease in the O-O inter-atomic distance. Further H bond formation leads to a net shortening of the R(O-O) length together with a strengthening of the H bonding interaction. Thus, contrary to the usual anti-correlation between the number and the strength of the bonds formed, in hydrogen bonding interactions there is a degree of *co-operativity* whereby the acceptor molecule becomes a better proton donor and the donor molecule a better acceptor as the number of H bonds increases [7] [8] [9].

A free water molecule possesses nine degrees of freedom, three rotational, three translational and three vibrational. The three vibrational modes are termed the symmetric stretch, the asymmetric stretch, and the scissors (also known as the bending mode) [1]. For isolated water molecules, the stretching mode appears at 3630-3750 cm^{-1} in the IR spectrum while the scissors mode appears in the region around 1595 cm^{-1}. The formation of hydrogen bonds produces a distinctive red shift (lower frequency) in the stretching frequencies due to the weakening of the covalent O-H bond. Comparison of water clusters with increasing number of water molecules and degree of hydrogen bonding shows that this red shift is directly

correlated with the hydrogen bond strength [17]. On the other hand, the scissors mode experiences a shift to higher frequencies (blue shift) as the formation of hydrogen bonds makes this motion more rigid. Moreover, since the scissors mode involves the motion of all three atoms in the H_2O molecule, its appearance in the IR spectrum provides reliable evidence of non-dissociative adsorption. In contrast, the presence of dissociation in a water adlayer leads to significant attenuation in the intensity of this mode. Furthermore, in addition to the OH stretching and the scissors mode, a water molecule adsorbed on a surface exhibits additional vibrational modes arising from "frustrated" rotations (librations) and translations [10].

1.2   Crystalline Ice and the Ice Rules

At temperatures below 274 K, water condenses into its solid phase: ice. Although, there are more than a dozen types of ice, depending on the temperature and pressure, ice I (figure 1.2), which comprises of cubic ice (Ic, ABCA... packing sequence) and hexagonal ice (Ih, ABAB...) is the only naturally occurring type.

In 1933, Fowler and Bernal [11] drafted a set of rules to describe the arrangement of water molecules in hexagonal ice. Then in 1935, Linus Pauling [12] reappraised the structure of ice and added further rules. The subsequent combination of the Bernal, Fowler and Pauling rules is generally known as the BFP ice rules or simply 'the ice rules'. According to these rules, each O atom of a water molecule should have two H atoms attached to it, with equal bond lengths of 0.96 Å and an H-O-H bond angle of 105° . Each water molecule should in turn bond to four other O atoms via hydrogen bonds, directed along the O-O axis, thus leading to a tetrahedral arrangement (figure 1.3). Moreover, each O-O axis may contain a maximum of one hydrogen atom. Finally, interactions between non-adjacent molecules are regarded as insufficient to contribute significantly to the stabiliza-
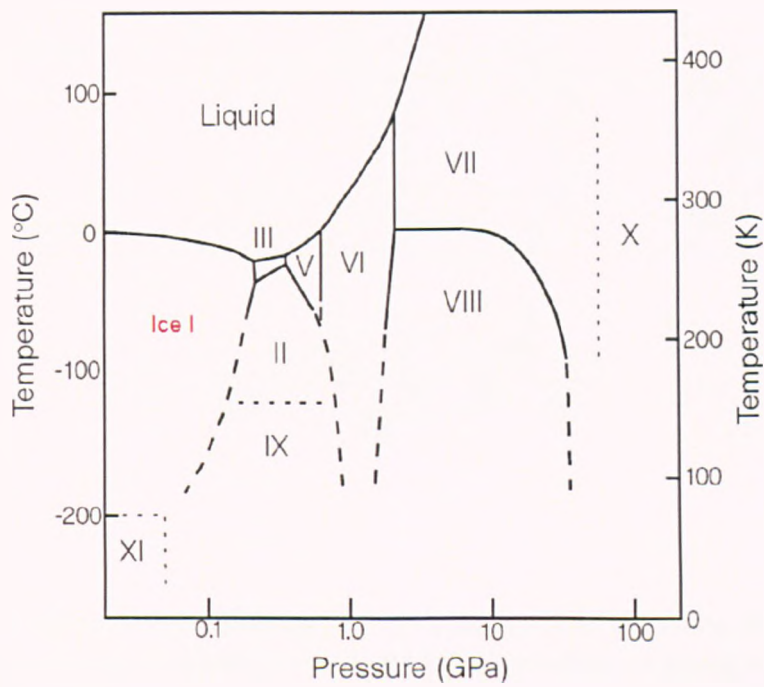
Figure 1.2: The phase diagram of water, showing the various types of ice (ice I shown in red). Adapted from Lobban *et al.* [2].

tion of any structural configuration. In both Ic and Ih, the O-O separation is 2.76 Å (at 273 K and 1 atm pressure). This O-O separation closely resembles the lattice parameters of close packed transitional metal surfaces (e.g. Ru (0001) = 2.704 Å). Consequently, it has traditionally been thought that these surfaces should provide ideal templates for growing commensurate 2D ice films [13].
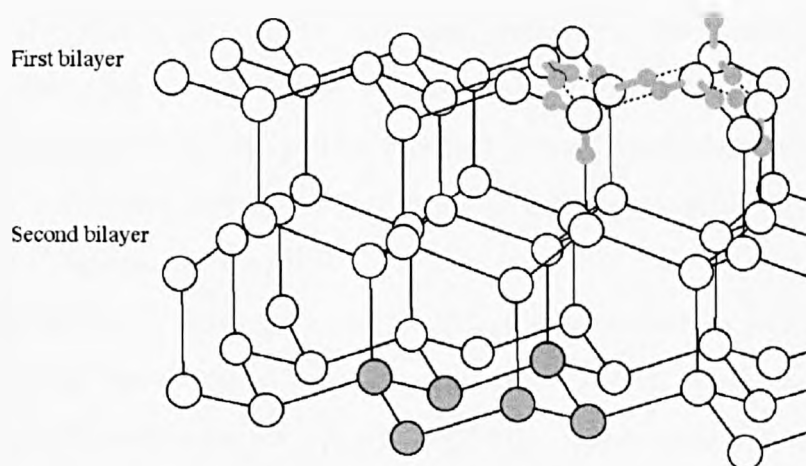
Figure 1.3: A schematic representation of bulk ice (Ih), showing the hexagonal ordering of the O atoms (circles) in contrast to the random ordering of the protons (top-right).

Importantly, while the O atoms in Ih form a periodic pattern, the H atoms are arranged randomly within the confines of the BFP ice rules [14]. This inherent disorder in the orientations of the protons in a hydrogen-bonded network of Ih allows it to maintain a residual entropy (3.4 J K_{-1} per mole) at 0 K. In contrast to the disordered Ih phase, in 1986 Suga *et al.* [15] found that doping D_2O Ih with KOD or similar hydroxides produces a phase transition at 76 K whereby 64 % of the residual entropy is removed. They subsequently termed this ordered phase ice XI. A similar ordering of protons was envisaged for 2D ice layers adsorbed on a

metal surface by Doering and Madey [16]. Moreover, for very thick ice layers, they anticipated that proton ordering should to be reflected in a large work function change ($\Delta\phi$) [16].

1.3   Water Adsorption on Metal Surfaces

The following summary of the literature on water adsorption on well-ordered single-crystal metal surfaces is by no means definitive. For a fuller treatment of the vast literature on this topic, the reader should consult the well-known reviews of Thiel and Madey (pre-1987 literature) [1] and Henderson (pre-2002) [13]. In addition, a detailed and up-to-date review of recent progress in this area is provided by Hodgson and Haq [17].

The adsorption of water on a metal surface is essentially a Lewis acid-base interaction, with water acting as an electron donor (Lewis base) and the metal surface as an electron acceptor (Lewis acid) [1]. Consequently, there is a net transfer of charge to the surface upon adsorption. Importantly, interaction with the surface has only a slight effect on the internal bond angles, bond lengths and vibrational frequencies of the water molecule, compared to the gas phase values. Furthermore, while the BFP ice rules are an adequate description of the arrangement of the water molecules in bulk hexagonal ice, additional constraints are necessary when considering ice films adsorbed on a metal surface. These constraints were formulated by Doering and Madey [16] in 1982 and are generally referred to as the surface modification rules. According to these rules, water adsorbs on the metal surface via the lone pair orbitals of the oxygen atom. Secondly, the tetrahedral arrangement of water in bulk ice is preserved for adsorbed water, even for 2D clusters and incomplete layers. Thirdly, each water molecule should bind to the system by a minimum of three bonds, which may be hydrogen bonds to other water molecules or lone pair bonds to the metal substrate. Finally, all

free oxygen lone pairs are forced into orientations that are perpendicular to the metal surface (figure 1.4).

As water adsorbs on a metal surface there is often a competition between maximising adsorption to the metal substrate and optimising the water-water hydrogen-bonding network. Indeed, this competition between water-water and water-metal interactions is responsible for much of the remarkably diverse adsorption behaviour observed for this seemingly simple substance [13]. On a given metal surface, water may adsorb intact, dissociate (partially or totally), cluster, or form 3-D crystallites. Generally, water clustering on a metal surface is favoured by weak water-metal interactions and rapid surface diffusion of water (allowing water molecules to locate each other). In contrast, a strong water-metal interaction means that the water molecules adopt a more rigid adsorption configuration, making water-water hydrogen bonding less significant. Having said this, one must also consider the kinetic processes in these interactions. For instance, at very low temperatures (e.g. 30 K) clustering may not occur even though the water-water interaction may be greater than the water-metal, since the clustering process is thermodynamically favoured but kinetically trapped. Similarly, at very low coverages diffusion is slow and clustering less favoured [13].

1.3.1   Adsorption and Wetting of Ru (0001)

Early studies of the water/Ru (0001) system[18][10] reported the appearance of a dim, halo-like ESDIAD pattern, for coverages below 0.2 monolayers, which changed to a hexagonal pattern upon further water adsorption. The thermal desorption spectrum showed a three-peak profile with peaks appearing at 210, 180, and 170 K. The adsorption peak at 210 K was assigned to the wetting layer, directly chemisorbed on the metal surface. While this peak saturated with increased adsorption, the lowest temperature state (170 K) continued to grow with increasing water coverage, without saturating and was consequently attributed to

multilayer adsorption. Moreover, for H_2O coverages of a monolayer and above, a faint and diffuse $(\sqrt{3} \times \sqrt{3})R30°$ pattern was observed in the LEED. The ESDIAD and LEED patterns were taken as evidence of the formation of hydrogen bonded clusters with specific long-range order. Crucially, these early studies noted that adsorbed water films are highly susceptible to electron damage [10].

A more detailed study of water adsorption on Ru (0001) was carried out by Doering and Madey [16] in 1982. In this impressively comprehensive study, they used a combination of TPD, LEED, ESDIAD and Auger electron spectroscopy (AES) to investigate the adsorption of water on a clean as well as an oxygen pre-covered Ru (0001) surface. These authors argued that the close match between the lattice parameters of Ru (0001) and ice allows for the formation of near-epitaxial 2D H_2O layers. Subsequently, they proposed a hexagonal ordered structure as the wetting structure on Ru (0001). The arrangement of the water molecules in this structure is based on a 2D plane of bulk Ih (figure 1.4) in accordance with the BFP ice rules [11] [12] and the surface modifications [16].

The resulting model (figure 1.5) assumes that adsorbed water molecules form a tetrahedral arrangement (similar to ice Ih) in which water molecules bind on top of the Ru atoms via one of their oxygen lone pairs, forming a chemisorbed layer. This water layer is in turn hydrogen bonded to a slightly higher layer of water molecules, with three hydrogen bonds per water molecule. In addition, all the second-layer molecules have their non-hydrogen bonded OH groups pointing along the surface normal while binding to the first-layer molecules via three hydrogen bonds. This configuration subsequently became known as the 'bilayer model' (figure 1.5) and is often referred to as a "puckered" bilayer because each O atom in the hydrogen bonded network is vertically displaced from its nearest neighbour by ca. 0.97 Å , giving the bilayer a characteristic corrugation. This bilayer arrangement allows the water to preserve its tetrahedral geometry and a complete bilayer is expected to show a $(\sqrt{3} \times \sqrt{3})R30°$ superstructure in LEED with an ideal coverage of θ
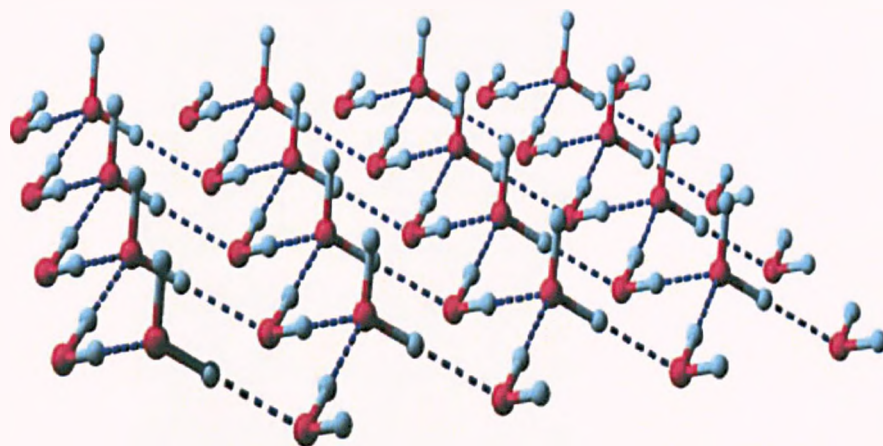
Figure 1.4: Schematic of a 2D plane of crystalline ice based on the BFP ice rules. The blue spheres indicate hydrogen while the red spheres represent oxygen. The dashed lines show the hydrogen bond interactions.

= 2/3 ML. Furthermore, the unit cell for this structure contains three Ru atoms and two H_2O molecules, one in each layer[16]. The bilayer model has endured for almost two decades as the established representation of water adsorption on metal surfaces but in recent years theoretical and experimental studies have cast increasing doubt on the thermodynamic viability of this configuration. Indeed, the enduring orthodoxy around adsorption of a water monolayer on a close packed metal surface has given way to speculation, debate and controversy.
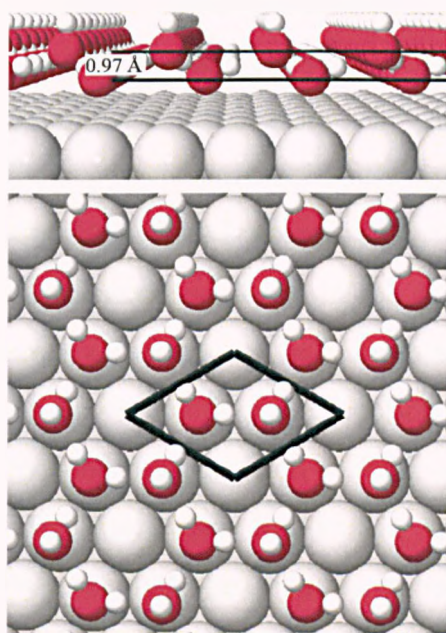
Figure 1.5: The bilayer model proposed for water adsorption on close packed metal surfaces. Water molecules (oxygen red spheres and hydrogen white spheres) bind atop the metal surface (grey spheres) forming cyclic hexamers with free hydrogen atoms pointing towards the vacuum.

A little over a decade after the proposal of the bilayer model, Held and Menzel [3] performed the first complete LEED I-V analysis of this system. Surprisingly, instead of the expected 0.97 Å difference in height between adjacent O atoms, as found in bulk ice, they found a much smaller vertical displacement of just 0.10

Å ± 0.02 Å . Their findings implied that rather than being a buckled bilayer, the wetting layer is closer to an almost coplanar monolayer. Furthermore, they observed that the buckling of the fist layer of Ru atoms is anti-correlated to the O height, leading to quite different Ru-O distances for the upper (2.23 ± 0.02 Å) and lower (2.08 ± 0.02 Å) water molecules [3].

The unusual conclusions from the LEED IV simulations led Feibelman to perform the first thorough theoretical analysis of this system[19]. In this much-cited study, he performed *ab initio* calculations based on density functional theory (DFT) in the generalized gradient approximation (GGA) for a monolayer of D_2O . The results from these calculations suggested that the traditional water bilayer is energetically unfavourable and should not even 'wet' the metal surface. On the other hand, wetting would become more energetically favourable after the removal of the non-hydrogen bonded (dangling) D atoms of the conventional bilayer. Severing the D atom of an upper water molecule in the bilayer arrangement, forces the O $2p_z$ orbital to become a high energy orbital unless it moves close enough to the surface to interact with the metal wave functions. The outcome of this is a thermodynamically favourable configuration consisting of a monolayer in which half the water molecules are dissociated. In addition, the intact water molecules and the hydroxyl fragments are hydrogen bonded to each other within a hexagonal structure. As for the single D atom resulting from the dissociation of the upper water molecules, Feibelman [19] argued that these will most likely remain on the surface, probably in the centres of the D_2O - OD hexagons or alternatively on bare patches of the metal surface. The formation of a partially dissociated wetting layer would explain how water forms a wetting layer on the Ru (0001) surface, as opposed to 3D bulk ice mounds. What is more, this structure has only a tiny corrugation of 0.05 Å and is therefore consistent with the near co-planarity found in the LEED IV simulations [3].

The DFT calculations of Peter Feibelman initiated a frenzy of interest in wa-

ter adsorption on the Ru (0001) surface. Puisto *et al.* [20] reanalysed the original LEED IV data, taking into account Feibelman's model of a partially dissociated wetting structure. Nevertheless, the best-fit geometry from the LEED IV reanalysis still favoured the original model of an almost coplanar wetting layer, with H atoms adsorbed atop the higher O atoms. However, all the other coplanar structures examined, including Feibelman's structure were within the 19 % Pendry factor (R_p) error range and so could not be rejected outright. This was even more so when the single H atoms were adsorbed on other parts of the surface and not incorporated into the superstructure observed in the LEED. In contrast, based on the LEED IV reanalysis, these authors were able to preclude a buckled bilayer structure [20]. Conversely, in a subsequent study, Materzanini *et al.* investigated the electronic and geometric structure of the water bilayer on Ru (0001) using DFT based first-principles total energy calculations. These authors examined three intact bilayer structures and two dissociated ones. In agreement with Feibelman [19] they found that the half-dissociated structures are more energetically favourable than the intact ones [21].

A comparative study of the adsorption and dissociation of H_2O monomers and ice-like bilayers on Ru (0001) using DFT showed that H_2O monomers prefer to bind on atop sites with the dominant bonding interaction being between the H_2O $1b_1$ molecular orbital and the Ru dz^2 states [22]. It was argued that lower-lying molecules of an intact H_2O bilayer bond to the metal surface in a similar fashion. These authors also examined the barrier for the dissociation of an adsorbed H_2O monomer and a hydrogen bonded bilayer structure and found that monomer dissociation is $\sim$0.27 eV exothermic, with an activation barrier of 0.8 eV . However, this activation barrier was reduced to $\sim$0.5 eV when the water was incorporated into a hydrogen bonded network [22].

Recently, Clay and co-workers have carried out a number of comprehensive TPD, RAIRS and LEED studies of H_2O and D_2O adsorption on a clean and O

pre-covered Ru (0001) surface [23] [4]. From the thermal desorption measurements, these authors concluded that the higher temperature A1 peak at 210 K is due to decomposition of a mixed OH/H_2O phase, while the low temperature A2 peak at 175 K was assigned to desorption/decomposition of an intact monolayer. Importantly, the heating-rate, H_2O coverage and the presence of O or H were all found to be influential in the branching of the A1 and A2 peaks [23]. The RAIRS of intact H_2O monolayers adsorbed at 155 K exhibited an OH stretching band at 3390 cm^{-1}, a scissors mode at 1630 cm^{-1} and librational (hindered rotation) band at 904 cm^{-1}. The presence of these IR bands implies that water forms a hydrogen bonded network. In contrast, adsorbing H_2O at 158 K, where it forms the partially dissociated phase responsible for the A1 peak in the TPD, resulted in the disappearance of both the OH stretching band at 3390 cm^{-1} and the scissors mode at 1630 cm^{-1}.

The coadsorption of O and H_2O produced a similar IR spectrum to that of the dissociated H_2O phase, implying a similarity in the structures formed by H_2O decomposition and O/H_2O coadsorption. The reaction of D_2O with O to form a flat OD/D_2O structure also led to a disappearance of the OD stretching bands. The presence of the OH stretching and H_2O scissors modes for the intact water structures and their subsequent disappearance upon formation of the A1 structure suggests that the water molecules of the A1 structure are no longer in an upright and dipole active geometry on the surface. This is consistent with partial dissociation to form a mixed OH/H_2O overlayer that lies parallel to the surface. From the IR spectra and the kinetic behaviour of the films, these authors concluded that below 155 K water forms an intact wetting layer on Ru (0001), which dissociates upon heating (in competition with desorption) to form a more stable OH/H_2O structure [23].

In a subsequent theoretical study, Meng *et al.* [24] used *ab initio* molecular dynamics and full-potential calculation to generate the vibrational spectrum and

work function changes ($\Delta\phi$) for a pure D-up, pure D-down, half-dissociated and mixed D-up/D-down D_2O bilayer structures on Ru (0001). The pure D-up and pure D-down bilayers produced a $\Delta\phi$ of 3.01 and 0.4 eV, respectively, while the mixed bilayers produced a $\Delta\phi$ of 1.70, 1.54 and 0.82 eV for D-up/D-own ratios of 1:1, 1:2 and 1:3 respectively. In contrast, a half-dissociated wetting layer had a calculated $\Delta\phi$ of 0.34 eV. Based on the large difference in $\Delta\phi$ for the pure D-up and D-down bilayers, Meng *et al.* concluded that the wetting structure on this surface is a mixture of D-up and D-down water [24]. The calculated binding energies of these two structures were very similar (531 and 533 meV for D-up and D-down, respectively), while the inter-conversion barrier was just 55 meV. Moreover, the experimental work function originally reported by Held and Menzel for a D_2O monolayer on this surface (1.26 eV) did not match either the pure D-up or D-down bilayers. However, Meng *et al.* suggested that a $\Delta\phi$ close to the experimental value could be reproduced by assuming a D-up/D-down ratio of between 1:2 and 1:3.

Although this picture of a mixed D-up/D-down bilayer is certainly favoured by entropy effects, Feibelman recently found that, at 150 K, these effects are tiny, (of the order of $\sim$9 meV per molecule) and only make a small contribution to the overall free energy of the system [25]. Furthermore, while a mixture of D-up and D-down sites is expected to give a $(\sqrt{3} \times \sqrt{3})$R30° LEED pattern, the calculated binding energies of these structures are still below the sublimation energy of bulk ice and would therefore not be expected to wet the Ru (0001) surface. The calculated sum frequency generation (SFG) vibrational spectra showed a peak at 2710 cm^{-1}. This feature, attributed to the free OD stretch, was intense for the D-up bilayer and weaker for the D-down. In contrast, RAIRS[4] and SFG [26] show that this high frequency OD stretch is largely absent from the spectra up until the saturation of the first layer.

Thermal desorption measurements by Denzler *et al.* [27] found that the yield

of D_2 for D_2O was a factor of ~ 26 lower than that of H_2 for H_2O . This suggested either, a different degree of dissociation for D_2O and H_2O or different recombination kinetics for H and D. These authors argued that these results supported a partially dissociated phase as the wetting layer on Ru (0001). Moreover, they suggested that the kinetics resulting from different long-range order found in LEED for H_2O and D_2O [28] could explain the different yields found in the TPD measurements. However, this interpretation was contradicted by subsequent SFG experiments [26] by the same authors. The vibrational spectrum for a D_2O layer showed three IR bands at 2729, 2290 and near 2550 cm^{-1}. The band at 2729 cm^{-1}, which was assigned to the free OD stretch, appeared abruptly as the first water layer saturated. In contrast, the other two bands, associated with the OD stretch of hydrogen bonded water molecules, were visible as the monolayer grew. Moreover, for a partially dissociated layer DFT had predicted a band near 2000 cm^{-1}, which was clearly absent in the SFG spectrum. Consequently, these authors proposed an intact bilayer arrangement consisting of a large proton disordered unit cell where every second water molecule has a hydrogen-metal bond, forming an 'H-down' structure [26].

Denzler's interpretation of the IR spectra was criticised by Feibelman [29] who argued that it is largely the O-O distance that determines the OD stretch frequency and so the D_2O adlayer's stretch spectrum only reflects its O-O distances rather than giving any information about the proportion of intact versus dissociated molecules. Moreover, Denzler's assignment of the D_2O structure as a D-down bilayer can not account for the discrepancy between the O-Ru separations found in DFT calculations and those obtained from LEED IV [3][29].

Andersson *et al.* carried out XPS studies of H_2O /D_2O monolayers adsorbed at 150 K and 180 K [30]. For H_2O /D_2O layers grown at 150 K, the XPS showed a single broad peak at 533.0 eV , characteristic of intact adsorption. However, on increasing the x-ray exposure, a second peak appeared at 530.8 eV . This

peak indicates the presence of OD/OH fragments, implying electron damage of the water layer leading to dissociation. The adsorption of H_2O at 180 K also produced an XPS signal characteristic of OH. This confirms that the formation of a partially dissociated structure is responsible for the A2 feature consistently observed in the TPD [23]. In contrast, the adsorption of D_2O at 180 K under the same conditions, showed less signs of dissociation. This is consistent with an activated dissociation of water, with a strong isotope effect between D_2O and H_2O [30]. However, a subsequent XPS study of this system by Weissenrieder *et al.* [31] seemed to conflict with these findings. In contrast to Andersson *et al.* , these authors found that the presence of H_2O , D_2O and OD/OH features in the XPS was independent of the coverage as well as the adsorption temperature. The implication was that dissociation occurred even at low temperatures. Indeed, at temperatures between 105 and 178 K they obtained a H_2O (D_2O):OH(OD) ratio of about 5:3 from the XPS intensities. This was interpreted in terms of a non-stoichiometric, partially dissociated structure [31].

In an attempt to clarify this conflict between the two XPS studies, Faradzhev *et al.* [32] carried out XPS and TPD measurements of H_2O and D_2O layers, before and after controlled electron irradiation. In agreement with the conclusions of Andersson *et al.* , [26] Hodgson *et al.* [23] and Nilsson *et al.* [30], they found that both species form molecular wetting layers at low temperatures. They also confirmed the findings of Clay and co-workers [23] that H_2O undergoes thermal dissociation while D_2O stays molecular during the desorption process. Moreover, they observed a high electron damage cross section for both the H_2O and D_2O layers. Consequently, it was proposed that inadvertent electron damage of the water layer was most probably responsible for the conflicting XPS studies of Andersson *et al.* [30] and Weissenrieder *et al.* [31] [32].

1.3.2 A Structural Isotope Effect between H_2O and D_2O ?

A difference in the TPD behaviour of D_2O and H_2O was initially reported by Schmitz *et al.* [33] [34]. In addition, Held and Menzel noticed during LEED IV measurements that D_2O layers gave a well-ordered $(\sqrt{3} \times \sqrt{3})R30°$ LEED pattern whereas H_2O layers under the same conditions produced a streaky/striped LEED pattern, which they attributed to ordered domains [3] [35] [28]. Consequently, these authors concluded that the different LEED patterns were due a structural isotope effect between D_2O and H_2O , which is surprising since no such isotope effect is observed in ice [35] [28]. Contrary to Held and Menzel, Haq *et al.* re-examined the adsorption behaviour of H_2O and D_2O on a clean Ru (0001) surface using low current LEED [4] and found that the LEED patterns of H_2O and D_2O are identical. This was the case, as long as the temperature was low enough (below ~160 K) to prevent H_2O dissociation. Heating the H_2O layer to above 160 K, or equally, exposing it to the LEED beam for extended periods and then heating to 150 K produced complex LEED patterns, very similar to those originally observed by Doering and Madey [16]. Haq *et al.* concluded that these LEED patterns are most likely due to domains of the partially dissociated $OH/H/H_2O$ structure [4].

1.3.3 Summary

The current experimental consensus for water adsorption on the Ru (0001) surface is that, at low temperatures, water adsorbs to from an intact molecular layer [23, 26, 30, 32]. Furthermore, H_2O and D_2O layers exhibit a dramatic kinetic isotope effect whereby D_2O desorbs intact and H_2O undergoes partial dissociation upon heating [23, 30, 32]. This isotope effect together with the sensitivity of the water structures to the preparation conditions and the high cross-section for electron damage, helps to explain much of the apparently contradictory experimental detail in the literature [3, 10, 16, 18, 28, 33–40]. However, despite this experimental consensus, key questions remain regarding the nature and structure of the intact

and dissociated phases. Most importantly, it is still not very clear how an intact water layer wets the surface [23, 26, 30, 32] when DFT calculations show that its binding energy is lower than sublimation energy of bulk hexagonal ice [19, 21, 22, 41].

1.3.4 Adsorption and Wetting of Pt (111)

After the Ru (0001) surface, water adsorption on the Pt (111) surface has been the most studied water/metal system. Early thermal desorption studies reported that water adsorbs intact at monolayer coverage. The corresponding TPD showed a single monolayer desorption peak near 160 K with a profile characteristic of zero order kinetics [42]. Further water adsorption led to the formation of multilayer clusters, giving a desorption peak, 10 K lower than the monolayer peak. The UPS and XPS spectra [42] showed broad IR bands characteristic of hydrogen bonded structures, even before the completion of the monolayer, indicating intact molecular adsorption [43]. Early LEED studies observed a $(\sqrt{3} \times \sqrt{3})$R30° pattern following water adsorption at ~125 K and concluded that water forms a commensurate hexagonal bilayer [44].

This picture of a simple commensurate structure on Pt (111) was challenged by the first application of STM to this system, which found that water initially decorates step edges by forming chains of hydrogen bonded species at the top site [45][46]. Subsequent He scattering experiments by Glebov *et al.* confirmed the presence of long-range registry between water and Pt (111) [47]. Instead of a simple $(\sqrt{3} \times \sqrt{3})$R30° structure, these authors observed that water adsorption initially forms domains of a $(\sqrt{37} \times \sqrt{37})$R25.3° structure, which is then replaced by a $(\sqrt{39} \times \sqrt{39})$R16.1° phase as the first layer saturates. The formation of these highly ordered epitaxially rotated phases were confirmed in several LEED studies by Haq and co-workers [48] [49] [50]. Furthermore, for water layers grown at 135 K, where water is relatively mobile, these authors observed a $\sqrt{37}$ LEED

pattern for coverages even as low as 0.1 of a monolayer. This suggests that water aggregates to form hydrogen bonded islands even at low coverage. They also found that the $(\sqrt{3} \times \sqrt{3})R30°$ LEED pattern previously reported for this system *only appears when the water film is subjected to high electron doses* [49], or when H_2O is co-adsorbed with a tiny amount of oxygen . Consequently, they concluded that previous reports of a $(\sqrt{3} \times \sqrt{3})R30°$ LEED pattern were most likely due to electron damage, leading to the formation of OH, which then pins the mixed OH/H_2O film into a simple $\sqrt{3}$ registry with the Pt (111) surface. Moreover, while the proposed commensurate $\sqrt{3}$ structure on Pt (111) would have a lateral expansion of 6 % relative to a bulk ice bilayer the $\sqrt{37}$ phase is only slightly expanded 3.6 % compared to bulk ice. The $\sqrt{39}$ structure on the other hand is believed to be compressed by 4.4 % relative to a bulk ice bilayer [49][50].

The IR spectra of saturated D_2O and H_2O $\sqrt{39}$ monolayers exhibited a very broad feature in the OD (OH) stretching region [48–50]. These stretching bands showed a significant change of shape only with the inception of multilayer growth, which is consistent with formation of extended hydrogen bonded islands above 135 K. Moreover, a weak band was observed near 2721 cm^{-1}, indicative of the 'free' or uncoordinated OH stretch. However, this feature was relatively weak, which suggests that the water layer contains few free OH groups dangling into the vacuum.

1.4 Thesis Outline

This thesis is divided into an experimental chapter (chapter 2) and two results chapters (chapters 3 and 4). Chapter 2 provides a description of the experimental set up, including the generation and maintenance of ultra high vacuum (UHV) pressures, the production of clean well-ordered substrate surfaces, the methods used for dosing water and the surface probes and techniques employed in our

experiments. In chapter 3, we reappraise the growth of monolayer and multilayer water films on the Ni (111) surface using a combination of TPD, LEED and chloroform desorption measurements. In addition, a comparative work function study of ice films of various thicknesses grown on the Ni (111) and Pd (111) surfaces is provided. In the final chapter (chapter 4), we investigate the growth of intact water monolayer and multilayer structures on the controversial Ru (0001) surface by comparing the ordering of O and Ru, as examined by LEED, and that of the top layer of O and H, as probed by He atom scattering (HAS).

Chapter 2

Experimental

2.1 Introduction

Highly polished, well-ordered surfaces are extremely susceptible to contamination and so to have any control over the processes occurring on them, an ultra high vacuum (UHV) environment is necessary. The ability to generate very high vacuums preceded the ability to measure them, but with the introduction of the Bayard-Alpert ion gauge in 1950 [51], pressures as low as 1×10^{-11} Torr could be readily measured, heralding the birth of the ultra high vacuum era. In the actual generation of UHV conditions, there are a myriad of vacuum pumps available to the surface scientist, all with their advantages as well as drawbacks. Once acquired, UHV pressures must be continually maintained. In our chambers, UHV conditions are generally limited by water vapour and hydrogen. The deposition water vapour on the inner surfaces of the chamber walls and on the other material inside the chamber is an undesirable consequence of the chamber spending a period at atmospheric pressure. To desorb and pump away the unwanted water vapour, the entire chamber is baked to 150 °C for 48 hours upon returning to high vacuum pressures after each period of venting. Once UHV pressures are regained, any remaining water is removed by periodic flashing of a titanium sublimation

pump (TSP). With the chamber water-free, the base pressures are then limited by hydrogen embedded in the stainless steel walls of the chamber, which seeps out once the system is in ultra high vacuum. This problem was also reduced to a certain extent by the use of the TSP pump, which has a high pumping speed for H_2. All of the experiments in this thesis are carried out either in chamber 1, or in chamber 2, both described below.

2.2   Chamber 1

Chamber 1 (figure 2.1) consists of a standard, stainless steel UHV chamber, with base pressures of below 2×10^{-10} Torr. The chamber pressure is measured using a Bayard-Alpert ionization gauge [51] and pumping to UHV is achieved by a combination of a turbomolecular pump (170 l s^{-1}), an ion pump (270 ls^{-1}) and a titanium sublimation pump. In addition, an *Edwards 18* rotary oil pump provides a rough vacuum (1×10^{-3}) backing line for the turbomolecular pump. The principle probes on this chamber include a microchannel plate (MCP) low energy electron diffraction (LEED) unit (OCI, Canada), a quadrupole mass spectrometer (QMS), for the temperature programmed desorption (TPD) measurements, a Kelvin probe for the workfunction measurements and an ion gun (500 eV, 5 μA) for argon ion sputtering during the surface cleaning process.

2.3   Preparation of Clean, Well-Ordered Surfaces

The surfaces investigated in our experiments are, the Ni (111), Pd (111) and the Ru (0001) single crystals. These are typically circular in shape with diameters of around 9 mm and thicknesses of about 2 mm. The surfaces, which are polished to a mirror finish and with an alignment better than 0.3°, are purchased from the
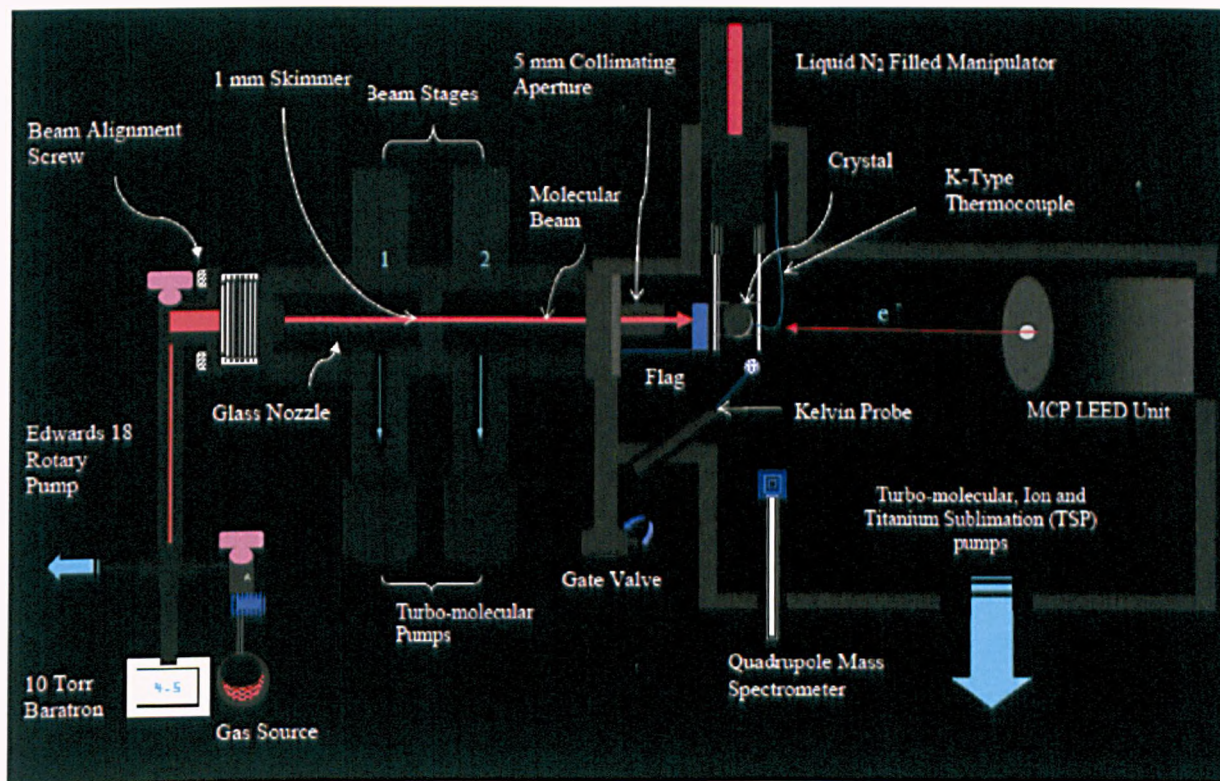
Figure 2.1: Schematic depiction of chamber 1, showing the MCP LEED unit, QMS and Kelvin probe. Gases are dosed using a two-stage effusive molecular beam that passes through a skimmer and a collimating aperture before entering the main chamber.

Surface Preparation Laboratory (*The Netherlands*).

Clean and well-ordered surfaces are consistently obtained by cycles of argon ion sputtering, which consists of bombarding the front face of the crystal with a well-defined beam of Ar^+ ions (500 eV) for 20 minutes, followed immediately by thermal annealing to 850 °C, to reorder the surface and remove any embedded argon. For a newly mounted crystal, the cleaning cycles are maintained for about three consecutive days. For the Ni (111) surface, we find that following the initial daily sputter-anneal cycle, high temperature flashing ($\geq$850 °C) is sufficient for producing a clean surface in between consecutive experiments (within a time limit of one day). The other surfaces, particularly the Ru (0001) require a sputter/anneal regime in between experiments. Surface cleanliness and ordering is generally confirmed by LEED patterns of the bare metal surface; a contamination-free substrate produces highly defined, pin-sharp LEED spots. A further confirmation comes from the TPD of a water monolayer, where the consistent production of a clean monolayer peak, without any further desorption peaks, is a reliable indicator of a clean surface.

2.4   Sample Mounting and Manipulation

In mounting the samples, two tantalum heating-wires (0.2 mm thickness) are spot-welded to either edge of the crystal. These wires are then welded to a pair tantalum support rods (2 mm thick), which are in turn mounted onto a differentially pumped Dewar-type manipulator via barrel connectors. This simple method of mounting the crystal requires far less material than constructing an elaborate sample stage and is, thus, less susceptible to undesirable out-gassing from the sample surroundings when annealing the crystal. Moreover, the sample can be accurately aligned to the effusive water beam by simply moving the cold crystal in front of the beam path and monitoring the changes in the partial pressure of

the chamber with the mass spectrometer. The greatest dip in pressure occurs when the middle of the sample is normal to the incoming beam and the maximum number of adsorbate molecules are sticking to the surface. In contrast, with traditional sample stages, which normally consist of a complex arrangement of metal plates, adsorption is not confined to the sample alone and so the simple procedure described above cannot be used to align the molecular beam to the sample.

The temperature of the sample is monitored using a K-type thermocouple, spot welded to the back of the crystal and connected to an external digital meter. A direct current from a laboratory power supply is used to heat the crystal resistively to 850 °C during cleaning and to produce a steady temperature ramp during TPD measurements. After annealing, the crystal can be cooled rapidly to ≤ 100 K by filling a hollow metal cylinder inside the manipulator (Dewar) with liquid nitrogen, which cools (via conduction) the Ta support rods, then the heating-wires and finally the sample itself. Annealing the crystal from ≤ 100 K to ≥ 1100 K and cooling back to ≤ 100 K can be done in approximately 10-12 minutes. The manipulator provides 0-60 mm linear translation along the z direction, 0-25 mm travel along x and y, as well as 360° rotation about θ. Additionally, a special tilt mechanism at the base of the manipulator allows the crystal position to be adjusted further when aligning the surface to the LEED unit.

2.5   The Molecular Beam

The gases are dosed by means of a two-stage collimated effusive molecular beam. Each stage is pumped by a turbomolecular pump (330 l s^{-1} and 170 l s^{-1} first and second stages, respectively).The first stage has a typical base pressure of 2 $\times$ 10^{-6} Torr and the second stage can be pumped to as low as 2 $\times$ 10^{-9} Torr. An *Edwards 18* rotary oil pump (1 $\times$ 10^{-3} Torr) provides a rough vacuum backing line for the beam-stage pumps. The standard procedure for dosing a gas on the

surface begins with the introduction of a beam of known pressure (typically 4.5 Torr), sourced from an external glass reservoir, into a glass nozzle with a 1 mm inner diameter (figure 2.2). On exiting the nozzle, the beam enters the first stage and then passes through a 1 mm aperture skimmer prior to entering the second stage. Upon entry into the second stage, the beam is incident onto a closed gate valve, preventing it from entering the main chamber. Opening the gate valve allows the beam into the main chamber through a final, 5 mm, collimating orifice. The effusive molecular beam is now incident on a metal flag that shields the crystal and which is only removed upon starting the (timed) dose. The molecular beam has a typical flux of 0.01 layer s^{-1}, controlled primarily by regulating the pressure of the gas in the source reservoir. Additionally, the beam collimation can be fine-tuned using screws on a bellows system that allow the glass nozzle to be moved in the x y z directions. With this collimated effusive beam, adsorbate gases can be accurately directed to produce adsorption areas of consistent size, in the centre of the crystal. This eliminates unwanted adsorption onto the back of the crystal as well as the sample stage, leading to higher quality TPD spectra. Indeed, by mounting the crystal using only two tantalum posts, without a sample stage, and delivering gases via a molecular beam we could ensure that ≥99% of the desorption signal in the TPD trace is actually from the crystal face. Moreover, adsorbate coverages can be determined with very good accuracy. In contrast, dosing via the background dosing technique produces a TPD trace that consists of desorption from the face of the crystal in addition to an undesired component from the back and sides of the crystal as well as the support posts, making it difficult to determine surface coverages with any accuracy. Due to the high sensitivity of the water/metal system to minute amounts of contamination, all the experiments are conducted using triply distilled H_2O and D_2O (99.9 % purity). Moreover, once the water is in the source reservoir, it is pumped for ~10 minutes using a rotary pump backing line (10^{-3} Torr), to remove any remaining O_2.

2.6 Molecular Beam Uptakes

Molecular beam uptakes and surface coverages are obtained using the well-known King and Wells technique [52], which is shown schematically in figure 2.2. Prior to the time t_o, the mass spectrometer only registers the background partial pressure of the chamber. However, with the introduction of a collimated effusive molecular beam at t_o, there is a sudden rise in pressure (P_0). The partial pressure is a ratio of the beam flux to the pumping speed of the chamber, so provided that these are kept constant it will remain at this new level. Once the flag shielding the (cold) crystal surface is moved out of the water beam's path, the molecules in the beam adsorb on surface, corresponding to a sharp drop in the pressure (P_1). Initially, nearly all of the impinging molecules adsorb (stick) on the surface but as the number of unoccupied adsorption sites decrease with time, more and more molecules are reflected from the surface and the pressure will begin to climb steadily. Finally, as the flag is repositioned in front of the crystal at t_f, the partial pressure rises again.

The sticking probability, S, which is an index (between 0 and 1) of the ability of a surface to adsorb impinging molecules, is extracted from the ratio of the rate of adsorption to the initial rate of bombardment as shown below:

$$S = \frac{P_1}{P_0} \tag{2.1}$$

Moreover, provided that the beam flux and the pumping speed of the chamber remain constant, the total coverage, N (t), is then given by:

$$N(t) = F \int_0^t S(t)dt \tag{2.2}$$

Where F is the flux of the molecular beam. In addition, absolute coverages can be determined by calibrating the relative coverage obtained from equation 2.2
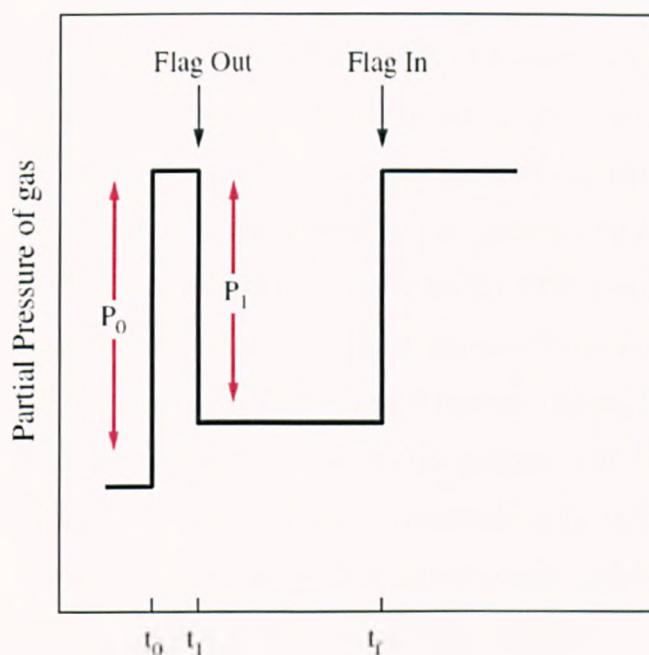
Figure 2.2: A schematic representation of the King and Wells experiment for determining sticking probabilities. See text for further details.

against the integral of the beam uptake for a known absolute coverage. In this thesis, the calculated coverages are given with respect to the density of atoms at the metal surface, where one monolayer (ML) is equal to one adsorbate per metal atom.

2.7 Temperature Programmed Desorption

The TPD spectra in this thesis are generally produced by dosing the desired film onto the (cold) clean crystal surface (typically 135 K) via a collimated molecular beam, the exception being the helium scattering experiments where a collimated leak-valve doser was also used to direct gases onto the crystal face. Upon the adsorption of the desired film, the crystal is heated resistively at a steady tem-

perature ramp (typically 1 K s^{-1}) and the pressure changes, in the constantly pumped chamber, recorded using a quadrupole mass spectrometer connected to an external computer. A subsequent plot of the rate of desorption as a function of the temperature yields qualitative information about the nature of the adsorption process (i.e. intact or dissociative) as well as the presence of contaminants. For instance, the TPD of an intact D_2O monolayer on Ru (0001) shows one monolayer peak (figure 2.3) while a dissociated monolayer has an additional peak arising from the recombination of the partially dissociated structure (figure 2.4). Furthermore, since species that are less strongly bound to the surface will desorb before more strongly bound adsorbates, relative binding energies can be inferred from the relative positions (in temperature) of the desorption peaks. Additionally, the peak profile can be used to classify the desorption rate as zero, first or second order. For adsorbed water layers, the TPD spectrum is extremely useful for deducing surface wetting or non-wetting. The TPD spectrum for water adsorption on the Ni (111) surface produces a higher temperature peak that saturates with further adsorption, followed by a lower temperature peak that continuous to grow with further adsorption without reaching saturation. From this, we can deduce that water wets the Ni (111) surface forming a complete monolayer before the onset of multilayer adsorption.

Provided the chamber pumping speed remains constant, the integrated area under the TPD peak(s) is directly proportional to the initial surface coverage, before the onset of desorption, thus providing a simple method of obtaining relative coverages. More importantly, absolute coverages can be obtained by calibration against the integrated area under the desorption peak of a known absolute coverage. For example, the $(\sqrt{3} \times \sqrt{3})R30°$ LEED pattern observed for water adsorption on the Ru (0001) surface is brightest for a surface coverage of 0.67 layers. The integrated area under the resulting TPD trace can then be taken as an absolute coverage 0.67 ML and other relative coverages calibrated against this
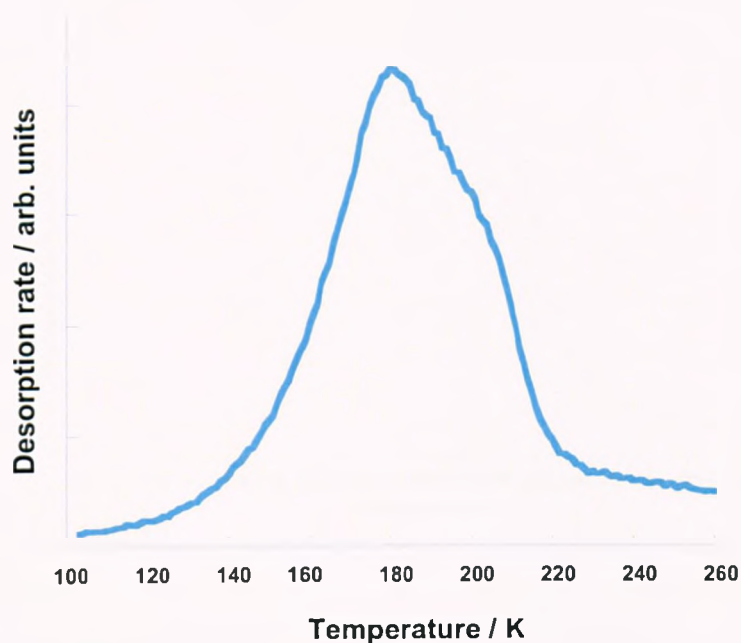
Figure 2.3: A typical TPD profile for an intact monolayer (ML) of D_2O from Ru(0001).

value.

2.8   Low Energy Electron Diffraction

In a modern surface science laboratory, a LEED system is a primary tool of the UHV chamber since it provides instant qualitative information concerning the unit cell geometry including size, shape and the presence of long-range order. Moreover, a quantitative and more powerful use of the LEED apparatus is to scan the electron energy whilst recording the fluctuations in the intensity of the diffraction spots. These intensity fluctuations, when plotted as a function of the incident electron energy generate an intensity versus voltage (LEED I-V) spectrum. Subsequent comparison of the experimental curves with those generated from theoretical models can yield quantitative information regarding the position of atoms
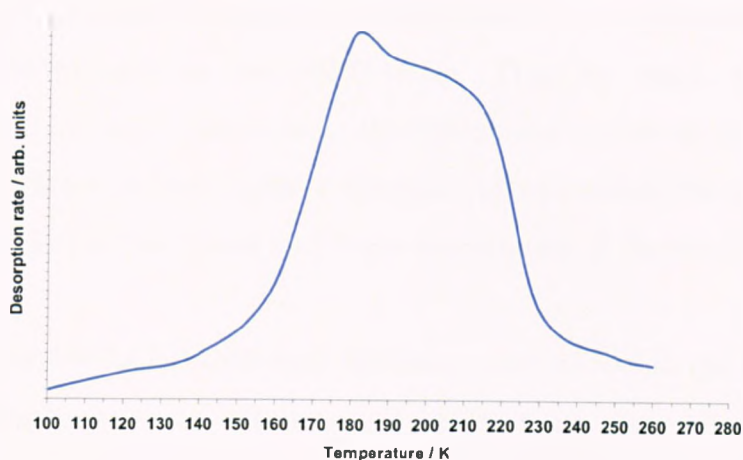
Figure 2.4: The TPD profile from a partially dissociated D_2O monolayer on Ru (0001.

(surface structure), bond strengths and bond angles. Despite these strengths, the LEED technique is not without its limitations, for example, because the probing electrons are diffracted from the electron density of the surface atoms they are sensitive to large atoms with high electron densities such as oxygen but virtually blind to lighter atoms such as hydrogen. This is particularly a problem for water adsorption on metal surfaces where we are interested in the relative positions of the H atoms.

2.8.1   The Low Current LEED Unit

The LEED data in this thesis is obtained using a low-current micro-channel plate (MCP) LEED unit (OCI, Canada) with a beam energy range of 5-3000 eV , a beam current range of 20 pA-200 nA and a maximum gain voltage of 3 kV. A spot size with a diameter of approximately 1.80-2.00 mm was measured for the electron beam. This was achieved by dosing a monolayer of water onto the Ni (111)

surface and then deliberately exposing the ensuing $(2\sqrt{7} \times 2\sqrt{7})$R19° structure to very high beam currents, leading to a consistent 2×2 pattern that is limited to the area restructured by the LEED beam. Thus, by simply translating the crystal in the x and y directions using the micrometer screws on the manipulator in addition to linear motion in the z direction, we can obtain the size of the area destroyed by the electron beam and hence an estimate of the electron beam spot diameter.

For decades, the LEED technique has been a central tool in the understanding of crystallographic systems. However, in recent years more scrutiny has been focused on the unwelcome influence of the electron beam on the adsorbate under investigation. This is particularly relevant in the application of LEED to delicately adsorbed films such as water. With our OCI LEED unit, we can probe delicately adsorbed water structures using beam currents of between 20-30 nA and never above 60 nA. This is considerably lower than that used in previously reported LEED experiments on adsorbed water. For instance, Held and Menzel in their 1994 LEED-IV study of water adsorption on Ru (0001) used beam currents in the range of 100-300 nA [3].

2.9 Workfunction Measurements

The possibility of measuring contact potential differences was first postulated by Sir William Thomson (later Lord Kelvin) in 1898 and subsequently published in the Philosophical Magazine [53]. Three decades later, a more advanced probe for measuring workfunction changes was developed by Zisman [54]. The probe used in our workfunction experiments, consists of a 3 mm Au grid, which is in turn attached to a piezo-ceramic rod at the end of a feed-through inside the UHV chamber that can be driven forwards and backwards. After the adsorption of the desired film, the Kelvin probe is driven toward the surface to within a typical

working distance of 0.5 mm. The sample position is then adjusted using microm-
eters on the manipulator so that the probe is parallel to the crystal surface. An
alternating current from an external control box is then used to oscillate the probe.
The vibrating frequency of the probe can be accurately controlled and the signal
monitored with an oscilloscope. Once the Kelvin probe is oscillating at the desired
frequency in front of the surface, the crystal is annealed at a steady temperature
ramp and the TPD and the workfunction change recorded simultaneously on an
external computer.

2.10   The Helium Scattering Set-Up

Helium diffraction experiments can provide information on the dimensions of the
unit cell from the angular location of the diffraction peaks while the intensity
distributions in the spectra give important information about the distribution of
the scattering centres. Since the neutral He atoms interact only weakly with the
surface this technique is conveniently non-destructive, in addition to its surface
sensitivity. Moreover, because the He atoms are diffracted from the repulsive
potentials of the surface atoms some distance above the surface, the He beam is
uniquely sensitive to H, which is not visible in LEED due to its relatively small
electron density. Consequently, helium atom scattering (HAS) is an exceptionally
powerful tool for investigating delicate adsorbate over-layers that are vulnerable to
undesirable damage when using more intrusive probes. For instance, water films
on metal surfaces have traditionally been studied using LEED but in recent years
there has been increasing concern that patterns of ordered water structures may
in fact be electron beam induced. In this thesis, we apply helium atom scattering
(HAS) to water adsorption on the Ru (0001) surface concurrently with the LEED
technique.

2.11 Chamber 2

The HAS experiments are performed in an ultrahigh vacuum (UHV) chamber, with base pressures below 5×10^{-11} Torr. In addition to the HAS apparatus described below, the main chamber was equipped with a low current LEED system, based around a dual microchannel plate (MCP) amplifier. To ensure against inadvertent electron beam damage, the beam current was kept low (below 30 nA) at all times and the exposure time to the absolute minimum necessary. With these conditions, we can maintain stable ice structures for the duration of the experiments.

The Ru crystal is aligned to within $\pm$ 0.25° of the (0001) face and cleaned by repeated cycles of Ar^+ ion sputter followed by thermal annealing (1100 K). The crystal is attached via Ta heating wires to liquid nitrogen cooled Ta support posts, allowing it to be heated to 1400 K and cooled to 90 K within a few minutes. The surface temperature is measured using a K-type thermocouple spot welded to the back of the crystal and controlled via computer feedback to a DC heating supply, allowing the temperature to be ramped linearly for TPD measurements. Surface cleanliness is judged primarily from the D_2O desorption behaviour and LEED patterns of the ice monolayer, which are very sensitive to surface contamination. Mounting the Ru crystal directly on the heating wires ensures that nothing except the sample desorbs gas during heating measurements, allowing accurate assessment of the quality of the water layer.

To highlight the critical role of the preparation on the resultant ice structure, water layers are grown using two separate experimental arrangements. The first method involves dosing with a molecular beam (figure 2.5). The beam flux is typically on the order of 0.005 layers s^{-1} and creates a pressure increase of $\leq 2 \times 10^{-11}$ Torr in the chamber, during adsorption. A retractable flag is placed in front of crystal allowing for accurate control of the surface exposure to the molecular beam. For D_2O , the water coverage was obtained by directly measuring the up-
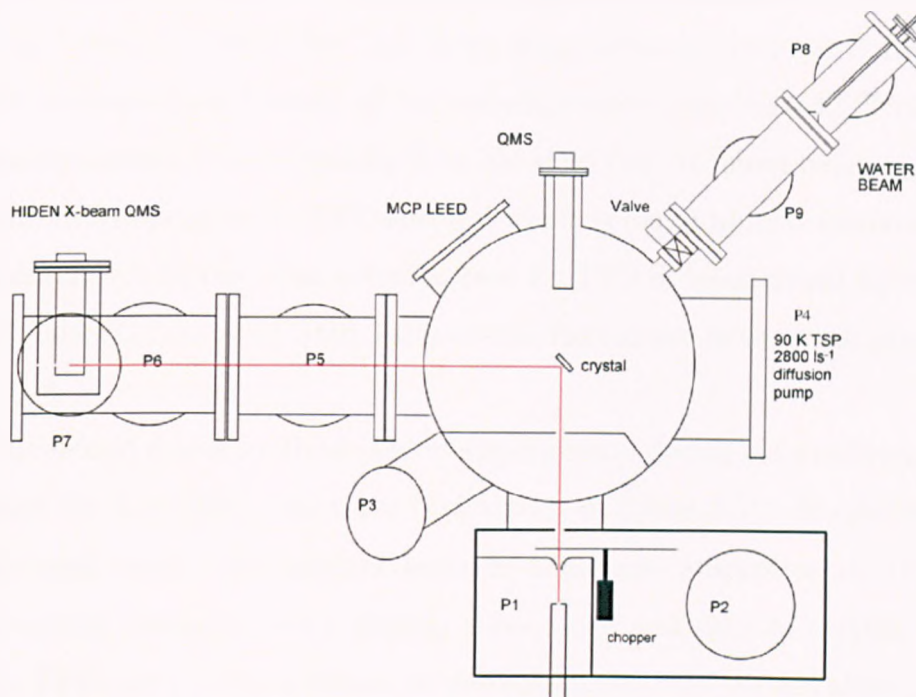
Figure 2.5: Schematic diagram of chamber 2. The chamber is separated into four main sections: the helium source and chopper chambers, the main experimental/scattering chamber, the detector path chambers and the molecular beam section. The helium atom source consists of a temperature-controlled nozzle with differential pumping (P1, P2 and P3) by 9", 6" and 6" diffusion pumps respectively. The detector arm is at a scattering angle of 90° and contains a cross beam QMS, triply differentially pumped by turbomolecular pumps (P5, P6), themselves backed by diffusion pumps, and an ion pump (P7), giving base pressures in the low 10^{-11} Torr range. The water beam consists of an effusive glass nozzle, pinhole skimmer and collimating aperture, differentially pumped by $240 \, l \, s^{-1}$ turbo pumps (P8 and P9), and is arranged so that the water beam just fills the crystal surface. The main chamber is also equipped with a variable leak valve and collimated tube doser (not shown). Further details can be found in the text.

take required to form a saturated ice monolayer at the surface, using the King and Wells direct reflection technique [52]. The TPD spectra provide a second measure of the water coverage by calibrating against a saturated monolayer (defined here as 1 layer of water). For H_2O films, dissociation of the layer during heating makes accurate measurement of the coverage more complicated. Typically, the saturation coverage is determined from the dose time required before appearance of a multilayer peak in the TPD spectra, which is found to be consistent with the D_2O dosing conditions. The detector used for TPD of beam-dosed layers, was an unshielded VG Smart-IQ QMS, located near the surface in the main experimental chamber.

The second dosing method used was background dosing via a collimating tube, supplied by a variable leak valve (not shown in figure 2.5). In contrast to the beam-dosed layers, this method leads to additional adsorption on the surface surroundings (support posts, heating wires, edge and sides of crystal, etc). To obtain TPD spectra characteristic of desorption from the surface alone, the QMS detector is used in a stagnation configuration, housed inside a retractable gas collection tube. Thus, water desorbing from the sample surroundings is shielded from entering the detector housing, whereas gas from the surface enters through a 4 mm hole placed directly in front of the sample. The TPD spectra obtained from this method are consistent with those from beam-dosed layers, with an additional time constant attributed to the time required to pump out the detector volume. This time constant was modelled and the tail removed from the TPD, allowing direct comparison with beam-dosed layers.

The HAS apparatus consists of seven independently pumped sections with the first chamber containing the He beam source. High purity helium (BOC) is supplied to the nozzle at a stable pressure of up to 10 bar and is then passed through a nitrogen-cooled coil to remove any remaining condensable impurities. The nozzle assembly is enclosed within a liquid nitrogen dewar, which, coupled with dc

resistive heating of the tip, gives a working temperature range of approximately 110 to 380 K. The nozzle temperature is stable to within $\pm$ 0.1 K, as measured by a K-type thermocouple spot-welded to the tip. This temperature range corresponds to beam energies of 26-80 meV, as confirmed by time-of-flight (TOF) measurements using the retractable chopper (figure 2.5). The He beam is incident at the centre of the crystal, mounted on a VG (x, y, z, θ) manipulator, whose axis can also be tilted relative to the scattering plane. The sample is mounted at the centre of the azimuthal rotation of the manipulator (θ), with the surface perpendicular to the incident beam. The incident and reflected beam paths are always fixed at 90° to each other and the crystal rotated about θ by a computer controlled stepper motor. The reflected beam leaves the experimental chamber through a 3 mm aperture and passes through two stages of differential pumping before entering the final sections containing the detector.

The final chamber contains the detector (Hiden HAL 301 Cross beam QMS) which is housed inside a separate section pumped independently by an ion pump (P7) for further reduction of background gas. The entrance to the mass spectrometer housing is a 3 mm aperture with the beam exiting through a 4 mm hole in the time-of-flight configuration. The final aperture can be blocked off to use the QMS as a stagnation detector, as is the case for the scattering data presented in this thesis. In stagnation mode the clean Ru surface gives a maximum reflected intensity of around 1.5×10^6 cps in the specular beam. The HAS measurements presented in this thesis are recorded at a tip temperature of 300 K, corresponding to an energy, incident wavevector and energy resolution of E = 65 m eV , k_i= 11.1 Å $^{-1}$ and $\Delta E/E$ of 7.0 %, respectively. The azimuthal orientation of the sample was initially set using LEED and then optimised using He diffraction from a (2 × 2)O overlayer.

Chapter 3

Monolayer and Multilayer Adsorption on Ni (111)

3.1 Introduction

While the interaction of water with close-packed transition metal surfaces has received a surge in interest in recent years, most of this attention has been on the Ru (0001) and Pt (111) surfaces. In contrast, the Ni (111) surface has received relatively little interest. The first study of the water/Ni (111) system was carried out almost three decades ago by Madey and Netzer [16]. Using a combination of LEED, TPD and electron stimulated desorption ion angular distributions (ESDIAD) they showed that water forms a stable wetting layer on this surface. The thermal desorption spectra (TPD) from water adsorbed on a clean Ni (111) surface showed an initial peak at 170 K that eventually reached saturation with further adsorption and which they attributed to the first wetting layer of water (the layer in direct contact with the metal surface). Following the saturation of this monolayer peak, a second peak grew at 150 K, but did not saturate even at very high coverages. This peak was ascribed to multilayer ice formation on top of the initial wetting layer. Importantly, the TPD spectra showed no evidence sug-

gestive of water dissociation on the surface, which is consistent with subsequent TPD studies[55]. At sub monolayer coverages, the LEED showed no ordered overlayer structures. However, upon completion of the first layer of water they observed a weak $(\sqrt{3} \times \sqrt{3})R30°$ LEED pattern [16]. In addition, the ESDIAD of the complete monolayer showed a broad H^+ distribution, with low intensity along the surface normal and no indication of a preferred orientation for the H atoms of the water molecules [16] [56].

Nobl and Benndorf [57] carried out UPS measurements, which showed three water induced emission peaks at 6.2, 8.5 and 12.3 eV below E_F, consistent with intact water adsorption. The same authors also performed angle and polarisation dependent measurements, which found no evidence for the existence of any long-range ordered bilayer structure and no preferred orientation of the H_2O axis, [57]. Moreover, workfunction measurements indicated that water adsorbs on the Ni (111) surface via the O atom [57]. *ab initio* calculations by Yang and Whitten [58] also suggested that H_2O binds via the O atom and found a Ni-O equilibrium distance of 2.06 Å . Moreover, these calculations implied that the hydrogen atoms of the water molecules point normal to the surface [58].

Pache *et al.* also observed a $(\sqrt{3} \times \sqrt{3})R30°$ LEED pattern for a complete monolayer and obtained a saturation coverage of 0.66 ± 0.05 ML from XPS [55]. The UPS spectra showed a splitting of the water $3a_1$ peak, which indicates the presence of two distinct types water molecules, both tilted from the surface normal. These authors attributed the phenomenon in the UPS spectra to the formation of commensurate $(\sqrt{3} \times \sqrt{3})R30°$ - $2H_2O$ bilayer with a similar structure as that proposed on the Ru (0001) surface [59]. However, this is inconsistent with the diffuse ESDIAD pattern reported by Madey and Netzer [16]. A $(\sqrt{3} \times \sqrt{3})R30°$ LEED pattern was also reported by Mundt and Benndorf [60]for a saturated layer on a stepped Ni (11,11,9) surface. However, on reducing the coverage, by annealing the surface to above 150 K, they observed that the $\sqrt{3}$ pattern changed to

a (2×2) pattern. This (2×2) pattern persisted up to 250 K, although it reached a maximum in intensity with the desorption of the surface water at 165 K. The transformation of the $\sqrt{3}$ pattern into a (2×2) pattern was interpreted as coverage and temperature dependent reordering of the water monolayer, however, they could not rule out the possibility of O or OH involvement.

Recently, Nakamura and Ito performed RAIRS experiments of water adsorbed on Ni (111) at 20 K as a function water coverage [61]. At very low coverages (0.03 ML) the IR spectrum showed a sharp D_2O scissors band at 1161 cm^{-1} and a weak stretching feature at 2474 cm^{-1}. These bands were attributed to the adsorption of a monomer D_2O molecule. The weak intensity of the symmetric OD stretching band at 2474 cm^{-1} relative to the sharp intensity in the scissors region is reminiscent of the behaviour observed on the Pt (111) and Ru (001) surfaces and presumably results from vibronic coupling to the metal surface. Moreover, from the relative weakness of the OD stretching band together with its large red shift, these authors inferred that the monomer lies flat on the surface. At higher coverages, the formation of D_2O clusters on the surface shifted the scissors band to a higher frequency and produced four strong bands in the stretching region between 2434 and 2696 cm^{-1}. These bands became very intense near 0.33 ML coverage but then broadened to form a red shifted band around 2540 cm^{-1} with the completion of the wetting layer at 0.67 ML [61]. The IR spectrum of the incomplete layer is in good agreement with that observed for low temperature adsorption on the Pt (111) and Ru (0001) surfaces under similar conditions and was attributed to the formation of cyclic hexamers [62].

While the literature [60] [13] for the water/Ni (111) system implies the formation of a commensurate $(\sqrt{3} \times \sqrt{3})R30°$ bilayer on this surface, recent reports have cast doubt on the validity of the conventional bilayer as a model for water adsorption on close packed metal surfaces. For example, DFT calculations indicate that the binding energy of the conventional $\sqrt{3}$ water bilayer is insufficient to

wet the Ru (0001) surface [19]. Similarly, on the Pt (111) surface, a commensurate $\sqrt{3}$ structure is only formed if there is O present to pin the water in registry with the metal surface [63][64]. Moreover, reports of commensurate $\sqrt{3}$ structures on these surfaces need to be treated with caution since recent studies [32] [30] have shown that LEED induced dissociation of water layers can lead to structures with $\sqrt{3}$ LEED patterns. Consequently, in the light of these developments, the hitherto supposed formation of a commensurate $(\sqrt{3} \times \sqrt{3})R30°$ phase on the Ni (111) surface requires reappraisal. In this chapter, we reinvestigate the formation of ordered structures on the Ni (111) surface above 135 K using a combination of low current LEED, TPD, workfunction measurements and chloroform desorption studies.

3.2 Experimental

The experiments are performed in a UHV chamber (chamber 1, chapter 2) with consistent base pressures of below 2×10^{-10} Torr. The principle tools on this chamber included an MCP LEED unit, a QMS and a Kelvin probe for workfunction measurements. The Ni (111) crystal is polished and aligned to better than 0.3° by the Surface Preparation Lab (*The Netherlands*). Clean and ordered surfaces are obtained by repeated cycles of argon ion sputtering and thermal annealing to 850° C. For a newly mounted crystal the sputter/anneal regime is maintained for 2-3 consecutive days. Surface cleanliness and ordering are confirmed by LEED patterns of a monolayer of water with additional confirmation provided by the TPD behaviour of a water monolayer. Following the initial 2-3 day cleaning process, the surface is only given an initial sputter/anneal cycle at the start of each day. For the remainder of the same day, an 850 ° C anneal is sufficient for producing a clean and ordered surface between consecutive experiments. The same procedure was also used to prepare the Pd (111) surface during

workfunction measurements (described below).

Gases are dosed via an effusive collimated molecular beam (see Chapter 2) with a typical flux of 0.01 layer s^{-1}. Relative water coverages are obtained from the time taken to form a saturated monolayer, using the King and Wells direct reflection technique [52]. Further coverage information is obtained by integrating the area under the desorption peaks. All LEED patterns are taken with a low current LEED unit based on a dual microchannel plate system. After dosing water at 135 K, the sample is cooled to below 100 K and the crystal aligned parallel to the LEED unit, which is driven to a typical working distance of 30-40 mm. As water films are only delicately adsorbed, there is always concern about the probing electrons of the LEED beam inducing unwanted damage or restructuring [32] [4]. The probability of inadvertent electron beam damage is reduced by using beam currents of 20-30 nA at all times. These conditions allow the water films to be probed for tens of minutes without any visible damage or restructuring. The LEED patterns are recorded manually using a Canon Mini DV camcorder and the images subsequently uploaded onto a computer.

Workfunction measurements are acquired using a Kelvin probe consisting of a 5 mm circular gold mesh. After the adsorption of the desired water film, the probe is driven toward the surface to a typical working distance of 0.5 mm. The probe is then oscillated in a periodic fashion using an alternating current from a Kelvin 07 control box and the frequency and the signal monitored with an oscilloscope. Following this, the earthed sample is annealed at a steady temperature ramp and the TPD spectrum and the workfunction change recorded simultaneously on a computer.

3.3 Results and Discussion

3.3.1 Temperature Programmed Desorption

The TPD traces for water layers of increasing initial coverage (0.2-3.2 layers) adsorbed on the Ni (111) surface are shown in figure 3.1. Initially, a peak grows at around 165 K but shifts to higher temperatures (~168 K) with increasing coverage. Upon further adsorption, this peak saturates and a new one begins to grow, initially at ~150 K. This lower temperature peak continues to grow with increasing coverage without reaching saturation. The initial higher temperature peak is due to the first wetting layer of water, adsorbed directly on the metal surface. The shifting of this peak to higher temperatures with increasing coverage seems to be at odds with simple first order desorption kinetics. Madey and Netzer [16] attributed this shift to the presence of attractive lateral interactions between neighbouring water molecules and suggested that this was indication of cluster formation at fractional monolayer coverages. This shift in the temperature of the monolayer peak was also observed by Pache *et al.* [55], who agreed with the interpretation of Madey and Netzer [16]. The other desorption peak, which appears initially at 150 K, results from the adsorption of additional multilayers on top of the first wetting layer. This peak shifts to slightly higher temperatures as the coverage increases but its lower temperature leading edge remains constant, suggesting simple zero order kinetics. Another interesting feature of the desorption spectrum of water on Ni (111) is that the growth of the multilayer peak only commences upon the saturation of the monolayer peak. This suggests the formation of a complete wetting layer before the onset of multilayer adsorption.

Importantly, no desorption products other than water are observed and no desorption peaks are seen after all the water desorbs (at 170 K), even on annealing to room temperature. The absence of peaks typical of partial or total dissociation [65] on Ni (111) (figure 3.2) implies that water adsorbs and desorbs intact on
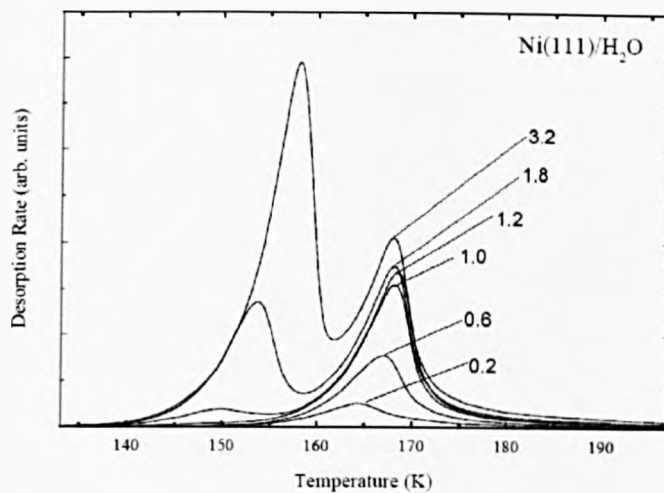
Figure 3.1: Thermal desorption of water from clean Ni (111) for initial coverages 0.2, 0.6 and 1.0 layers and the growth of a multilayer peak at higher coverage (1.2, 1.8 and 3.2 layers). Heating rate = 0.9 K/s.

this surface. Conversely, for other more reactive surfaces such as Pt (111) and Ru (0001) partially dissociated water structures consisting of OH / H_2O and O / H_2O , with characteristic desorption peaks at around 190 to 250 K, have been reported [65].
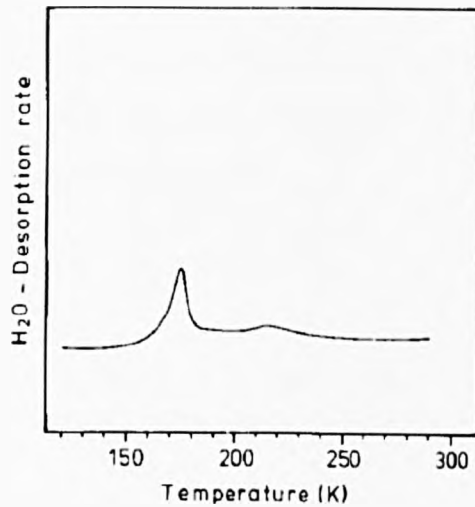
Figure 3.2: TPD profile from a dissociated H$_2$O layer on Ni (111), showing the distinctive high temperature peak (above 200 K) characteristic of dissociation. Adapted from Pache *et al.* [55].

3.3.2 Workfunction Measurements

Figure 3.3 shows the change in workfunction ($\Delta\phi$) as a function of ice thicknesses for amorphous solid water (ASW) films grown at 110 K on the Ni (111) (blue diamonds) and Pd (111) (red squares) surfaces. On Ni (111), the workfunction ($\Delta\phi$) changes rapidly for the first two layers, after which it only changes slowly before saturating at -0.94 V. This is similar to that previously reported for water adsorption on Ni (111) [13] and to that observed for Pt (111) ($\sim$-1 V) [49]. The Pd (111) surface shows similar behaviour, a rapid change in $\Delta\phi$ for the first two layers followed by a steady increase finally saturating at $\sim$-1 V. A monolayer of ice on Ni (111) produces a $\Delta\phi$ of -0.56 V in contrast to a $\Delta\phi$ of -0.70 V for the same film on the Pd (111) surface. Furthermore, growing crystalline ice films at warmer temperatures (153 K) on the Pd (111) produces the same $\Delta\phi$ of -0.70

V. Recently, Filhol *et al.* [66] calculated a $\Delta\phi$ of -0.2 V and -2.4 V for an ice bilayer (H-down and H-up respectively). Recent calculations by George Darling [67] obtained similar $\Delta\phi$ values for an H-up (-2.5 V) and H-down (- 0.3 V) bilayer. Thus, our experimental value for $\Delta\phi$ is inconsistent with both the H-up and H down versions of the conventional bilayer.
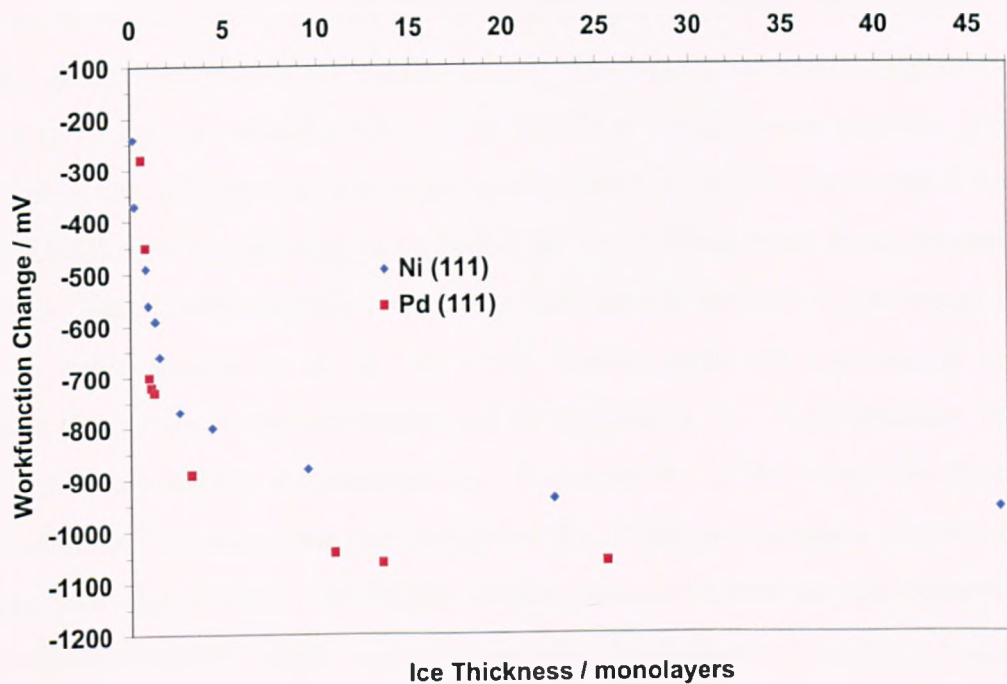
Figure 3.3: The change in workfunction as a function of ice thickness for ASW layers (dosed at 110 K) on Ni (111) (blue diamonds) and Pd (111) (red squares).

3.3.3 Low Energy Electron Diffraction

The first application of LEED to the H_2O / Ni (111) system was by Madey and Netzer in 1982 [16]. At first, they only observed an increase in the diffuse background scattering accompanied by dimming of the substrate spots for sub-monolayer coverages adsorbed at 80 K. However, upon the saturation of the first water layer, corresponding to the saturation of the peak at 170 K in the TPD trace, they reported a faint $(\sqrt{3} \times \sqrt{3})R30°$ LEED pattern. A subsequent study by Pache *et al.* [55] also reported an ephemeral $(\sqrt{3} \times \sqrt{3})R30°$ structure that was very short lived under the LEED beam. The undesired destruction or re-structuring of delicate adsorbate layers by LEED is a well-known problem [13]. To minimise the influence of the beam on our water films, we purchased a low current LEED system, allowing us to probe the water films using beam currents of ≤ 30 nA. This is substantially lower than that used in previous applications of LEED to water adsorption on Ni (111) [13]. Additionally, the exposure of the adsorbate film to the beam was minimised by optimising the LEED settings and then quickly moving the sample position. The stability of the water structures was investigated by monitoring the changes in the LEED patterns as a function of exposure time. Importantly, the LEED results presented below are also observed with a conventional VG LEED unit using significantly higher beam currents. The only notable difference between the two is that LEED patterns last tens-of-minutes longer when using the low current unit.

The LEED pattern for a clean Ni (111) surface is shown in figure 3.4. In contrast, the LEED pattern (25 eV) following the adsorption of a monolayer of water on Ni (111) is shown in figure 3.5. This pattern consists of an intense central ring of spots, surrounded by six bright spots in the commensurate half order positions, and is consistent with diffraction from two domains of a $2\sqrt{7}$ unit cell. These half order spots are in turn, surrounded by rings of lower intensity spots. A schematic representation of the LEED pattern formed by two domains

of the ice structure in a $2\sqrt{7}$ configuration is depicted in the lower frame of figure 3.5. The larger symbols in the schematic represent spots visible in the LEED at 25 eV . Annealing the surface causes the LEED pattern to fade and then completely disappear upon desorption of water at around 170 K.
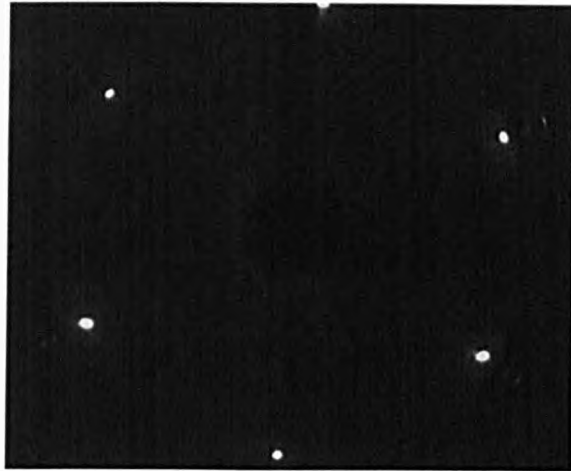
Figure 3.4: LEED pattern at 71 eV from a clean Ni(111) surface.

Previous LEED investigations of sub-monolayer water coverages on Ni (111) only reported an increase in the diffuse background scattering, together with concurrent dimming of the substrate spots and had argued that there was no significant ordering of water [16]. Conversely, we observe the $2\sqrt{7}$ LEED pattern for water coverages of between 0.67 and one layer, which implies the formation of islands of $2\sqrt{7}$ before the surface is saturated with a complete monolayer. Importantly, for ordered ice films less than a monolayer thick and grown at around 135 K, no diffraction intensity is observed around the Ni $\sqrt{3}$ positions. Interestingly, the $2\sqrt{7}$ LEED pattern disappeared for coverages just below 0.67 layers, which is in contrast to the behaviour observed for Pt (111), where an intense $(\sqrt{37} \times \sqrt{37})R25.3°$ LEED pattern is visible from as low as 0.15 of a monolayer and undergoes compression to a $(\sqrt{39} \times \sqrt{39})R16.1°$ structure as the coverage
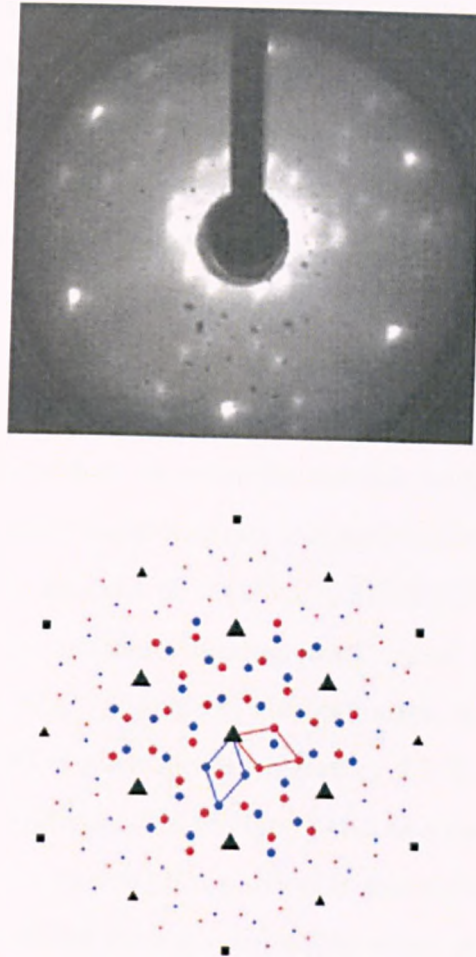
Figure 3.5: LEED pattern showing the $(2\sqrt{7}\times 2\sqrt{7})$R19° structure of H_2O on Ni (111) at 25 eV . Lower frame: schematic of the LEED pattern formed by two domains of a $2\sqrt{7}$ arrangement. The positions of the first order Ni spots (which are out of view at this energy) are indicated as solid squares. At energies above 20 eV the LEED pattern is dominated by the half order spots (shown as triangles) which are coincident between the $2\sqrt{7}$ domains. The two $2\sqrt{7}$ unit cells are indicated by different shading with spots that appear at 25 eV in the top panel shown as large symbols.

approaches saturation [50]. This indicates that on Ni (111), water does not prefer to form $2\sqrt{7}$ structures at very low coverages instead forming (smaller) less ordered structures [61]. Moreover, there is no direct evidence of any change in the lateral density of the water films for coverages of up to the saturation of the first layer. Conversely, on the Pt (111) surface, a change in lateral compression from -3.6% to 4.1% (with respect to bulk ice) is observed in the conversion of the initial $(\sqrt{37} \times \sqrt{37})R25.3°$ structure to the $(\sqrt{39} \times \sqrt{39})R16.1°$ configuration [47] [48].

The LEED results show that the bilayer model, previously proposed for water adsorption on Ni (111), does not apply to this system [59] [60]. Instead, water prefers to optimise its hydrogen-bonding network at the expense of optimising the O-metal bond. This means that, to maintain a stable hydrogen-bonding network on the Ni (111) surface, water must forgo its commensurate unit cell configuration. Indeed, this explains the absence of a $(\sqrt{3} \times \sqrt{3})R30°$ LEED pattern, both at low coverage and for the complete wetting layer. Due to the relatively short lattice parameter of the Ni (111) surface, the formation of commensurate $(\sqrt{3} \times \sqrt{3})R30°$ structures would require a compression of 4.5 % (as compared to bulk ice). This compression requirement is too large, and as a result, water is reluctant to adopt a honeycomb structure with a particular adsorption site on the surface.

In the absence of any direct evidence about the exact structure of the wetting layer on Ni (111), we assume that water adopts distorted hexagonal honeycomb network similar to those formed on the Pt (111) surface [50] [65]. In this regard, we propose a $(2\sqrt{7} \times 2\sqrt{7})R19°$ network of water molecules (figure 3.6) with a lateral compression of 2.8 % (relative to bulk ice). This compression is considerably less than the 4.5 % required for the $\sqrt{3}$ structure. Moreover, this arrangement produces an overall water coverage of 0.64 ML, which is very close to the 0.66 ML obtained by Pache *et al.* from XPS [55]. Just as for the $\sqrt{37}$ and $\sqrt{39}$ structures on Pt (111) [47], the $2\sqrt{7}$ wetting structure on Ni (111) implies a varying adsorption site for water molecules across the unit cell, as opposed to a defined adsorption site,

with domain boundaries relieving stress. Indeed, the $2\sqrt{7}$ unit cell has 18 different water molecules in its unit cell, giving rise to a range of different adsorption sites, with different geometries and vibration frequencies. This picture of the first water layer on Ni (111) is consistent with the very broad H^+ distribution observed in the ESDIAD [16], since the water molecules have a range of different orientations, probably majority flat or H-down, which will all contribute to the H^+ peak.

Similarly, the $2\sqrt{7}$ structure is in agreement with the UPS results of Nobl and Benndorf [57], which suggest a disordered structure, but inconsistent with the $\sqrt{3}$ bilayer inferred by Pache *et al.* [55].
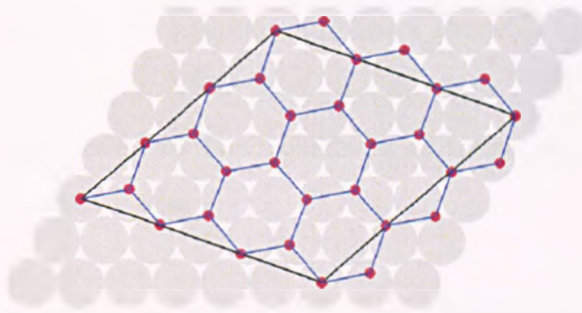
Figure 3.6: Schematic of the $2\sqrt{7}$ unit cell, showing one possible arrangement of water in an ice like, hexagonal hydrogen bonded network. The oxygen of each water (solid dots) sits at the corners of the hexagons, with one hydrogen atom sitting along each vertex and the others above or below the layer.

The long-range registry of the $(2\sqrt{7} \times 2\sqrt{7})R19°$ structure and the formation of extended, ordered islands below saturation coverage, is analogous to the formation of ordered structures on Pt (111) [47][50] [65]. On that surface, STM shows domains of a hexagonal ice structure [46], whereas no STM data is currently

available for water adsorption on Ni (111). In addition, whereas the $\sqrt{37}$ wetting structure on Pt (111) compresses to a $\sqrt{39}$ structure to allow more water on the surface at saturation [47][48], the $2\sqrt{7}$ LEED pattern on Ni (111) does not change with coverage as the monolayer grows and saturates.

The ability of water to adopt a range of adsorption sites is crucial in the wetting of the Pt (111) [50] surface and thus, may play a similar role on Ni (111). Compared to the structures formed on Pt (111), the $2\sqrt{7}$ LEED pattern on Ni (111) always shows rather more background intensity. This implies that there is rather more disorder in the wetting layer formed on Ni (111) and that the formation of a well-defined $2\sqrt{7}$ periodicity is only slightly favoured over a disordered, or incommensurate ice structure. Indeed, the adsorption of a second water layer on top of the wetting layer destroys the $2\sqrt{7}$ LEED pattern, leaving a hexagonal pattern with a diffuse background. This indicates that the wetting layer structure is disrupted by the formation of hydrogen bonds to the second layer, producing a bulk ice film.

3.3.4   Electron Beam Damage and Dissociation

We observe that, given sufficient exposure, ice layers on Ni (111) undergo electron induced restructuring, even when operating with beam currents of below 30 nA. The LEED pattern shown in figure 3.7 is recorded at 55 eV , after extended exposure of the ice film to the LEED beam. The $2\sqrt{7}$ structure observed for an intact layer has disappeared, replaced by multiple spots and an increase in the intensity around the $\sqrt{3}$ positions. There is also an intense 2 × 2 pattern, which persists, even with the desorption of water at 170 K. Moreover, no desorption was registered by the QMS as the film dissociated, suggesting that the ice film restructures under the influence of the electron beam without any electron induced desorption. Heating the beam damaged film results in the disappearance of the intensity in the $\sqrt{3}$ positions. On the other hand, the intensity in the 2 × 2

positions persists up to ~250 K, considerably higher than that associated with the pure water phase, which disappears after the desorption of water at ~170 K.
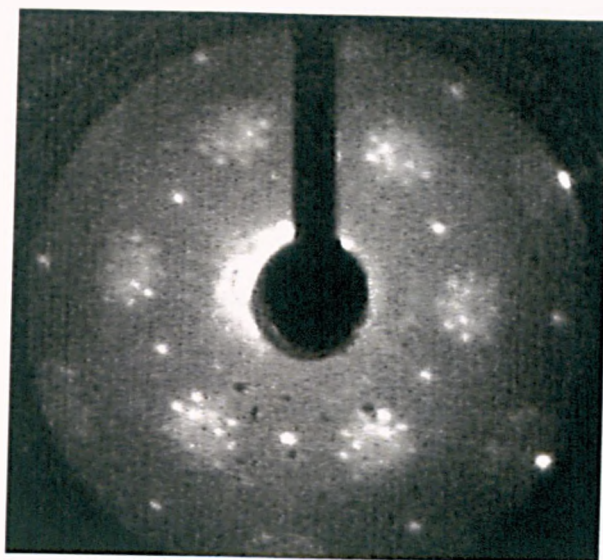
Figure 3.7: LEED pattern of a water layer on Ni (111) after extended electron exposure (taken at 55 eV), showing the development of spots and intensity near the $\sqrt{3}$ and (2×2) positions. Two of the Ni spots are just visible to the right-hand side of the screen.

This (2×2) pattern is most likely due to the creation of partially dissociated OH/H_2O or O/H_2O structures, where the oxygen in these structures pins the water film in registry with the Ni (111) surface. This picture is consistent with the fact that, above 180 K the half order spots were only present in areas of the film that received deliberate doses of high beam currents, whereas other patches remained unaffected. Pache *et al.* [55], who observed a 2×2 pattern as well, also concluded that it was probably due to the formation of partially dissociated structures.

Similarly, Mundt and Benndorf [60] initially observed a weak $\sqrt{3}$ pattern for a water layer adsorbed on the stepped Ni (11, 11, 9) surface at 120 K but observed that heating the film to 150 K reduced the $\sqrt{3}$ structure to a 2 × 2 LEED pattern. This 2 × 2 pattern displayed the highest intensity at 160 K before disappearing altogether at 250 K. Although, these authors subsequently attributed (2×2) phase to a temperature and coverage induced reordering of the surface, they did not rule out the possibility that dissociation may have already occurred at 165 K [60]. They cautiously suggested that some desorption may have occurred at 165 K and that the consequent reduction in the coverage may facilitate the compression of the $\sqrt{3}$ structure, enabling it to expand out of registry with the Ni (111) and form a (2×2) unit cell [60].

A recent synchrotron x-ray diffraction study by Nakamura and Ito [68] for water and oxygen coadsorption on Ni (111) also found a 2 × 2 structure. In addition, these authors used Fourier difference analysis to measure the position of O atoms, for water molecules adsorbed on the (2×2) O surface at 25 and 140 K. They found that, at low temperatures, water adsorbed in a disordered threefold arrangement around the chemisorbed O atoms. In this configuration, the O atom of the water molecule sits above the three-fold hollow site, while one D atom hydrogen bonds to the chemisorbed O and the other D atom dangles up from the surface. This arrangement is consistent with the strong H^+ ESDIAD emission peak reported for the coadsorption of water with oxygen at low temperatures [16]. As the surface temperature increased to 140 K, this adsorption site became unstable, with water subsequently preferring to adopt a flat geometry atop the Ni atoms. In the RAIR spectrum [68], the OD stretching bands disappeared as the surface temperature was increased, leaving just a single sharp band at 1165 cm^{-1}, which they assigned to the bending mode of a flat lying water monomer that gains intensity by vibronic coupling to the Ni surface. Further heating of the surface to 200 K led to the appearance of a new band at 2681 cm^{-1}, in addition to the

original water bending band. This new stretching band was assigned to partial dissociation of water to form OD [68] [69]. Interestingly, the surface retained its ((2×2)) periodicity irrespective of the water coverage, which indicates that the chemisorbed O was largely unperturbed by water adsorption.

3.3.5 Multilayer Growth

Having observed that the initial wetting layer on Ni (111) is not the previously assumed commensurate $(\sqrt{3} \times \sqrt{3})$R30° bilayer, we then investigated the wetting behaviour of thicker ice films. We find that adsorbing a fraction of a layer of water on top of the wetting layer completely restructures the $2\sqrt{7}$ layer, producing a diffuse LEED pattern with faint spots appearing in a rotated hexagonal pattern that is centred around the (0 0) beam. Depositing further water leads to an incommensurate hexagonal LEED pattern with spots near the $\sqrt{3}$ positions (figure 3.8). This pattern first appears as the coverage reaches 2 ML and gains intensity as the coverage increases, persisting as a multilayer ice film forms. Heating a multilayer ice film (2-10 layers) causes the $2\sqrt{7}$ LEED structure to reappear as the coverage drops from 2 ML to 1 ML and the multilayer sublimes. This behaviour is consistent with restructuring of the $2\sqrt{7}$ monolayer into an incommensurate multilayer upon the adsorption of, at minimum, two layers of water. This incommensurate film is oriented to the Ni close packed rows, which suggests that the first layer adopts some preferred registry to the surface.

We also investigated the wetting of the $(2\sqrt{7} \times 2\sqrt{7})$R19° monolayer by multilayer ice using chloroform adsorption-desorption measurements. The TPD trace of chloroform from ice layers adsorbed on close packed metal surfaces shows discrete behaviour for desorption from the bare metal, the first wetting layer and from multilayer ice films and thus can be exploited to obtain information about the morphology of the ice layers [70]. For instance, Zimbitas *et al.* have previously shown that for multilayer ice films on the Pt (111) surface, the chloroform desorp-
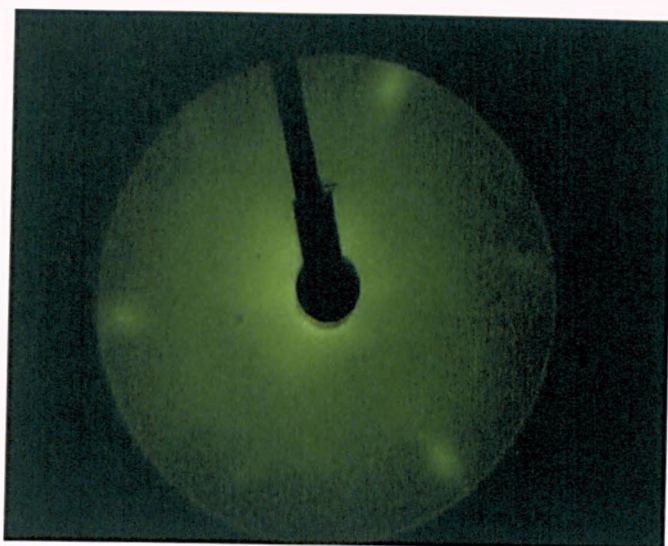
Figure 3.8: Hexagonal LEED pattern(21 eV) with spots near the $\sqrt{3}$ positions, after the adsorption of 2 layers of H_2O on Ni (111)

tion temperature depends on the chloroform's initial adsorption site. In our study, chloroform is dosed directly on the surface at $\leq$ 100 K, using an effusive molecular beam. For a clean Ni (111) surface, the desorption spectrum of chloroform shows two peaks (figure 3.9). The first peak appears at 150 K and is due to desorption of the $CHCl_3$ monolayer directly adsorbed on the metal surface. With the saturation of this peak, a second peak develops at ~130 K. This lower temperature peak arises from the desorption of chloroform multilayers. Chloroform measurements for multilayer ice on Ni (111), are performed by depositing ice layers of various thicknesses on the Ni (111) surface at 135 K, after which the sample is rapidly cooled to below 100 K. A sub-monolayer dose of chloroform is then adsorbed on top and the chloroform desorption temperature monitored as the surface is annealed. This subsequently provides information about the adsorption site of the chloroform at the surface and hence the morphology of the ice film.

The TPD profiles of chloroform from ice films of various thicknesses (0.7 -10 layers) on Ni (111) are shown in figure 3.10. Chloroform (dashed line) desorption
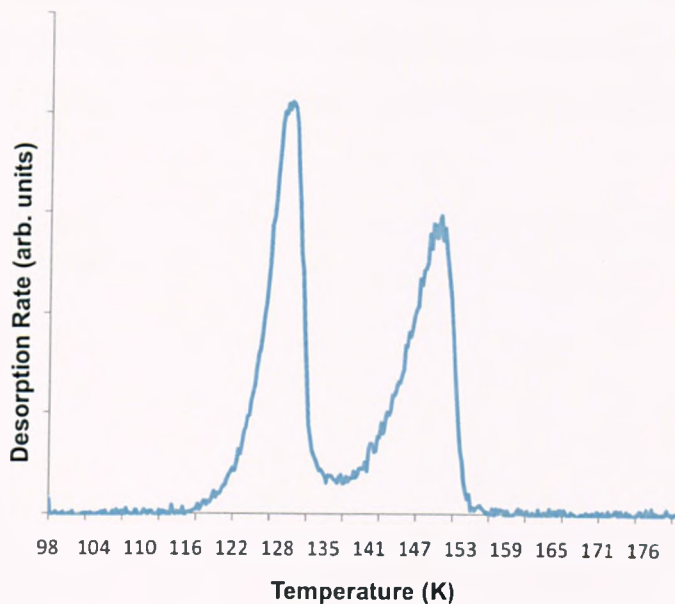
Figure 3.9: The TPD profile for ~2 layers of CHCl$_3$ from a clean Ni(111) surface.

from the first layer of water gives peaks at 138 K and 155 K, consistent with the behaviour observed on the Pt (111) and Ru (0001) surfaces. Monitoring the peak at 155 K as it diminishes with increasing ice thickness gives a measure of the amount of ice monolayer remaining exposed as the ice multilayer grows. The 155 K peak undergoes significant attenuation after the adsorption of 1.5 layers and disappears completely for water coverages above two layers. For thicker ice layers, a (single) chloroform desorption peak appears at 136 K. The chloroform desorption experiments imply that a uniform second layer of water forms on top of the initial wetting layer. Moreover, this layer is almost continuous when an average coverage of 2 layers has been adsorbed. This layer-by-layer growth of ordered crystalline ice on Ni (111) is in sharp contrast to multilayer growth on the Pt (111) surface, where a water multilayer of 40-100 layers is required before the ice forms a continuous film that completely covers the first wetting layer [70] [71].

On the other hand, the completion of a second layer on Ni (111) is consistent with changes to the LEED pattern, which indicate that an incommensurate film forms at a coverage of just 2 layers and persists with the growth of thick ice multilayers.
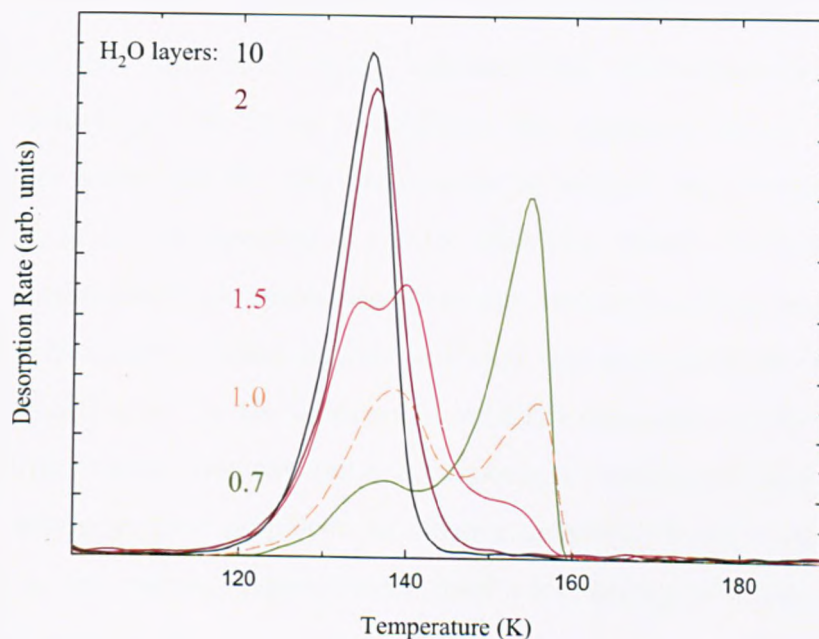
Figure 3.10: The TPD spectrum for a fixed coverage of $CHCl_3$ ($\sim$0.8 sat) from various coverages of H_2O on Ni(111).

Since the wetting layer on Ni (111) is not pinned into registry with the metal surface, it is not forced to adopt a particular adsorption site but enjoys a certain degree of flexibility, allowing it to form epitaxial layers with the first layer of water matching its lattice to the metal surface. All of this implies that on Ni (111), there is little difference in the free energy of the incommensurate interface layer, which forms between the bulk ice film and the Ni surface and that of the $2\sqrt{7}$ monolayer, where the water structure is optimised to the Ni substrate.

Recent studies of water adsorption on Ni (111) by Souda, report the slow

"dewetting" of an initially uniform water film at temperatures above 135 K [72]. In contrast, we do not find any dewetting of the metal surface for temperatures below 135 K, although we do not rule out dewetting at higher temperatures. A subsequent study by the same author [73], using temperature programmed time of flight secondary ion mass spectrometry (TP-TOF-SIMS) after 1.5 k eV He$^+$ sputtering of ASW films on Ni (111), indicated that no hydrogen-bonded water network is formed at 100-120 K. In addition, they observed abrupt "dewetting" of the surface above 160 K (the temperature at which a water monolayer desorbs from Ni (111)), irrespective of the ice thickness. Souda concluded that the strongly chemisorbed water molecules of the first wetting layer are unable to form an extended hydrogen-bonded network and that this contributes to the stabilisation of the multilayer. On the contrary, our LEED data indicate the presence of an ordered monolayer that can relax in response to multilayer adsorption. Importantly, where we have employed an effusive molecular beam to deposit water accurately on the sample surface, Souda used a less accurate background dosing technique. Moreover, Souda quoted a chamber base pressure of 1×10^{-8} Torr for the sputtering experiments, which is relatively high. We know that even minor impurities can have a substantial effect on the lateral order of the wetting layer and its ability to relax and change density. Thus, one possibility is that the experimental conditions in Souda's [73] study may have enabled impurities such as oxygen on the surface, leading to O/H_2O co-adsorption, with the oxygen helping to pin the wetting layer to the Ni surface.

3.4 Conclusions

Water adsorbs on Ni (111) to form a hydrogen bonded wetting layer with a $(2\sqrt{7} \times 2\sqrt{7})R19°$ unit cell, in contrast to previous reports of a commensurate $(\sqrt{3} \times \sqrt{3})R30°$ structure for this surface. The LEED and TPD results indicate

that water prefers to extend its hydrogen-bonding network by forming extended islands of order ice rather than adopting a particular adsorption site on the metal surface and forming small commensurate clusters. The relatively short lattice parameter of Ni (111) means that the 4.5 % compression (as compared to bulk ice) required for a commensurate $\sqrt{3}$ structure is simply too great. Instead, adsorption proceeds via the formation of sub monolayer islands of $2\sqrt{7}$ before the surface is saturated with a complete wetting layer with no change in the lateral period of the wetting layer as sub-monolayer islands grow to completely cover the metal surface. Subsequent adsorption of even a small amount of water on top of the wetting layer restructures it to form an incommensurate R30° structure oriented to the Ni close packed rows. This is similar to the behaviour seen on other surfaces such Pt (111) [65], except that on Ni (111), the wetting layer appears to be more labile, enabling it to adopt an incommensurate registry with the metal surface as soon as a second layer adsorbs on top. In addition, we find that the $2\sqrt{7}$ water structure is quickly damaged by exposure to the LEED beam, leading to the appearance of additional spots near the $\sqrt{3}$ positions. Further electron exposure produces an intense (2×2) pattern, which only disappears at temperatures above 200 K. This behaviour is similar to that previously observed by Mundt and Benndorf [60] and indicates the formation of an electron induced dissociation structure (O/H_2O or OH/H_2O) with a (2×2) registry.

Chapter 4

Adsorption and Wetting of the Ru (0001) Surface

4.1 Introduction

The Ru (0001) surface has generally been the surface of choice for the study of water adsorption on close packed metal surfaces. As far back as 1981, Thiel *et al.* [10] had reported the appearance of a $(\sqrt{3} \times \sqrt{3})R30°$ LEED pattern after the adsorption of a layer of H_2O at 95 K and some higher temperatures. A year later, Doering and Madey published their seminal ESDIAD, LEED, TDS, EELS and IR study [59], in which they reported that water adsorbs on the Ru (0001) surface by forming epitaxial 2D bilayers. These authors subsequently proposed their 'classic' bilayer model, based on a water adlayer that conforms to the Bernal-Fowler-Pauling (BFP) ice rules [11] [12] together with their own surface modification rules [59]. The resulting configuration is a puckered bilayer, similar to the (0001) plane of hexagonal ice, where the water molecules are arranged in a hexagonal, honeycombed network. The term 'bilayer' refers to the fact that half the water molecules in the hydrogen-bonding network adsorb on the Ru surface via their O atoms while the other half form hydrogen bonds to this lower layer without having

any direct contact with the Ru surface. In addition, each water molecule in the lower half of this bilayer has three hydrogen bonds, while each water molecule in the upper layer is left with an unsatisfied hydrogen bond. This 'dangling' H atom has traditionally been assumed to be directed towards the vacuum [1], although a more recent modification of the traditional model has the unsatisfied hydrogen bonds facing the substrate surface ('H-down' bilayer)[74].

For more than a decade, the bilayer model remained the only picture of the wetting layer on Ru (0001) as well as becoming the basis for studying adsorption on a range of other surfaces [1][13]. However, it began to receive scrutiny following the publication of the first complete LEED I-V analysis of the water/Ru (0001) system in 1994 [3]. In this study, Held and Menzel performed a detailed analysis of the D_2O structure on Ru (0001) based on LEED IV simulations of two O atoms in a $(\sqrt{3} \times \sqrt{3})R30°$ unit cell. The subsequent best-fit geometry indicated the formation of a hexagonal water layer on top of the first layer of Ru atoms. While this finding is in agreement with previous studies [1], the LEED I-V analysis also found that the O atoms in the two halves of the bilayer are almost co-planar $(\Delta z_{(O-O)} = 0.10 \pm 0.02$ Å), with the first Ru layer buckled in anti-correlation to the O height. This is surprising since the bilayer structure was based on a 2D plane of hexagonal ice and so the vertical displacement between adjacent O atoms had traditionally been anticipated to be about 0.96 Å [1]. In agreement with previous studies, Held and Menzel concluded that half the water molecules of the bilayer do indeed form a chemical bond with the Ru surface while the water molecules in the upper half are hydrogen-bonded to the lower layer with their uncoordinated H atoms pointing (H-up) toward the vacuum. In contrast to the conventional bilayer, this structure is considerably flattened. Nevertheless, these authors could not to repudiate the conventional model entirely. Indeed important aspects of it, like the existence of two distinct types of water molecule within the unit mesh, which differ in their bonding environments remained valid. To date,

Held and Menzel's study remains the only detailed structural analysis of a wetting layer on a metal surface.

Interest in water adsorption on the Ru (0001) surface was reignited in 2002 after Feibelman published *ab initio* DFT calculations for a D_2O wetting layer [19]. In this study, this author initially calculated the binding energies of intact wetting layers but found that these consistently produced binding energies that were 0.15 to 0.2 eV below the heat of sublimation of ice. Thus, from a thermodynamic perspective, water would not even be expected to wet the Ru (0001) surface, instead preferring to form 3D clusters. In the conventional bilayer model it had been thought that the O atoms of the lower water molecules bind to the Ru surface through the mixing of the P_z orbitals (where z is normal to the surface) with the Ru valence states while the upper water molecules have no direct interaction with the metal surface. However, since Held and Menzel [3] had found an almost coplanar wetting layer, Feibelman argued that this co-planarity implies that all of the O atoms in the wetting layer must interact with the surface in a similar manner, which means the upper water molecules must somehow move closer to the metal surface. Feibelman proposed that this could be achieved by severing the non-hydrogen bonding D atom of the upper lying water molecules. Furthermore, he argued that the severed D atoms would not desorb but remain on the surface as D (ads), most likely on bare patches of Ru or in the centre of the D_2O -OD hexagons.

The resulting configuration is a partially dissociated $D/OD/D_2O$ wetting structure that is thermodynamically favourable relative to the conventional bilayer. The O atoms of the upper and lower water molecules in this dissociated monolayer are (respectively) 2.16 and 2.09 Å above the metal surface, consistent with the nearly coplanar wetting layer implied by the LEED IV simulations. In addition, the presence of the dissociated D atoms would not be detected by LEED I-V analysis, as it does not affect the co planarity of the adsorbed D_2O -OD structure.

In response to Feibelman's DFT calculations, Puisto *et al.* [20] performed a refined analysis of the original LEED I-V simulations, together with a full analysis of Feibelman's partially dissociated structure. The best-fit geometry from the refined analysis suggested an intact wetting layer with out of plane hydrogen atoms atop the slightly higher oxygen atoms, in effect, a refined version of the earlier model proposed by Held and Menzel [3]. While Puisto *et al.* concluded that the partially dissociated structure is probably not responsible for the ($\sqrt{3} \times \sqrt{3}$)R30° layer observed by LEED, the Pendry Factor (R$_P$) difference between an intact and a partially dissociated structure was within the acceptable error range of 19 % and so they could not exclude (unequivocally) the partially dissociated wetting layer model.

This controversy over the structure of the wetting layer on the Ru (0001) surface stimulated a number of subsequent studies [4, 23, 26, 30–32], all of which show that the water/Ru system is far more complicated than originally anticipated. For instance, core-level XPS studies by Weissenrieder *et al.* [31] indicated that the wetting layer contained OH and H_2O in a 3:5 ratio, in good agreement with Feibelman's partially dissociated wetting layer but at variance with the fact that LEED consistently suggests the presence of an ordered ($\sqrt{3} \times \sqrt{3}$)R30° structure. In contrast, Clay *et al.* [23] and Andersson *et al.* [30] found that water may form intact or dissociated structures, depending on the isotope and the adsorption conditions. At temperatures below 150 K, water wets the Ru (0001) surface, forming a metastable intact overlayer. However, this structure exhibits a significant kinetic isotope effect whereby a D_2O monolayer desorbs intact upon heating but an H_2O monolayer decomposes to form a partially dissociated structure that is stable up to 210 K [23].

In this chapter, we investigate the nature of the intact ($\sqrt{3} \times \sqrt{3}$)R30° phase on Ru (0001) using a combination of LEED I-V and Helium Atom Scattering (HAS). By combining LEED with HAS, we can examine whether or not helium

scattering can confirm the $(\sqrt{3} \times \sqrt{3})R30°$ ordering of the O and Ru atoms implied in previous LEED studies of this system [13]. In addition, we discuss possible structures for the wetting layer, based on recent DFT calculations of the intact 2/3 ML water layer [4], which find that water forms chains of flat-lying and H-down water molecules within a honeycomb hydrogen bonded network. This novel structure does not have the simple alternation in O height that characterises the traditional water bilayer and is intrinsically disordered, with no long-range registry between the heights of the O atoms or the location of the protons. Finally, we examine whether structures based on this model are consistent with the well-ordered $(\sqrt{3} \times \sqrt{3})R30°$ pattern observed in LEED.

4.2 Experimental

The LEED I-V measurements are performed in a stainless steel ultra high vacuum chamber (chamber 1, see chapter 1) with base pressures of below 3×10^{-10} Torr. The chamber is equipped with a dual microchannel channel plate (MCP) LEED unit and a quadrupole mass spectrometer (QMS) for TPD measurements. The Ru (0001) sample is mounted by welding a pair of tantalum heating wires to either side of the crystal and then spot welding these wires to two liquid nitrogen-cooled support rods, which are connected to a Dewar-type manipulator. The sample temperature is measured via a K type thermocouple welded to the back of the crystal. The crystal can be rapidly cooled to 96 K by filling a cylinder inside the manipulator with liquid nitrogen and heated to 1500 K using a direct current from an external power supply. The Ru crystal is aligned to $\pm$ 0.25° of the (0001) face and cleaned by repeated Ar^+ sputter and high temperature anneal cycles ($\geq$1000 K). The purity of the surface is confirmed by the LEED images of an ice monolayer and from the thermal desorption behaviour.

D_2O (purity: 99.99 %) is dosed using a specially constructed two-stage molec-

ular beam, which allows the high purity D_2O to be transferred directly on to the face of the Ru (0001) crystal without contamination. Relative surface coverages are obtained using the well documented King and Wells [52] direct reflection technique, while integration of the area under the desorption peak(s) provides a secondary measure of relative coverage. Absolute coverages are obtained by calibration against the coverage required to produce pin sharp $(\sqrt{3} \times \sqrt{3})$R30° spots, which is taken as 2/3 ML. Desorption is monitored using a QMS in direct sight of the sample. LEED patterns are recorded using an OCI low current LEED unit equipped with a computer controlled video system. Sharp $(\sqrt{3} \times \sqrt{3})$R30° LEED structures are consistently obtained by either of two methods. The first involves saturating the surface at low temperatures (below 100 K) followed by slow annealing of the sample until the complete desorption of the multilayer. Alternatively, equally sharp $(\sqrt{3} \times \sqrt{3})$R30° spots are obtained by depositing an absolute coverage of 0.67 ML at 138 K, although this method is admittedly more trying.

LEED I-V curves for an energy range of 40-400 eV are recorded for the $(\sqrt{3} \times \sqrt{3})$R30° phase on Ru (0001) in steps of 1 eV . Sustained exposure to the electron beam during LEED measurements can lead to significant restructuring of water films. To ensure against this, the beam current is kept below 40 nA at all times using small increments in the Wehnelt potential, in proportion to the beam energy. These conditions allow us to maintain stable ice structures for the duration of our experiments. A typical scan of 40 to 400 eV can be recorded in less than 10 minutes, which corresponds an estimated electron dose of 0.14 electrons per atom. A combination of LEED and post exposure TPD is used as an indication of electron beam damage. The presence of partial dissociation is revealed by a characteristic desorption peak about 33 K higher than the intact monolayer peak.

4.2.1 Helium Atom Scattering

The Helium scattering experiments are conducted in a stainless steel ultra high vacuum (UHV) chamber (chamber 2, see chapter 1) with base pressures better than 5×10^{-11} Torr. This chamber is comprised of seven independently pumped sections, with the first section housing the He beam source. The circular Ru(0001) crystal is mounted by spot welding a tantalum wire on either edge. These two wires are then welded to a pair of tantalum support rods that are in turn mounted on a liquid nitrogen cooled manipulator via barrel connectors. The crystal surface is cleaned between experiments using repeated cycles of argon ion sputtering followed by high temperature annealing ($\geq$850 °C).

High purity helium (BOC) is supplied to a specially designed nozzle at a stable pressure of up to 10 bar, after passing through a nitrogen cooled coil to remove any remaining condensable impurities. The nozzle assembly is housed in a liquid nitrogen Dewar, which, together with resistive heating of the tip using a direct current, allows the nozzle to be cooled to 110 K and heated to ca. 380 K. This temperature range corresponds to beam energies of 26-80 meV , as confirmed by time-of-flight (TOF) measurements using a retractable chopper. The nozzle temperature is measured using a K-type thermocouple spot welded to the tip and is stable to within $\pm$ 0.1 K.

The sample is mounted on a VG (x,y,z) manipulator whose axis can also be tilted relative to the scattering plane. The crystal is positioned so that it is at the centre of the azimuthal rotation of the manipulator (θ), with the surface perpendicular to the incident beam. Thus, upon entering the main chamber, the He beam is incident at the centre of the crystal. During the scattering measurements, the incident and reflected beam paths are always fixed at 90° to one another and the crystal is rotated about θ by a computer controlled stepper motor. The reflected beam exits the experimental chamber through a 3 mm aperture, passing through a differentially pumped stage before entering the final section containing the de-

tector (a Hiden HAL 301 X beam QMS). For further reduction of background gas, an ion pump is used to pump this final compartment independently. The scattering measurements presented in this chapter are acquired by blocking off the final 3 mm aperture and using the QMS as a stagnation detector. In stagnation mode the clean Ru (0001) surface gives a maximum reflected intensity of around 1.5×10^6 cps in the specular beam. The HAS measurements are recorded at 300 K, which corresponds to an energy of E = 65 meV , an incident wavevector of $k_i = 11.1$ Å^{-1} and an energy resolution of Δ E/E of 7.0%. In addition to the HAS apparatus, the main chamber is equipped with a low current, dual microchannel plate (MCP) LEED system. The azimuthal orientation of the sample is initially set using LEED and then optimised using helium diffraction from a (2 × 2) O film.

To highlight the critical role of the preparation on the resultant ice structure, the water layers are grown using two separate experimental arrangements. The first method involves dosing with a molecular beam with a typical flux of 0.005 layers s^{-1}, which causes the chamber pressure to rise to about 2×10^{-11} Torr during adsorption. The exposure of the surface to the molecular beam is controlled to a high accuracy using a retractable flag positioned in front of crystal. The coverage of the D_2O layers is obtained by measuring the uptake required to form a saturated ice monolayer at the surface, using the King and Wells direct reflection technique [52]. A second measure of the D_2O coverage is provided by TPD measurements, calibrated against a saturated monolayer (defined here as 1 layer of water). In contrast, the susceptibility of H_2O layers to dissociation during heating made accurate measurement of the H_2O coverage more difficult. The saturation coverage for a monolayer of H_2O is typically determined from the exposure time required to produce a saturated monolayer peak (i.e. just before the onset of the multilayer peak) in the TPD spectra. The TPD spectra for water layers dosed via the molecular beam are obtained using an unshielded VG Smart-IQ QMS that is

housed in the main experimental chamber and positioned very close to the front face of the crystal.

The second dosing method employed in our experiments is background dosing via a collimated tube, supplied by a variable leak valve. However, unlike the molecular beam technique, this method leads to unwanted additional adsorption on the edges and sides of the crystal as well as on the support posts and heating wires. To obtain TPD spectra characteristic of desorption from the surface alone, the QMS detector is used in the previously mentioned stagnation configuration. In this arrangement, the QMS is housed inside a retractable gas collection tube with a 4 mm orifice. During TPD measurements, the collection tube is positioned directly in front of the sample, allowing gas desorbing from the surface to enter the detector housing via the 4 mm aperture while excluding gas desorbing from the sample surroundings. In general, we find that the TPD spectra obtained via background dosing are consistent with those from beam-dosed layers. However, TPD spectra from background dosing has an additional time constant due to pump out of the detector volume. This time constant is modelled and the tail subsequently removed from the TPD spectrum, allowing direct comparison with the TPD spectra from beam-dosed layers.

4.3   Results and Discussion

4.3.1   Preparation of Intact H_2O and D_2O Layers

The TPD profile of an intact D_2O layer (figure 4.1, dashed black line) is a simple two peak profile. The wetting layer in direct contact with the Ru surface appears as a high temperature peak near 180 K while the onset of multilayer desorption begins at ~142 K before maximising at ~160 K. In addition, dissociation of the wetting layer due to contamination during adsorption, or electron beam damage during LEED measurements, stabilises water on the surface. This gives rise to a

further desorption peak at around 200 K. After any scattering measurement the absence of this higher temperature peak (or tail) is, in general, a good indication of a contamination free and intact ice film. With the use of a low current MCP LEED unit, we find it relatively simple to avoid electron damage of the ice films and as anticipated, the helium measurements have no discernable effect on the TPD.

As mentioned previously, the TPD profile for ice layers grown using a molecular beam and those grown via the background dosing method were generally very similar (figure 4.2). However, a point worthy of note is that the area in the TPD spectrum around 200 K was only completely featureless for beam dosed ice layers, indicating that some dissociation occurs during background adsorption. The molecular beam deposits a water beam directly on the crystal surface, causing an insignificant pressure increase in the main chamber. In contrast, with background dosing the chamber pressure rises to ca. 6×10^{-10} Torr, only recovering to base level after 5-10 minutes and so the surface is prone to contamination by gases displaced from the chamber walls. We find that this pressure increase in the main chamber can be reduced by cooling the titanium sublimation pump to 80 K. This in turn reduces the desorption intensity around 200 K, giving credence to the interpretation of this feature as a by-product of the coadsorption of some low coverage surface impurity. Similarly, we find it impossible to obtain an intact $\sqrt{3}$ LEED pattern using the background dosing method. Instead, we always obtain the streaked LEED pattern normally attributed to domains of partially dissociated $OH/H_2O/H$ [23]. Conversely, good $(\sqrt{3} \times \sqrt{3})R30°$ LEED patterns are relatively simple to obtain for H_2O layers dosed using an effusive molecular beam. The implication is that there is always an element of contamination associated with background dosing. However, while this contamination always leads to dissociation in H_2O layers, there is a strong kinetic isotope effect in dissociation [23] and so the impact on the TPD spectra and LEED patterns of D_2O layers
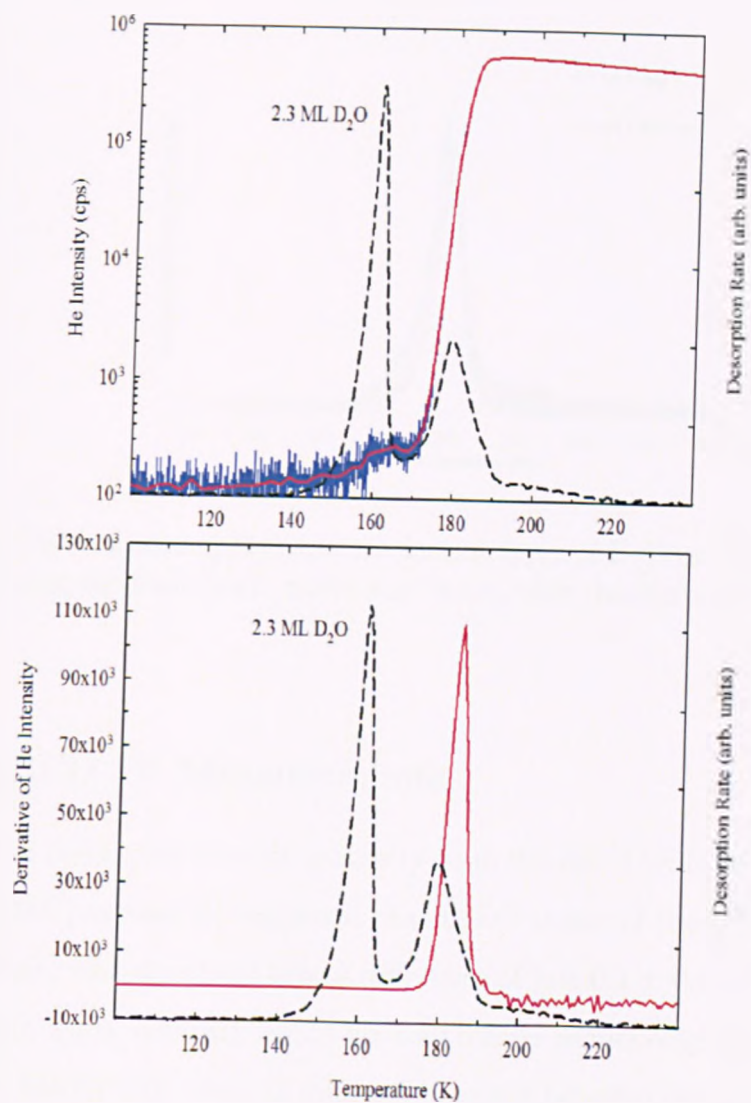
Figure 4.1: Top: The He specular reflectivity (blue:raw and red:smoothed) and D_2O TPD (dashed black line) as a function of the surface temperature(ramp rate ~0.5 K/s, He beam energy = 65 meV). Bottom: the red line corresponds to the derivative of the He reflectivity signal shown in top panel as a function of temperature.

is less perceptible. Moreover, dissociation of the water layer also has significant implications for helium scattering, which are discussed later.
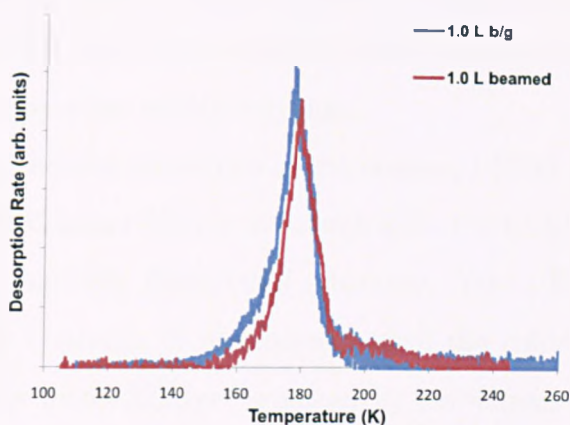
Figure 4.2: Thermal desorption spectra for one layer of D_2O on Ru (0001) for two different dosing methods (red: molecular beam, blue: background dosing).

4.3.2 LEED IV Measurements

As mentioned before, the best-fit geometry from the first LEED IV analysis of the water/Ru (0001) system [3] suggested that the O atoms of the $\sqrt{3}$ bilayer are almost co-planar, with a vertical height difference of just 0.1 ± 0.02 Å (compared to ~ 1 Å in ice I). Thus, contrary to the buckled bilayer model originally proposed by Doering and Madey [59], there is minimal buckling between the two halves of the bilayer. In response to these LEED IV simulations, Feibelman compared the binding energy of intact water bilayers and partially dissociated $OH/H/H_2O$ structures using density functional theory [19]. His calculations implied that the binding energies of intact $(\sqrt{3} \times \sqrt{3})R30°$ bilayer structures are significantly lower than the sublimation energy of bulk ice and thus cannot wet the Ru (0001) surface. Moreover, in contrast to the near co-planarity of the wetting found by Held and Menzel

from LEED IV, Feibelman found substantial corrugation in the O atoms of intact H-up or H-down bilayers (0.72 and 0.52 Å respectively) [19]. On the other hand, the binding energy calculations for a partially dissociated $OH/H/H_2O$ structure implied that it would wet the Ru (0001) surface. In addition, since this structure has a corrugation of just 0.05 Å it is consistent with the observation that the O atoms of the wetting layer are nearly coplanar.

Despite this, a subsequent reanalysis of the original LEED IV simulations [20] still favoured a flattened intact bilayer, although from the LEED IV fits it was not possible to exclude a partially dissociated structure. Yet, a flat (intact) bilayer, with almost coplanar O atoms, is inconsistent with the substantial corrugation in the O atoms of the intact bilayer, reported by Feibelman [19] and in subsequent calculations by Michaelides *et al.* [22], Haq *et al.* [4], Meng *et al.* [24] and Materzanini *et al.* [21]. What then may explain this inconsistency? Since the $(\sqrt{3} \times \sqrt{3})R30°$ structure on Ru (0001) is exceptionally susceptible to electron beam irradiation, one possibility is that it may have suffered inadvertent electron damage during the LEED IV measurements, leading to the formation of a dissociated (and thus coplanar) $D/OD/D_2O$ structure.

To investigate electron beam damage and dissociation of the wetting layer on Ru (0001), we have re-measured the LEED IV data for the intact D_2O $(\sqrt{3} \times \sqrt{3})R30°$ structure, originally studied by Held and Menzel [3], using an MCP low current LEED system. Figure 4.3 shows the LEED IV profiles for a monolayer of D_2O , obtained after a 40-400 eV scan. Overall, the IV curves compare well with those of Held and Menzel (figure 4.4) [3], the only appreciable difference being that in contrast to Held and Menzel, we observe extra intensity and structure at energies above 200 eV . An immediate 40-170 eV follow up scan showed no discernable change to the IV profile, implying that the film was not being inadvertently damaged with the LEED beam during the scans. In addition, the subsequent TPD spectrum (figure 4.5) had none of the features associated with a

dissociated overlayer.
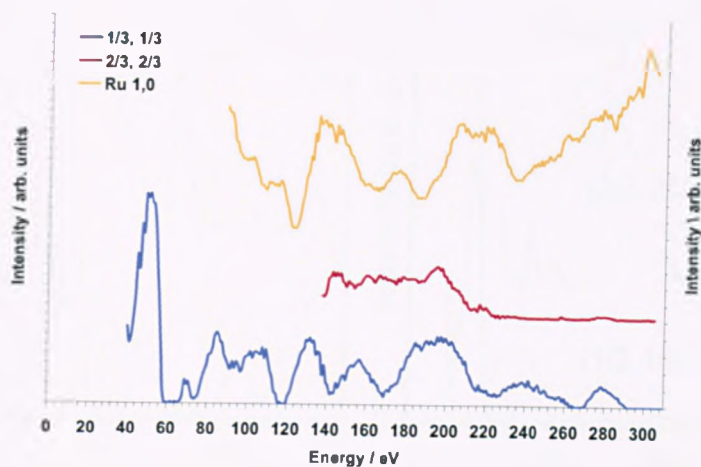
Figure 4.3: LEED IV profiles for the first and second order $\sqrt{3}$ spots (1/3, 1/3 and 2/3, 2/3, respectively) along with the first order (1,0) Ru spots, following a 40-400 eV IV scan of an intact D_2O layer on Ru (0001).

In contrast, the I-V profiles from a D_2O adlayer subjected to relatively high beam currents are shown in figure 4.6 and are markedly different from those for an intact wetting layer, with no structure visible after 140 eV . Qualitatively, upon electron damage of the wetting structure, the pin-sharp $(\sqrt{3} \times \sqrt{3})R30°$ spots (figure 4.7) give way to the distinctive streaked LEED pattern shown in figure 4.8. Moreover, the follow up TPD spectrum (after dissociation) exhibits a distinctive shoulder on the high temperature side of the monolayer peak (figure 4.9), which becomes more prominent with increased exposure of the wetting layer to the LEED beam.

The similarity of our LEED IV profiles to those of Held and Menzel [3] suggests that their LEED IV simulations were indeed for an intact wetting structure. This is not surprising, given the extensive efforts that these authors took to minimise
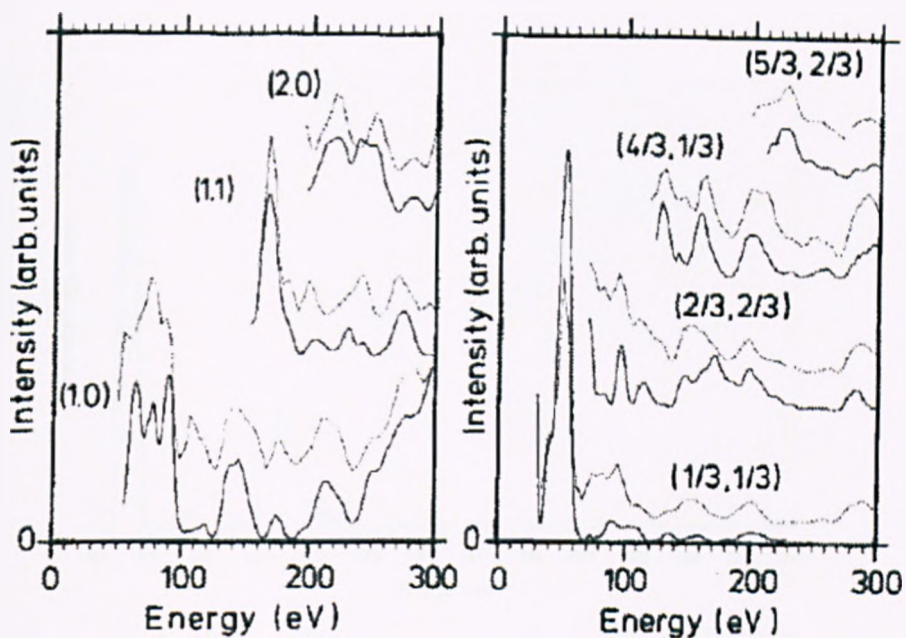
Figure 4.4: LEED IV profiles for the Ru (left) and the $(\sqrt{3} \times \sqrt{3})$R30° spots (right) from the original LEED IV study of Held and Menzel [3]. Note: the darker curves are from experiment while the lighter curves are from LEED IV simulations.
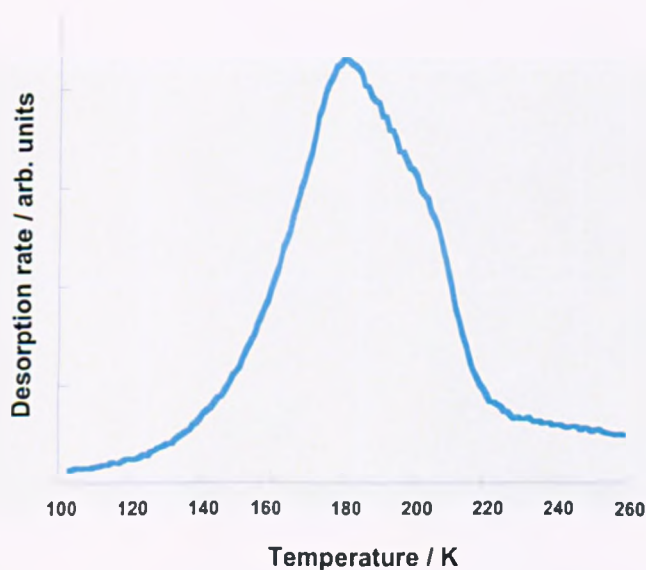
Figure 4.5: The TPD profile from a D_2O monolayer on Ru (0001) after LEED IV measurements.
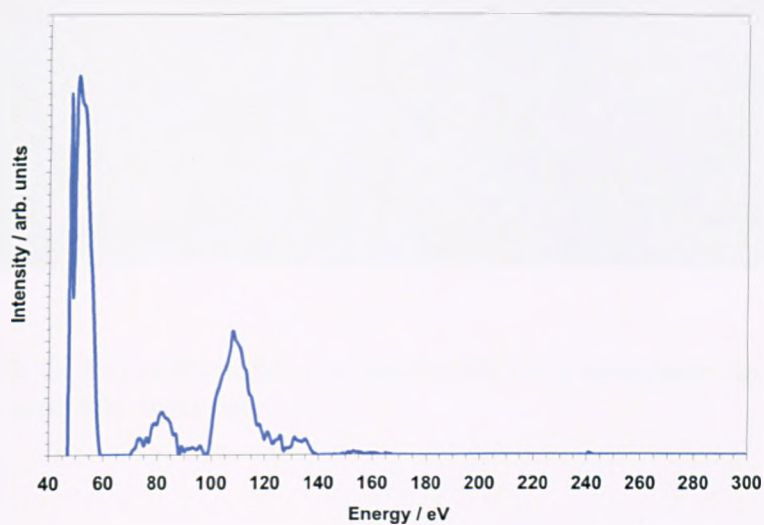
Figure 4.6: LEED IV profiles of the first order $\sqrt{3}$ spots from an electron-beam damaged D_2O layer on Ru (0001).
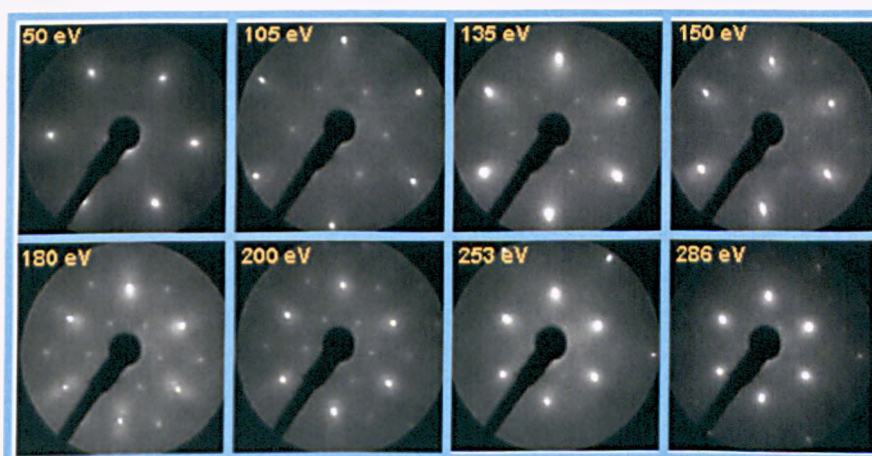
Figure 4.7: LEED pattern from an intact D_2O monolayer on Ru (0001), showing the first order $(\sqrt{3} \times \sqrt{3})R30°$ spots.

Figure 4.8: LEED pattern from a dissociated D_2O monolayer on Ru (0001) after extended electron exposure.
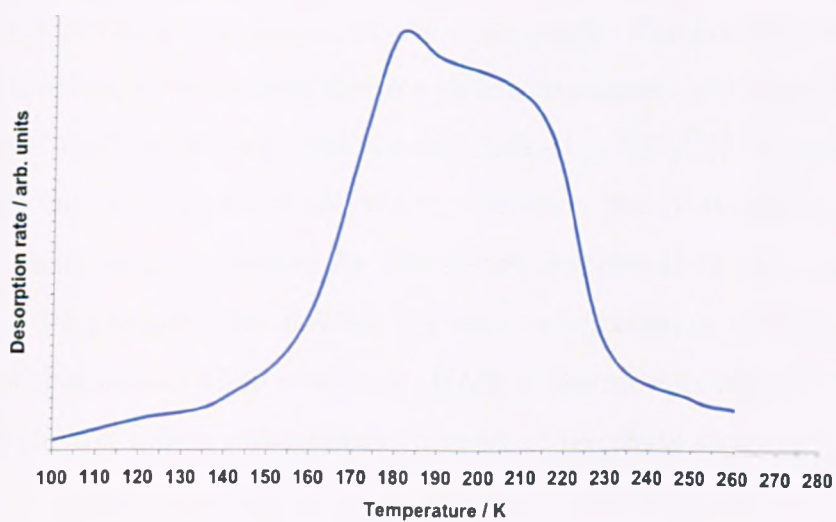
Figure 4.9: The TPD profile from a D_2O monolayer on Ru (0001) following deliberate electron induced damage.

the effect of the LEED beam on their I-V data. Consequently, we can dismiss Feibelman's [19] suggestion that the flattened O layer found in Held and Menzel's I-V analysis was due to partial dissociation. However, having ruled out electron damage, the flat geometry of their best-fit structure is still problematic since it does not agree with the DFT calculations for an intact bilayer or explain how water wets the Ru (0001) surface.

A more plausible wetting layer structure was recently proposed by Haq and co-workers [4]. This structure (figure 4.10) consists of disordered, short chains of flat and H-down water molecules, imbedded in a honeycomb hydrogen-bonded network. Crucially, while this hydrogen-bonding network imposes long-range order on the adlayer it allows for substantial local disorder. Moreover, in contrast to the rigid alternation in the geometry of the water molecules, intrinsic to the conventional bilayer model, the formation of chains is expected to give substantial disorder in the wetting layer, associated with the proton orientation along the chains, the direction of the chains and the chain length. Furthermore, because the hydrogen-bonding network gives rise to a strong long-range order in the lateral location of the water molecules, there is a well-defined $(\sqrt{3} \times \sqrt{3})R30°$ periodicity in the O sites. On the other hand, the water orientation (flat or H down) is expected to show a short-range preference for having two neighbours of the same orientation, but no long-range order in either the water orientation or the O height. It is anticipated that helium atom scattering (HAS) measurements from the water/Ru (0001) system will reflect this intrinsic disorder of the chain structure.

4.3.3   Helium Atom Scattering from H₂O and D₂O Layers

The reflectivity of the water monolayer to He is extremely low, thus the presence of any ordered contamination, however minor, has a substantial effect. We observe that annealing the Ru crystal to higher temperatures (1400 K) during cleaning cycles induces an ordered impurity structure on the "clean" surface. The origin
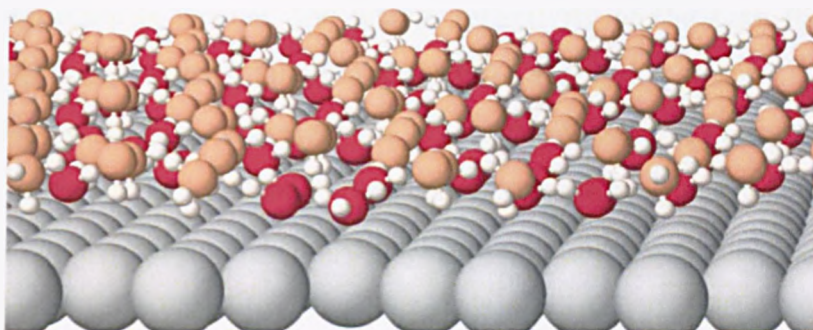
Figure 4.10: The disordered 'chain structure' proposed by Haq *et al.* [4] for the wetting layer on Ru (0001), showing the flat-lying (red spheres) and H-down (orange) water molecules

and precise nature of this structure is not known. However, we speculate that it may arise from the segregation of impurities from the bulk of the crystal, most likely carbon, to form relatively small regions of ordered superstructure on the surface. In Helium scattering this structure is manifested as sharp satellite peaks on either side of the specular signal at a momentum transfer of $\Delta k_{\parallel} = \pm 0.23$ Å $^{-1}$. Moreover, these peaks are stable for water coverages ranging from a monolayer to large multilayer films. The satellite peaks disappear underneath the specular peak for a water free surface and are thus only visible when the bare Ru reflectivity is reduced by water adsorption. This impurity structure also appears in LEED, for both the bare metal and a water covered surface, as a weak, multiple spot pattern at around 10-40 eV , with the same momentum transfer. Even when this impurity structure is formed, the helium reflectivity of the bare Ru surface is extremely high and indeed comparable to the clean 1 × 1 beams. Thus, we do not consider the helium reflectivity as a reliable measure of surface cleanliness. Likewise, annealing the surface to very high temperatures (1400 K) produces a shoulder in the monolayer D_2O TPD peak, which indicates partial dissociation or the presence of contamination. However, this problem can easily be avoided by reducing the anneal temperature to around 1100 K. This is found to consistently produce a good (1 × 1) surface, as confirmed by LEED, HAS and TPD, while avoiding segregation of bulk material to the surface.

The top panel of figure 4.1 shows the TPD spectrum from desorption of 2.3 layers of D_2O (dashed black line) and a simultaneous measurement of the change in the He specular reflectivity (blue line - raw data, red line - smoothed). As the surface is heated, there is no visible change in the reflectivity until about 150 K, where a small step coincides with multilayer desorption. The helium reflectivity then plateaus until the monolayer begins to desorb. With the onset of monolayer desorption the bare Ru surface is increasingly exposed, corresponding to a very sharp increase in the helium reflectivity. This is more evident in the lower panel of

figure 4.1, which shows the derivative of the helium intensity as a function of the surface temperature. The comparison of this intensity with the TPD spectrum reveals that the largest change in intensity occurs as the monolayer desorbs, with scant variation elsewhere. Interestingly, we find that the helium reflectivity on the plateau, just before the onset of monolayer desorption is only about ~0.05 % of the reflectivity from the bare Ru surface. This is surprisingly low compared to previous reports in the literature, where the He intensity at the same region in the TPD spectrum was found to be 0.2-0.3 % [76] or 3-6 % [75] of the bare Ru signal. These values are, respectively, 5 and 100 times higher than the value we report here. We also find that the He reflectivity in the region just before monolayer desorption is considerably higher if partial dissociation is induced in the water layer, by exposing it to high electron doses using the LEED beam, or by heating a structure containing H_2O to above 150 K. This increased reflectivity, together with a high temperature tail in the TPD, is also evident for ice layers grown using the background dosing method, again implying partial dissociating of the water layer. In contrast, D_2O layers prepared via the molecular beam method only show a slow decrease in the reflectivity above 190 K (figure 4.1, which is associated with Debye-Waller effects. Importantly, no increase is observed in the reflectivity near 200 K that would suggest decomposition of a partially dissociated structure [23].

We investigated the structure of an ice layer by measuring the angular scattering profile as a function of the water coverage and the preparation conditions. The helium scattering from an intact D_2O layer is shown in figure 4.11a. The coverage of the ice layer is optimised so as to give a sharp $(\sqrt{3} \times \sqrt{3})R30°$ LEED pattern, which coverage dependence experiments show forms at ~0.67 ML coverage, slightly below the monolayer saturation coverage of 0.75 ML [59] [4]. The blue line in figure 4.11 depicts a wide angle (20-70°) He scattering profile, which corresponds to a parallel momentum transfer $\Delta k_\parallel$ of up to ± 6 Å $^{-1}$ along the [11$\bar{2}$0] direction while red line shows the angular scattering profile from the clean

Ru surface (divided by a factor of 2000). Even though LEED shows a well-defined $(\sqrt{3} \times \sqrt{3})R30°$ pattern, we find no evidence of sharp diffraction peaks in the helium studies that would indicate classical elastic diffraction. Instead we observe broad maxima centred near (although not exactly at) the position expected for second order $\sqrt{3}$ diffraction. Contrary to recent reports by Traeger *et al.* [75], we observe no satellite peaks near the specular reflection, as is clear from figure 4.11. On the other hand, the HAS shown here resembles the findings of Kondo *et al.* [76], which was attributed to a $(\sqrt{3} \times \sqrt{3})R30°$ ice bilayer. They argued that the absence of first order diffraction was due to the large corrugation in the interaction potential between He and the Ru surface.

The broad maxima in the helium scattering intensity are inconsistent with that expected from a well-ordered $(\sqrt{3} \times \sqrt{3})R30°$ bilayer structure. Indeed, we found this intensity maximum did not even depend on the scattering azimuth and appeared at approximately the same position following rotation of the sample to scatter along the Ru rows. What is more, the HAS pattern shown in figure 4.11 was also found to be essentially independent of coverage. In fact, from 0.5 to 1.5 layers the only noticeable change was a decrease in the intensity close to the specular peak as coverage went beyond 0.67 ML; this was equally true for H_2O as well as D_2O . In addition, limited exposure to the LEED beam had no discernable effect on the HAS pattern. For higher coverages the disordered multilayer forms clusters on top of the monolayer and consequently the intensity of the specular reflection diminishes rapidly to background levels.

As mentioned before, adsorbing H_2O below 150 K produces a non-dissociated layer. The dotted line in figure 4.11(b) shows the HAS profile from a saturated, intact H_2O layer. Although, the general features of the HAS are rather similar to that obtained for D_2O , the specular reflectivity is slightly higher and the diffuse peaks near the second order positions are slightly sharper for an H_2O layer. In addition, for H_2O there is a weak intensity rise near $\Delta k_{\parallel} = \pm 1.5$ Å $^{-1}$, which
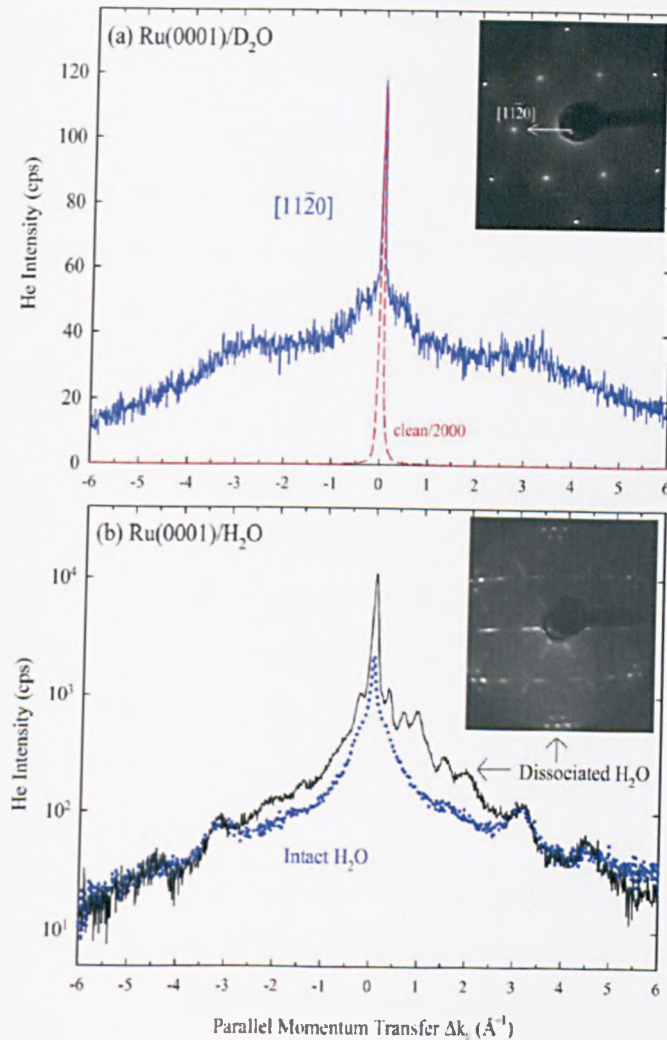
Figure 4.11: (a) He atom scattering over the parallel momentum transfer range $\Delta k_\parallel$ of $\pm$ 6 Å^{-1} for clean Ru(0001) (dashed red line, divided by 2000) and a saturated D_2O layer (solid blue line) along the [11$\bar{2}$0] direction. No classical elastic diffraction peaks corresponding to a $(\sqrt{3} \times \sqrt{3})$R30° structure are observed. Inset: LEED pattern (55 eV) from a saturated D_2O layer. This pattern shows no change following the HAS experiments, indicating that the He beam does not perturb the water structure. (b) HAS of an intact H_2O layer (dotted blue line) and a deliberately dissociated structure (solid line) grown at 165 K. Inset: LEED (56 eV) corresponding to a dissociated H_2O layer grown at 165 K.

cannot be resolved in the D_2O distribution shown in figure 4.11a.

For layers grown at above 152 K, dissociation of the H_2O structure always ensued. The solid black line in figure 4.11b depicts the HAS profile for an H_2O layer adsorbed at 165 K. At these temperatures multilayer is unstable, leading to the formation of a complete layer of dissociated H_2O. The resulting HAS profile shows a series of somewhat sharper diffraction peaks along the $[11\bar{2}0]$ azimuth. What is more, the specular reflectivity is enhanced by a factor of ∼5 as compared to the intact H_2O phase. These additional features in the HAS are consistent with the LEED patterns obtained from this layer (inset figure 4.11b). This streaked LEED pattern has been reported previously and is thought to arise from domains of mixed OH/H_2O interspaced by areas of H covered Ru [23]. Moreover, this LEED pattern has sharp features around the central beam, oriented to the $\sqrt{3}$ direction, the spacing of which corresponds to the HAS peaks. In addition, the $\sqrt{3}$ LEED beams are surrounded by satellite spots and connected with lines of intensity. That both the H_2O and D_2O layers fail to produce the sharp HAS diffraction anticipated for an ordered $(\sqrt{3} \times \sqrt{3})R30°$ bilayer indicates that such a structure can be excluded on this surface.

On the other hand, the HAS data is consistent with a highly corrugated albeit disordered He-surface potential. Due to the low electron scattering cross section of H and D, the ordered LEED pattern reflects the ordering of the O and Ru atoms. At the correct coverage (∼2/3 ML) ordered domains of O atoms are formed in the water layer giving rise to a sharp $\sqrt{3}$ LEED pattern. In contrast, the HAS shows no such coverage dependence, which indicates that the top layer of atoms in the water structure is disordered even when the LEED shows long-range $\sqrt{3}$ order. In the following discussion, we argue that this picture is consistent with a $(\sqrt{3} \times \sqrt{3})R30°$ water layer that has periodicity in the O sites within an intrinsically disordered hydrogen bonding structure. It is worthy of note that while the remainder of this discussion is based on the formation of idealised 0.67 ML

water structure, in practice, water is not constrained to form extended domains at low coverage and will indeed accommodate more water if adsorption is continued [59] [4].

4.3.4 Discussion: DFT Calculations and the Structure of the 0.67 ML Wetting Layer

DFT calculations for the water/Ru (0001) system [19] have consistently suggested that the binding energy of an intact bilayer is less than in bulk ice and therefore should not wet the Ru (0001) surface. However, it is important to note that a generic drawback of DFT has been its inadequacy in capturing the essence of Van der Waals forces, which can lead to an underestimation in the binding energy of water films. A comparison of this system with Ar adsorption on Ru (0001) [77] indicates that the incomplete inclusion of dispersion interactions in the DFT calculations is not enough to explain the discrepancy between the binding energy of the bilayer and bulk ice. Consequently, the structure of the intact bilayer remains unclear.

As mentioned earlier, Haq and co-workers recently suggested disordered chains of flat and H-down water molecules as a model of the 2/3 ML intact monolayer on Ru (0001). To test this model, DFT calculations using the plane-wave basis set VASP code were recently performed by George Darling [4]. These calculations employed the standard ultra-soft pseudo-potentials for all atoms while exchange and correlation were treated with the PW91 generalized gradient approximation. In addition, a plane-wave cut-off energy of 396 eV was used. The surface was represented by a three-layer slab of Ru, with the experimental lattice constants and the bottom two layers fixed in position. A vacuum gap of 12 Å was measured from the H atom furthest from the surface. Moreover, a 3 × 3 × 1 Monkhorst-Pack k-point set was used to sample reciprocal space. For super-cells larger than $(2\sqrt{3} \times 2\sqrt{3})$, tests were performed by varying the k-point set to maintain the

same density of k-points in each dimension. However, the influence on the final binding energies was found to be insignificant.

The 2/3 ML water structure with the highest binding energy on the Ru (0001) surface is shown in figure 4.12. In this model, which produced a binding energy of 0.655 eV per molecule, half the water molecules lie flat atop the Ru atoms, while the other half adopt an H-down orientation. Darling found that obtaining *a favourable binding energy was heavily dependent on the existence of extended* chains of flat lying water, with a short hydrogen bond of ~1.67 ± 0.02 Å . The most salient feature in Darling's model is that in order to maximise this bonding, the adlayer must forgo the stringent $(\sqrt{3} \times \sqrt{3})$R30° symmetry enforced upon it in previous models. This increases the binding energy of the adlayer by 24 % relative to the H-down version of the $(\sqrt{3} \times \sqrt{3})$R30° bilayer. It is worthy of note that even in its simplest form, the structure shown in figure 4.12a, has an element of disorder associated with the positions of the H-down water molecules. For this structure it was found that the O atoms of the flat lying water molecules deviate from the atop Ru positions by only 0.06 Å (RMS).

In contrast, the O atoms of the H-down water molecules *were found to have* an RMS lateral displacement of 0.22 Å . Moreover, these H-down chains have long (weak) hydrogen bonds between water molecules and do not form a direct bond with the Ru surface. In other optimization runs, Darling observed the H-down lateral displacements increase to as high as 0.58 Å after a displacement of the whole H-down chain. However, this had *no* discernable effect on the binding energy of the structure. The implication is that, as long as the complete hydrogen-bonding network is sustained, the binding energy of the structure is relatively insensitive to the exact position of the H-down chain above the Ru surface. Furthermore, more disorder can be introduced into the structure by changing the direction of the O-H bonds without detriment to the overall bonding network.

An important feature in the above structure is that the direction of the wa-
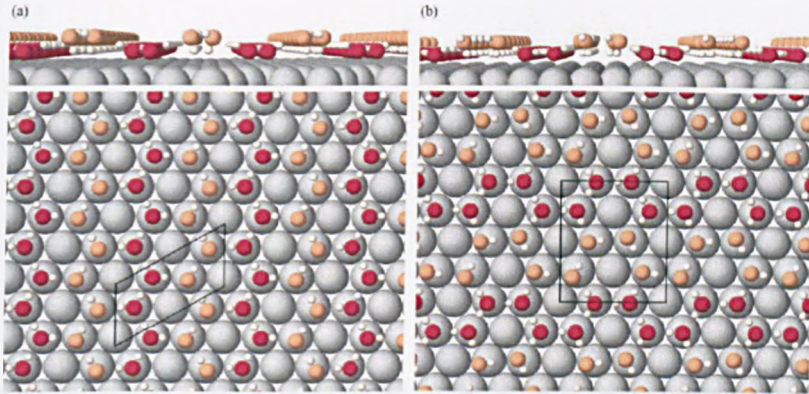
Figure 4.12: Minimum energy structures for an intact water layer calculated in (a) a ($\sqrt{3} \times 2\sqrt{3}$) and (b) a ($3 \times 2\sqrt{3}$) unit cell. Water forms chains of flat water (O atoms represented by dark red spheres) and H-down water (O indicated as orange spheres) embedded within the overall hydrogen bonded hexagonal network. Taken from [5].

ter chains is not constrained. Thus, substantial changes to the structure can be made by simply altering the chain direction. For instance, in figure 4.12b a bend has been introduced into the chain by altering the position of the flat-lying water molecules, creating chains that run along the close pack direction. Each water molecule within the flat chain still donates and accepts one hydrogen bond while donating the remaining hydrogen bond to the H-down water chain. This structure produced a binding energy of 0.648 eV per molecule, in effect the same as the original chain structure. The implication is that the direction of the flat lying chains is likely to be entirely random within the overall hydrogen bonded honeycomb structure.

A simpler way of making every flat-lying water molecule form a hydrogen bond with two other waters in the same geometry is by forming closed rings. This is illustrated in figure 4.13, which shows a structure made up of hexagons of flat-lying water molecules with one hydrogen bond to chains of H-down water molecules. Moreover, the H-down chains are decorated with H-down water molecules that
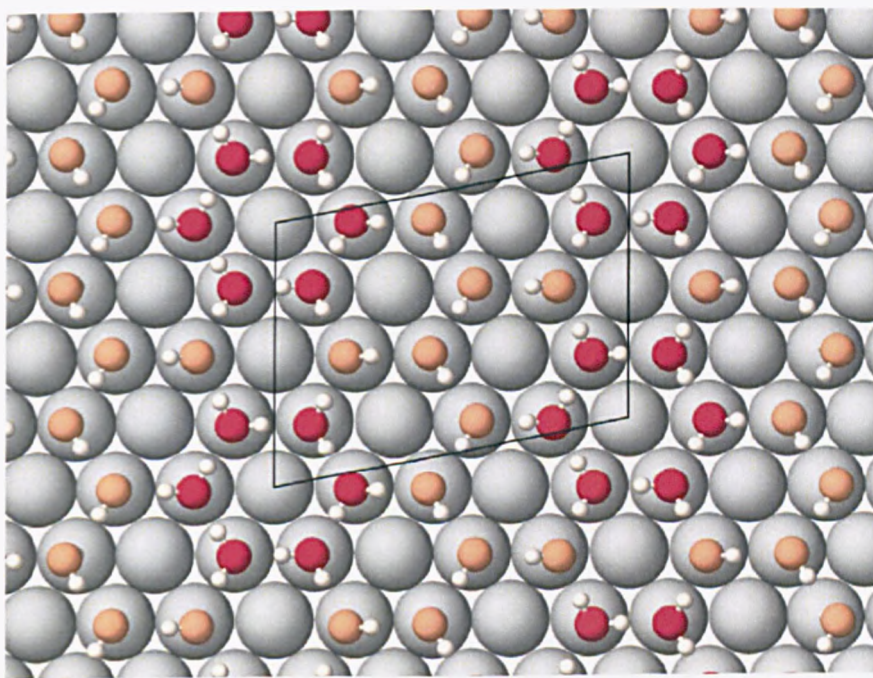
Figure 4.13: A water network containing cyclic rings of flat water, arranged in a $(2\sqrt{3} \times \sqrt{21})$ unit cell. Taken from [5].

branch off and two hydrogen bonds with water molecules in the same flat-flying geometry. Importantly, the idea of unbroken flat-lying "chains" is preserved within this structure. Thus, it still has a relatively high binding energy of 0.639 eV per water molecule.

As mentioned previously, the stability of these chain structures is strongly associated with the formation of chains of flat-lying water molecules. However, Darling also explored the energy cost of terminating these chains by calculating binding energies for structures with a range of chain lengths, as shown in figure 4.14. In all of these structures, half the water molecules lie flat while the other half is H-down. However, as the chains get shorter, the number of hydrogen bonds between water molecules with different geometry increases.

For instance, water chains two molecules long (figure 4.14a) produced a binding energy of 0.596 eV / molecule, which increases slightly, to 0.604 eV /molecule, as the chain length becomes three water molecules long. For chains consisting of four water molecules, Darling examined two different structures. The first structure (figure 4.14c) consisted of a linear chain, related to the structure in figure 4.12a and produced a binding energy of 0.631 eV /molecule. The other four molecule chain (related to the structure in figure 4.12b) has water molecules arranged in simple arcs and was found to be slightly less favourable than the linear chain, with a binding energy of 0.621 eV /molecule (figure 4.14d). A five unit chain structure with a compact unit cell (figure 4.14e), which probably restricts the amount of relaxation of the H-down water molecules produced a binding energy of only 0.621 eV /molecule. On the other hand the six unit chain shown in figure 4.14f produced a binding energy of 0.627 eV /molecule. It should be noted here that the structures in figure 4.14 for chains of varying lengths are only representative. Indeed, in most cases there are other possible arrangements of the water molecules that would produce the same chain length.

The structures shown in figure 4.14 are still well ordered chain-like arrange-
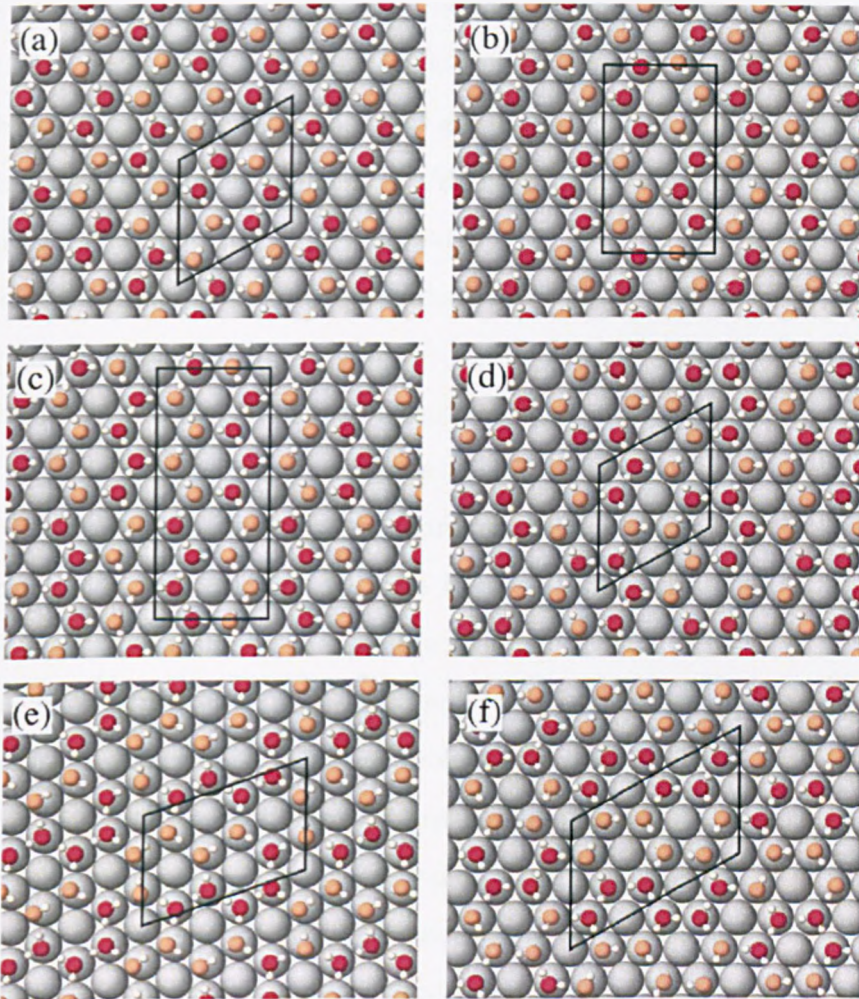
Figure 4.14: Calculated structures for water arranged in chains of different length within the overall hydrogen bonding network. Each water molecule always has three hydrogen bonds to neighbouring molecules, but is arranged with chains of (a) two, (b) three, (c) and (d) four, (e) five and (f) six flat-lying waters respectively. Taken from [5].

ments of the water molecules. However, Darling also used the DFT calculations to estimate the binding energy cost of introducing single errors and branches in these chains. The resulting models are illustrated in figure 4.15. The exchange of a single flat-lying water molecule and H-down water molecule is depicted in figure 4.15a. This arrangement consists of a flat-lying molecule with three hydrogen bonds to H-down water molecules and an H-down molecule with three hydrogen bonds to flat-lying water molecules. Although, these units formed the basis of the H-down version of the conventional bilayer model [74], both configurations are inherently unfavourable, as is evident from the subsequent reduction in the binding energy from 0.655 to 0.615 eV /molecule. Moreover, Darling found that while the H-down water molecule accepts two hydrogen bonds of medium length (1.77-1.87 Å) it donates a much longer ($\sim$2.37 Å) one. In contrast, complete chains of H-down molecules have a hydrogen bond length of 1.93-2.0 Å .

Because it is not possible to have branches in infinite chains with a finite unit cell, Darling considered branched structures of finite length. In figure 4.15b a branch is introduced at the right-hand side of a chain of flat-lying water molecules. In contrast, in figure 4.15c the last molecule at the left-hand side of the structure is moved down to form another branch on that side of the chain. These two structures were found to have identical binding energies (0.634 eV /molecule), which suggests that there is no preference for or against branch formation within the chain as long as the number of flat-lying-to-flat-lying hydrogen bonds is preserved. Finally, Darling considered the binding energy cost of orienting one water molecule H-up in one of these large-scale structures. For example, orienting one water molecule H-up in the structure shown in figure 4.15b produces the structure in figure 4.15d. This structure produced a binding energy of 0.631 eV /molecule, which seems little but actually amounts to a destabilization (increase in the total energy) of $\sim$70 meV for the unit cell indicated. Moreover, replacing complete H-down chains with H-up chains in figure 4.15 leads to a large decrease in the

binding energy to 0.564 eV .
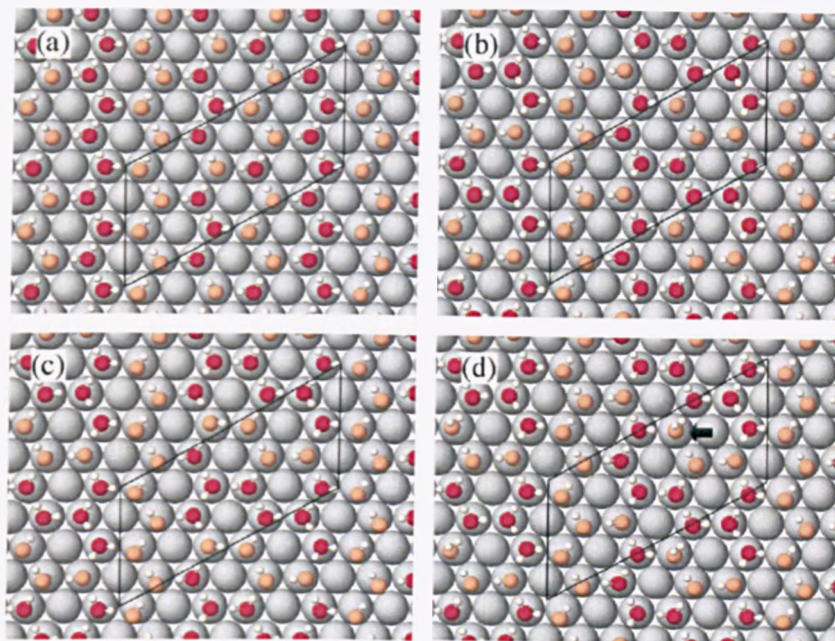
Figure 4.15: Water networks containing disordered chains, calculated in a $(2\sqrt{3} \times 4\sqrt{3})$ unit cell. (a) Exchange of one flat and one H-down water to break half of the infinite chains into units of three waters. Branched chain structures containing (b) one flat and one H-down water and (c) two flat waters each coordinated by three waters of the same geometry. (d) Structure (b) but with one H-down water replaced by an H-up species (arrowed). The binding energies were calculated as 0.615, 0.634, 0.634 and 0.631 eV respectively. Taken from [5].

Interestingly, Darling found that all of the calculated structures had certain common features. For instance, the flat-lying water molecules adsorb almost exactly atop the Ru atoms and have Ru-O bond lengths of ~2.36 to ~2.40 Å . In addition, the RMS lateral deviation of O ranged from 0.06 Å for the optimum structure shown in figure 4.12 to 0.154 Å for the unfavourable 2-unit chains (figure 4.14a). In contrast, the H-down molecules were found to have a much greater deviation from exact atop adsorption. For example the 4-unit chains, depicted in figure 4.14d, had an RMS lateral deviation of ~0.15 Å , which increases to

~0.58 Å for the wiggles shown in figure 4.15b. This greater lateral displacement in the H-down chains arises from the chain structure itself. Unlike the standard $(\sqrt{3} \times \sqrt{3})R30°$ bilayer structures, molecules in the chain structure are not symmetrically bound to flat-lying molecules. Consequently, they are able to tilt slightly and displace themselves to improve the hydrogen bonding to their flat-lying neighbours. On average, Darling found that the lateral deviation within the H-down chains is more than three times that of the flat-lying water.

Figure 4.16 shows a plot of the binding energy of different structures as a function of the fraction (f_s) of short hydrogen bonds (i.e. flat water- flat water) within the computational unit cell. This fraction, f_s ranges from 0, for the traditional bilayer structures (H-down, H-up and mixed H-up/H-down), to 0.33 for the optimum chain structures depicted in figure 4.12. It is clear from the graph that there is a good correlation across all the structures, thus emphasising the importance of short hydrogen bonds within the flat-lying chains. The graph also shows that structures with the same f_s can have a range of different binding energies. However, the exact details of the bonding of flat chains to H-down molecules and within H-down chains, influences the binding energy to a lesser extent than completion of the flat-lying chains. For example, at $f_s = 0.33$ there are three structures (figures 4.12 and 4.13) with a range of binding energies. Similarly, at $f_s = 0.25$, the structures depicted in figures 4.14c, 4.14d and 4.15a have a range of binding energies. A similar, albeit weaker, correlation was also observed between the binding energy and the O-Ru bond length. This is illustrated in figure 4.17.

In addition to the energetic stability of the different water structures, their relative free energy will also be influenced by entropy effects. Recently, Feibelman and Alavi showed that the residual Pauling-type entropy of a surface bilayer at 150 K reduces the free energy relative to a 3D ice crystal by 4.5 meV /molecule, with vibrational entropy contributing a similar amount. The chain structures described above are intrinsically disordered, with no long-range correlation in the geometry
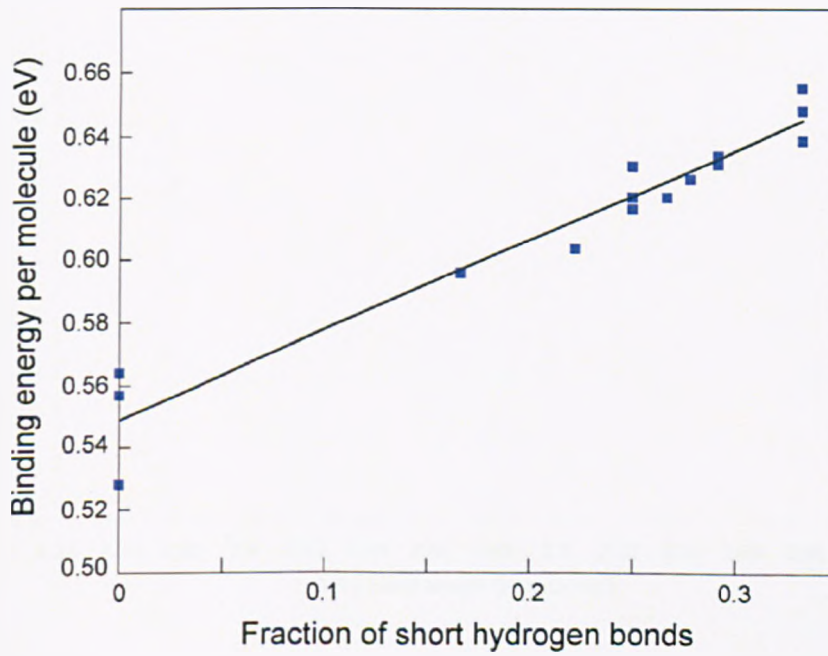
Figure 4.16: Calculated binding energy as a function of the number of hydrogen bonds between flat lying water molecules. Taken from [5].
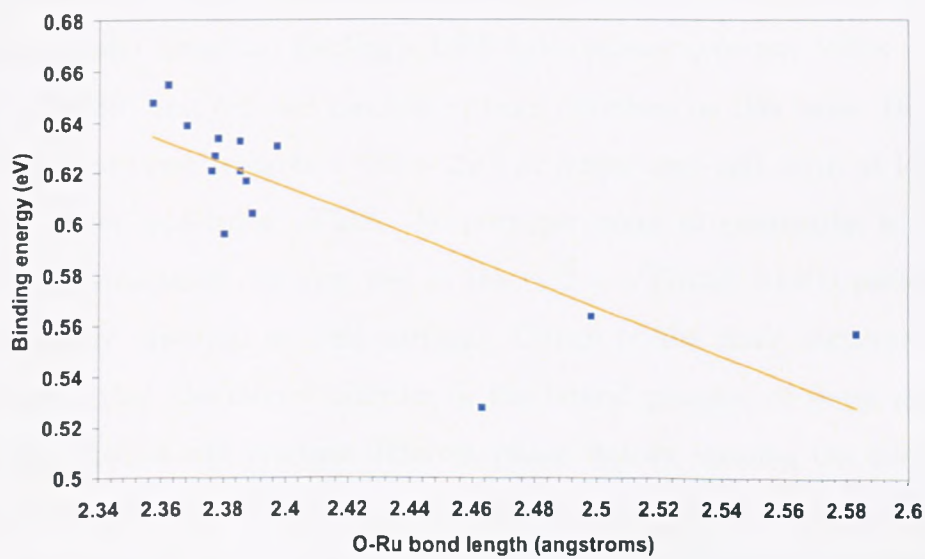
Figure 4.17: Calculated binding energy as a function of the O-Ru bond length. From the DFT Calculations of George Darling [79].

of the water molecules (flat or H-down) or in the heights of O atoms. Terminating the flat chains was found to add to this disorder but with some detriment to the binding energy.

4.3.5 LEED Patterns for the Chain Structure

As mentioned before, based on the observation of (1/3, 1/3) LEED spots for the 2/3 ML water layer [3], the wetting layer on the Ru (0001) surface has traditionally been anticipated to have a simple $(\sqrt{3} \times \sqrt{3})$R30° unit cell. In contrast, the chain structure model based on Darling's DFT calculations does not follow a simple $(\sqrt{3} \times \sqrt{3})$R30° unit cell and has indeed been criticised on this basis. Describing the chain structures requires a $\sqrt{3} \times 2\sqrt{3}$ or larger unit cell, with at least four different water molecules. Thus, the principle point of contention is whether these chain structures can give rise to the $(\sqrt{3} \times \sqrt{3})$R30° LEED pattern that is consistently observed on this surface. Critics of the chain structure model have argued that the lateral disorder in the lateral position of water molecules of different height will produce different phase factors, causing the intensity of $\sqrt{3}$ superstructure LEED beams to average to zero. In addition, formation of more ordered chain structures would produce additional diffraction beams that are inconsistent with experiment. Indeed, this picture underpinned the original LEED I-V analysis of Held and Menzel [3], from which they concluded that the wetting layer has a coplanar geometry.

Here we examine this picture more closely by considering the structure factor for different hexagonal water networks. We show that a water layer that is disordered in the vertical (orientational) location of the O atoms, while maintaining a well-defined lateral periodicity, will give rise to a well-defined LEED pattern. We note the analysis presented below is entirely qualitative in that multiple scattering is not taken into account. However, although multiple scattering will affect the relative intensity of the diffraction beams, it cannot remove their intensity at all

energies. We then examine the extent to which this simple structure factor model is sensitive to disorder in the location of the oxygen atoms.

As shown in the previous sections of this chapter, DFT calculations imply that water adsorbs on the Ru (0001) to form a hexagonal network in a commensurate atop site, which is consistent with the site found in Held and Menzel's LEED I-V simulation. Moreover, each water molecule in this arrangement forms three hydrogen bonds with its neighbours. Now, if we consider an $n\sqrt{3} \times m \sqrt{3}$ island containing 2N water molecules, where m and n are integers and $N = n \times m$, the subsequent diffraction beams will have intensity as long as the structure factor ($F_{h,k}$) does not go to zero. The overall structure factor for the island is given by,

$$F_{h,k} = \sum f_n e^{2\pi i (\vec{G} \cdot \vec{r}_n)} = \sum f_n e^{2\pi i (h u_n + k v_n + \Delta k_z z_n)}$$

where the sum runs over all the atoms in the structure. The position of the O atoms is defined by $\mathbf{r}_n = u_n \mathbf{a}_1 + v_n \mathbf{a}_2 + z_n \mathbf{j}$ (where $\mathbf{a}_1$, $\mathbf{a}_2$ and $\mathbf{j}$ are real space vectors) and $\mathbf{G}_{h,k} = h \mathbf{b}_1 + k \mathbf{b}_2$ (where $\mathbf{b}_1$ and $\mathbf{b}_2$ are reciprocal space vectors). $\Delta k_z = (k_{zi} - k_{zf})$ denotes the change in wavevector perpendicular to the surface. The intensity of the $\sqrt{3}$ beams is then obtained by calculating the structure factor $|F_{h,k}|^2$ or its equivalent. For instance, the structure factor for a hexagonal network, with the O atoms exactly atop Ru, at heights $z_{O_A}^{p,q}$ and $z_{O_B}^{p,q}$, in sub-cell (pq) is given by,

$$F_{n,m} = \sum_{p,q=0}^{n-1,m-1} f_O \left[e^{2\pi i(pn/n+qm/m+\Delta k_z z_{OA}^{p,q})} + e^{2\pi i(pn/n+n/3n+qm/m+m/3m+\Delta k_z z_{OB}^{p,q})} \right]$$

$$= \sum_{p,q=0}^{n-1,m-1} f_O \left[e^{2\pi i(p+q)} e^{2\pi i(\Delta k_z z_{OA}^{p,q})} + e^{2\pi i(p+q)} e^{2\pi i(1/3+1/3)} e^{2\pi i(\Delta k_z z_{OB}^{p,q})} \right]$$

$$= \sum_{p,q=0}^{n-1,m-1} f_O e^{2\pi i(p+q)} \left[e^{2\pi i(\Delta k_z z_{OA}^{p,q})} + e^{4\pi i/3} e^{2\pi i(\Delta k_z z_{OB}^{p,q})} \right]$$

$$= \sum_{p,q=0}^{n-1,m-1} f_O \left[e^{2\pi i(\Delta k_z z_{OA}^{p,q})} + e^{4\pi i/3} e^{2\pi i(\Delta k_z z_{OB}^{p,q})} \right]$$

Thus, different arrangements of the O height ($z_{OA}^{p,q}$ and $z_{OB}^{p,q}$), within the hydrogen bonded superstructure will produce different values for the structure factor. However, for none of these arrangements will the structure factor (and hence the intensity of the diffraction peaks) be uniquely zero. For example, a situation where the height of the O atoms, within the network, is entirely random, with no correlation whatsoever, leads to a structure factor of, $F_{n,m} = N f_O \langle e^{2\pi i(\Delta k_z z_O)} \rangle \left[1 + e^{4\pi i/3} \right]$ where $\langle e^{2\pi i(\Delta k_z z_O)} \rangle$ is just the expectation value for the O phase factor, averaged across the entire $n\sqrt{3} \times m\sqrt{3}$ network. For two water molecules with different geometry (i.e. flat and H-down) and with heights, z_{OA} and z_{OB}, this just corresponds to the average,

$$\langle e^{2\pi i(\Delta k_z z_O)} \rangle = \left(\langle e^{2\pi i(\Delta k_z z_{OA})} \rangle + \langle e^{2\pi i(\Delta k_z z_{OB})} \rangle \right) /2.$$

Thus, even for an entirely random arrangement of water orientations within the hexagonal network, the structure factor will be explicitly non-zero, which means that $\sqrt{3}$ LEED beams would indeed be anticipated for this configuration.

Similarly, a coplanar array of O atoms, in which $z_{OA}^{p,q} = z_{OB}^{p,q}$, produces the

structure factor,

$$
\begin{aligned}
F_{n,m} &= \sum_{p,q=0}^{n-1,m-1} f_O \left[e^{2\pi i(\Delta k_z z_{OA}^{p,q})} + e^{4\pi i/3} e^{2\pi i \Delta k_z z_{OB}^{p,q}} \right] \\
&= \sum_{p,q=0}^{n-1,m-1} f_O\, e^{2\pi i(\Delta k_z z_{O}^{p,q})} \left[1 + e^{4\pi i/3} \right] \\
&= N f_O \left[1 + e^{4\pi i/3} \right] e^{2\pi i(\Delta k_z z_O)}
\end{aligned}
$$

Once again this is non zero and so a $\sqrt{3}$ LEED pattern is once more expected. Likewise, for an ordered bilayer, $z_{OA}^{p,q} = z_{OA}$ and $z_{OB}^{p,q} = z_{OB}$, which produces the (non-zero) structure factor,

$$
\begin{aligned}
F_{n,m} &= \sum_{p,q=0}^{n-1,m-1} f_O \left[\exp^{2\pi i(\Delta k_z z_{OA}^{p,q})} + e^{4\pi i/3} e^{2\pi i \Delta k_z z_{OB}^{p,q}} \right] \\
&= \sum_{p,q=0}^{n-1,m-1} f_O \left[e^{2\pi i(\Delta k_z z_{OA})} + e^{4\pi i/3} e^{2\pi i(\Delta k_z z_{OB})} \right] \\
&= N f_O \left[e^{2\pi i(\Delta k_z z_{OA})} + e^{4\pi i/3} e^{2\pi i(\Delta k_z z_{OB})} \right] \\
&= N f_O e^{2\pi i(\Delta k_z z_{OA})} \left[1 + e^{4\pi i/3} e^{2\pi i(\Delta k_z z_{O})} \right]
\end{aligned}
$$

Indeed, provided that $\left\langle e^{2\pi i(\Delta k_z z_O)} \right\rangle$ is non-zero, this model will give $\sqrt{3}$ LEED beams. In addition, the above term will only average to zero if the O atoms are distributed over a substantial range in height.

The structure factor arguments presented above can also be applied to the displacement of the top layer Ru atoms caused by water adsorbed in a hexagonal and commensurate array. DFT calculations by Darling [4] find that Ru atoms with flat water molecules adsorbed on top are displaced toward the vacuum by 0.054 ± 0.014 Å relative to bare Ru atoms or those that have H-down water molecules adsorbed on top. Thus, this buckling of the Ru will mirror the well-defined lateral

periodicity of the O sites in the flat-lying water molecules. Indeed, it will provide a contribution to the $\sqrt{3}$ LEED beams and should therefore be included in the scattering factor. Interestingly, Held and Menzel also reported an anti-correlation of the O and Ru height [3].

In this simple model, we have so far assumed the O atoms have a fixed lateral site and a vertical height that depends only whether water is in an flat or H-down adsorption geometry. However, in reality, the lateral and vertical O location will also be influenced by the local coordination of neighbouring water molecules. Consequently, this will broaden the distribution of O and Ru positions, contributing to the averaging, reducing the scattering factor and hence the beam intensity. The extent of this averaging can be investigated by comparing against the DFT calculations and observing how the O positions vary depending on the local environment of the water. As discussed earlier, the flat-lying and H-down water molecules display markedly different behaviour on the Ru (0001) surface. Flat-lying water molecules form a well-defined bond to the Ru, with the Ru height tightly constrained. The DFT calculations find an average Ru-O separation of 2.37 ± 0.067 Å for a typical disordered ($2\sqrt{3} \times 4\sqrt{3}$) chain structure (e.g. structure 4.15b), with a comparable variation in the absolute O height ($\sigma_z = 0.08$ Å). Similarly, the RMS lateral displacement of these O atoms from the atop position is rather small, 0.09 Å . The O position is even more tightly constrained in the ordered chains depicted in figure 4.14, with the O displacement increasingly only for the shortest chain structures shown in figure 4.14. Overall, the variation in the O position for the flat-lying water molecules is appreciably less than the 0.18 Å RMS displacement used by Puisto *et al.* in the re-analysis of the original LEED I-V data [20].

In contrast, the H-down water molecules that complete the hexagonal network often exhibit a considerably larger displacement from the regular atop site, depending on the local hydrogen-bonding environment. For instance, in figure 4.15b,

the O atoms of the H-down water molecules have a typical height variation of σ_z = 0.15 Å , an RMS lateral displacement of σ_{XY} = 0.34 Å and a Ru-O separation of 3.44±0.22 Å . While the more regular chain structures of figure 4.12 pin the flat-lying water molecules close to the Ru surface, the DFT calculations find that the binding energy is not particularly sensitive to the lateral location of the O atoms of the H-down water molecules, even for an RMS displacement as large as 0.5 Å . Thus, from these findings it is anticipated that scattering from the O atoms of the flat water molecules will only experience limited averaging because of displacement by the local hydrogen bonding network. In contrast, because the O atoms in the upper layer adopt a greater range of geometries they will suffer greater averaging and may well contribute little to the scattering intensity. Cleary, the analysis described above can tell us nothing about the intensity or I-V characteristics of the LEED spots. Indeed, this would require a full multiple scattering calculation for the disordered water network, which may well be impracticable. On the other hand, we can address the relationship between the structures proposed here and the previous LEED I-V analysis by Held and Menzel [3] [20].

Having ruled out partial dissociation as a factor in the Held and Menzel's LEED I-V data [3], we must then consider their failure to find any corrugation in wetting layer on Ru (0001). In their original analysis, Held and Menzel assumed the presence of a simple $(\sqrt{3} \times \sqrt{3})$R30° unit cell with two distinct oxygen heights and then fitted the site and position of the O atoms, as well as the relaxation of the Ru layer. Although they concluded that the best structure was a non-buckled monolayer structure, they were unable to rule out a buckled bilayer structure with Δz_O of 0.7 Å . However, in a subsequent reanalysis of the I-V data where the O RMS displacements were optimised and an H atom added above the upper O, they found that the layer could not be buckled. In contrast, the chain structure has no simple local $(\sqrt{3} \times \sqrt{3})$R30° ordering of the flat or H-down water sites within

the hexagonal superstructure. Thus, although this structure has a corrugation of about 1 Å , this would not be detected by a LEED I-V analysis with an a priori assumption of a simple $(\sqrt{3} \times \sqrt{3})R30°$ unit cell.

Moreover, the presence of any long-range correlation between the heights of adjacent oxygen atoms will be offset by the disorder in the flat/H down chain direction and length. This reduces the LEED pattern from the ideal $\sqrt{3} \times 2\sqrt{3}$ symmetry of the chains structure to that of a $(\sqrt{3} \times \sqrt{3})R30°$ skeleton. What is more, this lack of long-range correlation in the heights of adjacent O atoms will mask the corrugation of the wetting layer irrespective of the level of electron beam damage. Thus, any reanalysis of this system will have to take in to consideration the lateral disorder in the lower O site within the honeycomb hydrogen bonded network, as well as the much greater RMS displacement of the upper water molecules.

4.4 Conclusions

On Ru (0001), we find that ordered H_2O /D_2O $(\sqrt{3} \times \sqrt{3})R30°$ layers, with well-defined LEED patterns have a very low He reflectivity and produce diffuse features in the scattering, with no well-defined diffraction peaks. This implies that, although there is lateral order in the location of the oxygen atoms, the repulsive potential sampled by the He beam is disordered. An intact bilayer structure containing a mixture of H-up and H-down water molecules has been proposed by Meng *et al.* [24], with the correct proportion of the H-up and H-down mixture (between 1:2 and 1:3) producing the correct workfunction. This structure, which is reliant on the H-up and H-down water bilayers having a very similar binding energy, is qualitatively consistent with the disorder seen in our HAS measurements. However, it fails to account for the absence of a free OH stretching band in the SFG [26] and RAIR spectra [23] [4]. In contrast, we find that a water network containing flat-lying chains produces a calculated binding energy that is more then 20 %

larger than the traditional bilayer structure [4]. In addition, this chain structure reproduces the observed workfunction without resort to arbitrary assumptions about the H-up/H-down makeup of the wetting layer. Furthermore, in this chain structure model, the water network is inherently disordered, with no constraint on the longer-range lateral registry (H-up or H-down) of the water molecules. This gives rise to the low reflectivity and disorder observed in the HAS measurements. In this chapter, we have argued that the long-range periodicity of the O adsorption site is very much consistent with an ordered $(\sqrt{3} \times \sqrt{3})R30°$ LEED pattern. What is more, the variation in O position most likely contributes to making the O atoms of the H-down water in the upper part of the layer invisible to LEED. Finally, disorder in the water layer will also lead to a variation in the O-O distances [4], contributing to the inhomogeneous broadening of the vibrational spectrum, which indeed shows broad bands in the free OH stretching region [29].

Chapter 5

Conclusions

For many years, the established model describing water adsorption on close packed metal surfaces has been the 'bilayer model' originally developed by Doering and Madey in 1982 [59]. This configuration assumes that the water molecules bind atop the metal atoms via one of their oxygen lone pairs to form a lower chemisorbed layer, which then hydrogen bonds to a slightly higher layer of water molecules. Moreover, each O atom in the hydrogen bonded network is vertically displaced from its nearest neighbour by ca. 0.97 Å , giving the bilayer a distinctive 'puckered' corrugation. A complete bilayer, with an ideal coverage of $\theta = 2/3$ ML, is expected to show a $(\sqrt{3} \times \sqrt{3})$R30° superstructure in LEED. On the contrary, the experimental data reported in this thesis shows that this simple picture is not adequate for describing water adsorption on the Ru(0001) and Ni(111) close packed surfaces.

On the well-studied Ru (0001) surface, Helium atom scattering (HAS) shows no sharp diffraction peaks suggestive of an ordered bilayer structure, even as LEED shows an ordered $(\sqrt{3} \times \sqrt{3})$R30° pattern. Rather, the HAS data indicates a highly corrugated but disordered surface potential. The low electron scattering cross section of H and D means that the ordered $(\sqrt{3} \times \sqrt{3})$R30° pattern consistently observed in LEED only reflects the ordering of the O and Ru atoms. Thus, at the

correct coverage ($\sim$2/3 ML in this case) ordered domains of O atoms are formed in the water layer, giving rise to a sharp $\sqrt{3}$ LEED pattern. In contrast, no such coverage dependence is observed in HAS, implying that the top layer of atoms in the water structure is disordered even while LEED indicates the presence of long-range order.

The findings from the HAS measurements strongly suggest that we can preclude a commensurate $\sqrt{3}$ bilayer as the wetting layer on this surface. Instead, we argue that both the disorder implied by HAS and the long-range order suggested by LEED are consistent with a ($\sqrt{3} \times \sqrt{3}$)R30° wetting layer that has periodicity in the O sites, within an intrinsically disordered hydrogen bonded structure consisting of chains of flat and H-down water. Importantly, while hydrogen-bonding network imposes long-range order on the adlayer it allows for substantial local disorder, with disorder arising from the orientation of the protons along the chains, the direction of the chains and the chain length. Density functional theory (DFT) calculations for a 2/3 ML wetting layer based on this chain model indicate that its binding energy is sufficiently close to that of bulk ice for wetting to be expected.

LEED IV measurements for an intact D_2O layer, produce IV profiles that are qualitatively very similar those of the original simulations of Held and Menzel [3], implying that dissociation was not a factor in their study. The failure of Held and Menzel to find any corrugation in the wetting layer on Ru (0001) may be accounted for by their assumption of a simple ($\sqrt{3} \times \sqrt{3}$)R30° unit cell with two distinct O heights. In contrast, the chain structure has no simple local ($\sqrt{3} \times \sqrt{3}$)R30° ordering of the flat or H-down water sites within the hexagonal superstructure. Consequently, while it has a corrugation of about 1 Å , this would not be detected by a LEED I-V analysis with an a priori assumption of a simple ($\sqrt{3} \times \sqrt{3}$)R30° unit cell. Moreover, while the chain structure should ideally produce a $\sqrt{3} \times 2\sqrt{3}$ LEED pattern, this symmetry is reduced to that of a ($\sqrt{3} \times \sqrt{3}$)R30° skeleton by the disorder in the flat/H-down chain direction, which

offsets any long-range correlation in the heights of adjacent O atoms. The lack of long-range correlation in the heights of adjacent O atoms also helps to mask the corrugation of the wetting layer, making it seem coplanar. Moreover, O atoms in the higher layer are expected to have a much larger Debye-Waller factor, reducing their contribution to the diffraction. Any future LEED IV reanalysis must be able to take into account the lateral disorder in the lower O site, within the honeycomb hydrogen bonded network.

While the chain structure is consistent with the experimental observation that water wets the Ru (0001) surface, it is not yet proven that this structure correctly describes the configuration of water on this surface, since the presence of intrinsic disorder and the electron sensitivity of the water film make it exceptionally difficult to draw definitive conclusions about its structure. Nevertheless, many aspects of this calculated minimum energy structure are qualitatively consistent with existing experimental observations. These include the high degree of order implied by LEED even as HAS suggests considerable disorder, the absence of the 'free' OH stretch in the vibrational spectra, the agreement of the workfunction with that calculated for the chain structure and the minimal corrugation of the wetting layer indicated by the previous LEED IV simulations (which neglected disorder). As a future development, tests to examine the compatibility of the chain structure with the LEED IV data are needed. These simulations must be able to provide a proper treatment of the lateral disorder intrinsic in the chain structure.

A water-wetting layer based on the chain model may also have important implications for other metal surfaces. Indeed, the workfunction measurements for water adsorption on Pd (111) (chapter 3) are consistent with the commensurate wetting layer having the same chain structure on that surface and inconsistent with the original bilayer model. Moreover, calculations [41] [78] for the complex $(\sqrt{39} \times \sqrt{39})R16.1°$ layer on Pt(111) also reveal chains of flat water within the overall hydrogen bonding network, suggesting that the formation of chains of flat

water is important even in the structure of incommensurate or large unit cell structures.

On the Ni (111) surface early reports indicated the formation of a simple commensurate $(\sqrt{3} \times \sqrt{3})$R30° structure [16]. In contrast, we find that ordered water layers grown at above 135 K display a $(2\sqrt{7} \times 2\sqrt{7})$R19° LEED pattern for coverages of 0.4 up to the saturation of the first layer. Thus, upon adsorption, water aggregates to form extended islands of ordered ice rather than binding at a favoured adsorption site on the metal to form small commensurate clusters, the water molecules preferring to optimise the lateral period of their hydrogen-bonding network at the expense of the favoured atop adoption site on the metal surface. Due to the relatively short lattice parameter of the Ni(111) surface, the formation of a commensurate $(\sqrt{3} \times \sqrt{3})$R30° unit cell with a stable hydrogen-bonding network would require a 4.5 % compression (relative to bulk ice), which is simply too great. Instead, we propose a wetting layer with a distorted hexagonal honeycomb structure (similar to those proposed on Pt (111), a $2\sqrt{7}$ network and a lateral compression of 2.8 %. The unit cell of this $(2\sqrt{7} \times 2\sqrt{7})$R19° structure contains 18 different water molecules, giving rise to a range of different adsorption sites, with different geometries and vibrational frequencies. Importantly, unlike the behaviour observed on Pt (111), the wetting layer on Ni (111) is particularly labile, restructuring into an incommensurate R30° hexagonal structure oriented to the Ni close packed rows as soon as a small amount of water is adsorbed on top. The water monolayer on this surface is particularly sensitive to electron exposure, with extended electron irradiation leading to formation of an intense (2×2) pattern, probably caused by dissociation to form chemisorbed O.

These studies reveal the remarkable flexibility of water adsorption on close packed metal surfaces. Indeed, the conventional view that water adsorbs via the formation of a commensurate $(\sqrt{3} \times \sqrt{3})$R30° bilayer is too simplistic to explain wetting of the Ru (0001) and Ni (111) surfaces. Instead, water forms hydro-

gen bonded networks whose structure depends on the metal-water bond and the chemical reactivity of the surface as much as the lateral parameter of the metal substrate.

Bibliography

[1] PA Thiel and TE Madey, *Surface Science Reports* **7**, 211-385 (1987).

[2] C Lobban, JL Finney, and WF Kuhs, *Nature* **391**, 268-270 (1998).

[3] G Held and D Menzel, *Surface Science* **316**, 92-102 (1994).

[4] S Haq, C Clay, GR Darling, G Zimbitas, and A Hodgson, *Physical Review B* **73**, 115414 (2006).

[5] M Gallagher, A Omer, GR Darling, and A Hodgson, *Faraday Discussions of the Royal Society of Chemistry* **141**, (2008).

[6] WM Latimer and WH Rodebush, *Journal of the American Chemical Society* **42**, 1419 (1920).

[7] M Cavalleri, H Ogasawara, LGM Pettersson, and A Nilsson, *Chemical Physics Letters* **364**, 363-370 (2002).

[8] H Ogasawara, J Yoshinobu, and M Kawai, *Chemical Physics Letters* **231**, 188-192 (1994).

[9] R Ludwig, *Angewandte Chemie-International Edition* **40**, 1808-1827 (2001).

[10] PA Thiel, FM Hoffmann, and WH Weinberg, *Journal of Chemical Physics* **75**, 5556-5572 (1981).

[11] JD Bernal and RH Fowler, *Journal of Chemical Physics* **1**, 515-548 (1933).

[12] L Pauling, *Journal of the American Chemical Society* **1**, 2680 (1935).

[13] MA Henderson, *Surface Science Reports* **46**, 5-308 (2002).

[14] V Buch, P Sandler, and J Sadlej, *Journal of Physical Chemistry B* **102**, 8641-8653 (1998).

[15] T Matsuo, Y Tajima, and H Suga, *Journal of Physics and Chemistry of Solids* **47**, 165-173 (1986).

[16] TE Madey and FP Netzer, *Surface Science* **117**, 549-560 (1982).

[17] A Hodgson and S Haq, *Submitted* (2008).

[18] TE Madey and JT Yates, *Chemical Physics Letters* **51**, 77-83 (1977).

[19] PJ Feibelman, *Science* **295**, 99-102 (2002).

[20] SR Puisto, TJ Lerotholi, G Held, and D Menzel, *Surface Review and Letters* **10**, 487-492 (2003).

[21] G Materzanini, GF Tantardini, PJD Lindan, and P Saalfrank, *Physical Review B* **71**, 155414 (2005).

[22] A Michaelides, A Alavi, and DA King, *Journal of the American Chemical Society* **125**, 2746-2755 (2003).

[23] C Clay, S Haq, and A Hodgson, *Chemical Physics Letters* **388**, 89-93 (2004).

[24] S Meng, EG Wang, C Frischkorn, M Wolf, and SW Gao, *Chemical Physics Letters* **402**, 384-388 (2005).

[25] PJ Feibelman and A Alavi, *Journal of Physical Chemistry B* **108**, 14362-14367 (2004).

[26] DN Denzler, C Hess, R Dudek, S Wagner, C Frischkorn, M Wolf, and G Ertl, *Chemical Physics Letters* **376**, 618-624 (2003).

[27] DN Denzler, S Wagner, M Wolf, and G Ertl, *Surface Science* **532**, 113-119 (2003).

[28] G Held and D Menzel, *Surface Science* **327**, 301-320 (1995).

[29] PJ Feibelman, *Chemical Physics Letters* **389**, 92-95 (2004).

[30] K Andersson, A Nikitin, LGM Pettersson, A Nilsson, and H Ogasawara, *Physical Review Letters* **93**, 196101 (2004).

[31] J Weissenrieder, A Mikkelsen, JN Andersen, PJ Feibelman, and G Held, *Physical Review Letters* **93**, 196102 (2004).

[32] NS Faradzhev, KL Kostov, P Feulner, TE Madey, and D Menzel, *Chemical Physics Letters* **415**, 165-171 (2005).

[33] PJ Schmitz, JA Polta, SL Chang, and PA Thiel, *Surface Science* **186**, 219-231 (1987).

[34] PJ Schmitz, JA Polta, SL Chang, and PA Thiel, *Journal of Vacuum Science and Technology A-Vacuum Surfaces and Films* **5**, 1086-1088 (1987).

[35] G Held and D Menzel, *Physical Review Letters* **74**, 4221-4224 (1995).

[36] K Kretzschmar, JK Sass, and P Hofmann, *Chemical Physics Letters* **78**, 410-412 (1981).

[37] PA Thiel, FM Hoffmann, and WH Weinberg, *Physical Review Letters* **49**, 501-504 (1982).

[38] K Kretzschmar, JK Sass, and AM Bradshaw, *Surface Science* **115**, 183-194 (1982).

[39] PA Thiel, RA Depaola, and FM Hoffmann, *Journal of Chemical Physics* **80**, 5326-5331 (1984).

[40] G Pirug, C Ritke, and HP Bonzel, *Surface Science* **241**, 289-301 (1991).

[41] S Meng, EG Wang, and SW Gao, *Physical Review B* **69**, 195404 (2004).

[42] GB Fisher and JL Gland, *Surface Science* **94**, 446-455 (1980).

[43] BA Sexton, *Surface Science* **94**, 435-445 (1980).

[44] LE Firment and GA Somorjai, *Surface Science* **55**, 413-426 (1976).

[45] M Morgenstern, T Michely, and G Comsa, *Physical Review Letters* **77**, 703-706 (1996).

[46] M Morgenstern, J Muller, T Michely, and G Comsa, *Zeitschrift fur Physikalische Chemie-International Journal of Research in Physical Chemistry and Chemical Physics* **198**, 43-72 (1997).

[47] A Glebov, AP Graham, A Menzel, and JP Toennies, *Journal of Chemical Physics* **106**, 9382-9385 (1997).

[48] S Haq, J Harnett, and A Hodgson, *Surface Science* **505**, 171-182 (2002).

[49] J Harnett, S Haq, and A Hodgson, *Surface Science* **528**, 15-19 (2003).

[50] G Zimbitas, S Haq, and A Hodgson, *Journal of Chemical Physics* **123**, 174701 (2005).

[51] RT Bayard and D Alpert, *Review of Scientific Instruments* **21**, 571 (1950).

[52] DA King and MG Wells, *Surface Science* **29**, 454-482 (1972).

[53] Lord Kelvin, *Philosophical Magazine* **46**, 82-120 (1898).

[54] WA Zisman, *Review of Scientific Instruments* **3**, 367-370 (1932).

[55] T Pache, HP Steinruck, W Huber, and D Menzel, *Surface Science* **224**, 195-214 (1989).

[56] FP Netzer and TE Madey, *Physical Review Letters* **47**, 928-931 (1981).

[57] C Nobl and C Benndorf, *Surface Science* **182**, 499-520 (1987).

[58] H Yang and JL Whitten, *Surface Science* **223**, 131-150 (1989).

[59] DL Doering and TE Madey, *Surface Science* **123**, 305-337 (1982).

[60] C Mundt and C Benndorf, *Surface Science* **287**, 119-124 (1993).

[61] M Nakamura and M Ito, *Chemical Physics Letters* **384**, 256-261 (2004).

[62] M Nakamura and M Ito, *Chemical Physics Letters* **404**, 346-350 (2005).

[63] C Clay, S Haq, and A Hodgson, *Physical Review Letters* **92**, 046102 (2004).

[64] G Held, C Clay, SD Barrett, S Haq, and A Hodgson, *Journal of Chemical Physics* **123**, 064711 (2005).

[65] C Clay and A Hodgson, *Current Opinion in Solid State and Materials Science* **9**, 11-18 (2006).

[66] JS Filhol and ML Bocquet, *Chemical Physics Letters* **438**, 203-207 (2007).

[67] L Cummings, C Clay, A Omer, S Haq, GR Darling, and A Hodgson, *Submitted*, (2008).

[68] M Nakamura, M Tanaka, M Ito, and O Sakata, *Journal of Chemical Physics* **122**, 224703 (2005).

[69] M Nakamura and M Ito, *Physical Review Letters* **94**, 035501 (2005).

[70] G Zimbitas and A Hodgson, *Chemical Physics Letters* **417**, 1-5 (2006).

[71] GA Kimmel, NG Petrik, Z Dohnalek, and BD Kay, *Physical Review Letters* **95**, 166102 (2005).

[72] R Souda, *Chemical Physics Letters* **415**, 146-149 (2005).

[73] R Souda, *Journal of Physical Chemistry B* **110**, 17524-17530 (2006).

[74] H Ogasawara, B Brena, D Nordlund, M Nyberg, A Pelmenschikov, LGM Pettersson, and A Nilsson, *Physical Review Letters* **89**, 276102 (2002).

[75] F Traeger, D Langenberg, Y K Gao, and Ch Woell, *Physical Review B* **76**, 033410 (2007).

[76] T Kondo, S Mae, H S Kato, and M Kawai, *Surface Science* **600**, 3570-3574 (2006).

[77] PJ Feibelman, *Physical Review B* **72**, 113405 (2005).

[78] PJ Feibelman, *Physical Review Letters* **91**, 059601 (2003).

[79] G Darling, *Private communication*.

Appendix A

Publications

- Water Monolayer and Multilayer Adsorption on Ni (111)
  M. Gallagher, A. Omer, S. Haq and A. Hodgson, *Surface Science*, **601** 268-273 (2007)

- Order and Disorder in the Wetting Layer on Ru (0001)
  M. Gallagher, A. Omer, G.R. Darling and A. Hodgson, *Faraday Discussions of the Royal Society of Chemistry*, **141** (2008)

- Segregation and Stability at $Pt_3Ni(1\ 1\ 1)$ Surfaces and $Pt_{75}Ni_{25}$ Nanoparticles
  B.Fowler, C.A. Lucas, A.Omer, G. Wang, V.R. Stamenkovic and N.M. Markovic, *Electrochimica Acta* , **53** 60766080 (2008)

- L. Cummings, C. Clay, A. Omer, S. Haq, G.R. Darling and A. Hodgson, *Surface Science: submitted*, (2008)